# UC Santa Barbara
## UC Santa Barbara Electronic Theses and Dissertations

**Title**

Indium Phosphide Photonic Integrated Circuits for CO2 Lidar

**Permalink**

https://escholarship.org/uc/item/8h77c7z7

**Author**

Rosborough, Victoria

**Publication Date**

2022

Peer reviewed|Thesis/dissertation

UNIVERSITY of CALIFORNIA
Santa Barbara

**Indium Phosphide Photonic Integrated Circuits for CO$_2$ Lidar**

A dissertation submitted in partial satisfaction of the
requirements for the degree of

Doctor of Philosophy

in

Electrical and Computer Engineering

by

Victoria Marie Rosborough

Committee in charge:

Professor Jonathan Klamkin, Chair

Professor Larry A. Coldren

Professor Nadir Dagli

Dr. Mark Stephen

June 2022

The dissertation of Victoria Marie Rosborough is approved:

_____

Professor Larry A. Coldren

_____

Professor Nadir Dagli

_____

Dr. Mark Stephen

_____

Professor Jonathan Klamkin, Chair

June 2022

This dissertation is dedicated to Diane and Rick Rosborough.
Thank you for always believing in me.

# Acknowledgements

I couldn't have completed my PhD without support from many family, friends, fellow graduate students, post-docs, collaborators, and my committee. I'd like to thank my PhD advisor, Professor Jonathan Klamkin, for giving me the opportunity join his research group and study in the field of photonics. His guidance over the years has been invaluable. His knowledge spanning from MOCVD growth to device and PIC design to opto-electronic integration made the work in this dissertation possible. I'd also like to thank Professor Larry Coldren for contributing his expert advice to the $CO_2$ lidar project. I'm appreciative to Dr. Mark Stephen for seeing the potential of PIC technology for space applications and providing the perspective from the NASA side. I'd like to thank Professor Nadir Dagli for providing feedback on my dissertation. In addition to my committee, I'm appreciative of our collaborators and program managers at NASA: Kenji Numata, Randy Kawa, Jeffrey Chen, Parminder Ghuman, and Amber Emory.

I'm also indebted to many fellow graduate students as well as post-docs. I'd like to especially thank Fengqiao Sang, Joseph Fridlander, Fabrizio Gambini, Lei Wang, Simone Brunelli, Sergio Pinna, Bowen Song, and Hongwei Zhao. I learned so much from all of them and they made the day-to-day of research life enjoyable.

I'd also like to thank Amanda Miller, the Optoelectronics Technology Center (OTC) administrative assistant, Paul Gritt, the ESB building manager, Raul Ramirez, electronics shop assistant, and Daryl Lee , the IT manager.

The members of the Photonics Society at UCSB were also an important part of my graduate school experience. Takako Hirokawa, Andrew Netherton, Shereen Hamdy, Warren Jin, Eric Stanton, Philip Chan, and Demis John made planning and participating in education outreach events fun and fulfilling. The programs run by the staff in the UCSB Center for Science and Engineering Partnerships (CSEP), including Wendy Ibsen, Arica Lubin, and Carli Ruskauff, made all Photonics Society educational outreach events possible.

None of the work in this dissertation would have been possible without the dedicated efforts of the UCSB Nanofab staff: Brian Thibeault, Tom Reynolds, Tony Bosch, Brian Lingg, Aidan Hopkins, Ning Cao, Bill Mitchell, Demis John, Biljana Stamenic, Don Freeborn, Lee Sawyer, Mike Day, Mike Silva, Luis Zuzunaga, and Tino Sy.

I'm grateful to my parents, Diane and Rick Rosborough for their unwavering support and confidence in me. My sister and brother, Sara and James, always helped me to keep things in perspective. My aunt, uncle, and cousin, Vivien Hoke and Bill and Willow Freeman, were always interested in hearing about graduate school and my research. My grandmother, Constance Hoke, never stops rooting for me.

Last, but not least, I'm grateful to my partner, Philip Chan, for always accepting me through thick and thin. I can't wait to start the next chapter of our lives together, now that we've both completed our PhD's!

# Curriculum Vitæ

## Victoria Marie Rosborough

**Education**

| | |
|---|---|
| 2022 | Ph.D., Electrical and Computer Engineering, University of California, Santa Barbara, CA |
| 2013 | M.S., Applied Physics, University of Oregon, Eugene, OR |
| 2012 | B.S., Physics, Mary Baldwin University, Staunton, VA |

**Patents**

B. Song, J. Klamkin, V. Rosborough, J. Fridlander, and M. A. Stephen, "Method for Integration of Variable Bragg Grating Coupling Coefficients," U.S. Patent Application No. 63/057,484, July 28, 2020.

**Publications**

1. F. Sang, V. Rosborough, J. Fridlander, F. Gambini, S. S. Brunelli, J. R. Chen, S. R. Kawa, K. Numata, M. Stephen, L. Coldren and J. Klamkin, "Dual Laser Indium Phosphide Photonic Integrated Circuits for Remote Active Carbon Dioxide Sensing," Optical Fiber Communication (OFC) Conference 2022.

2. P. Verrinder, L. Wang, F. Sang, V. Rosborough, G. Yang, M. Stephen, L. Coldren and J. Klamkin, "Widely Tunable 1030 nm Gallium Arsenide Sampled Grating Distributed Bragg Reflector Lasers and Photonic Integrated Circuits," Optical Fiber Communication (OFC) Conference 2022.

3. J. Klamkin, F. Sang, J. Fridlander, V. Rosborough, F. Gambini, S. T. S. Brunelli, L. Coldren, J. R. Chen, S. Kawa, K. Numata, and M. Stephen, "Integrated phase-locked lasers and photonic integrated circuits for remote gas sensing," 27th International Semiconductor Laser Conference (ISLC) 2021.

4. F. Sang, J. Fridlander, V. Rosborough, S. T. S. Brunelli, L. Coldren, J. Klamkin, J. Chen, K. Numata, S. Kawa, M. Stephen, "Integrated photonics technology for earth science remote-sensing lidar," IEEE International Geoscience and Remote Sensing Symposium 2021

5. V. Rosborough, J. Fridlander, F. Sang, F. Gambini, S. T. S. Brunelli, J. R. Chen, S. Kawa, K. Numata, M. Stephen, L. Coldren, and J. Klamkin, "Photonic Integration for Low Size, Weight, and Power (SWaP) Remote Gas Spectroscopy," OSA Optical Sensors and Sensing Congress 2021.

6.  J. Fridlander, F. Sang, V. Rosborough, F. Gambini, S. T. S. Brunelli, J. R. Chen, K. Numata. M. Stephen, L. A. Coldren, and J. Klamkin, "Dual Laser Indium Phosphide Photonic Integrated Circuit for Integrated Path Differential Absorption Lidar," IEEE J. Sel. Topics Quantum Electron, June 2021

7.  P. A. Verrinder, L. Wang, J. Fridlander, F. Sang, V. Rosborough, M. Nickerson, G. Yang, M. Stephen, L. Coldren, and J. Klamkin, "Gallium Arsenide Photonic Integrated Circuit Platform for Tunable Laser Applications," IEEE JSTQE, June 2021

8.  J. Fridlander, F. Sang, V. Rosborough, S. T. S. Brunelli, J. Chen, K. Numata, S. Kawa, M. Stephen, L. Coldren, and J. Klamkin, "Monolithic Indium Phosphide Dual Laser Photonic Integrated Circuit for Remote Sensing Lidar," Conference on Lasers and Electrooptics (CLEO) 2021 JTu3A.8.

9.  V. Rosborough, J. Fridlander, F. Sang, F. Gabmini, S. T. S. Brunelli, J. R. Chen, S. Kawa, K. Numata, M. Stephen, L. Coldren, and J. Klamkin, "Residual Amplitude Modulation Reduction in Integrated Indium Phosphide Phase Modulators," Conference on Lasers and Electrooptics (CLEO) 2021 STh4B.3.

10. J. Fridlander, V. Rosborough, F. Sang, M. Nickerson, J. Chen, K. Numata, P. Verrinder, F. Gambini, S. Pinna, S. Kawa, M. Stephen, L. Coldren, and J. Klamkin, "Photonic Integrated Circuits for Precision Spectrosctopy," CLEO (2020).

11. F. Sang, J. Fridlander, V. Rosborough, H. Zhao, S. S. Brunelli, M. A. Stephen, K. Randy, and J. R. Chen, K. Numata, and J. Klamkin "Monolithic Integrated Micro-Photonics for Earth Science Carbon Dioxide Remote Sensing Lidar," IEEE International Conference on Space Optical Systems and Applications (ICSOS) 2019

12. J. Fridlander, V. Rosborough, F. Sang, S. Pinna, S. Estrella, L. Johansson, J. Klamkin, "High-Speed RZ-DPSK Photonic Integrated Transmitter for Space Optical Communications," SPIE Optical Engineering + Applications Conference, 2019

13. V. Rosborough, F. Sang, J. Fridlander, H. Zhao. B. Song, S. Brunelli, J. R. Chen, M. A. Stephen, L. Coldren, J. Klamkin, "Monolithic Integration of Widely-Tunable DBR and DFB Laser with One-Step Grating Formation," Advanced Photonics Congress, Integrated Photonics Research, Silicon and Nanophotonics (IPR) 2019 IM2A.5.

14. M. Stephen, J. Klamkin, L. Coldren, J. Fridlander, V. Rosborough, F. Sang, J. Chen, K. Numata, R. Kawa, "Integrated Micro-Photonics for Remote Earth Science Sensing (IMPRESS) Lidar," IEEE Geoscience and Remote Sensing Society (IGARSS) Conference, 2019

15. F. Gambini, Y. Liu, B. Song, H. Zhao, V. Rosborough, F. Sang, P. Velha, S. Faralli, J. Klamkin "Ultra-Compact Bragg-Assisted Silicon Photonics Orbital Angular Momentum Emitter," Integrated Photonics Research, Silicon and Nanophotonics, 2019

16. S. W. Hamdy, T. Hirokawa, P. Chan, W. Jin, V. Rosborough, E. Stanton, A. M. Netherton, M. Garza, W. Ibsen, D. D. John, and J. Bowers, "Light-based educational outreach activities for pre-university students," Fifteenth Conference on Education and Training in Optics and Photonics (ETOP) 2019, Proc. Of SPIE vol. 11143.

17. J. Fridlander, V. Rosborough, F. Sang, S. Pinna, S. Estrella, L. Johansson, J. Klamkin, "Photonic Integrated Transmitter for Space Optical Communications," SPIE Photonics

West, 2019

18. S. Dwivedi, W. Xie, V. Rosborough, and J. Klamkin, "Compact 7-Channel SiN Wavelength De-multiplexer with Multi-core Fiber Fan-out," IEEE Avionics and Vehicle Fiber-Optics and Photonics Conference (AVFOP), 2018

19. J. Fridlander, S. Pinna, V. Rosborough, S. Estrella, L. Johansson, and J. Klamkin, "RZ-DPSK photonic integrated transmitter for space optical communications," SPIE Photonics West, 2018

20. V. Rosborough, F. Gambini, J. Snyder, L. Johansson, J. Klamkin, "Integrated transmitter for deep space optical communications," IEEE Avionics and Vehicle Fiber-Optics and Photonics Conference (AVFOP) 2016 WA3.2.

21. V. Rosborough, F. Gambini, J. Snyder, L. Johansson, and J. Klamkin, "Integrated Indium Phosphide Pulse Position Modulation Transmitter for Free Space Communications," Advanced Photonics Congress, Integrated Photonics Research, Silicon and Nanophotonics (IPR) 2016 ITu2A.3.

22. S. Jin, L. Xu, V. Rosborough, J. Klamkin, and Y. Li, "RF Frequency Mixer Photonic Integrated Circuit," IEEE Photonics Technology Letters, vol. 28, no. 16, pp. 1771–1773, Aug. 2016.

# Abstract

**Indium Phosphide Photonic Integrated Circuits for CO$_2$ Lidar**

by

Victoria Marie Rosborough

Photonic integrated circuit (PIC) technology will enable a future of ubiquitous compact sensors. One application space that can be disrupted by PIC-enabled sensors is remote Earth-science sensing. A photonic integrated lidar satellite module would greatly reduce the size, weight, and power of science instruments, making data collection much more affordable and accessible. In this work, a PIC was designed, fabricated, and characterized for a CO$_2$ integrated path differential absorption (IPDA) lidar system operating at 1572 nm. Key achievements include demonstration of a novel method for simultaneous definition of variable $\kappa$ laser mirror gratings, 60 dB SMSR DFB lasers, a novel implementation of a low residual amplitude modulation phase modulator design, and integration of most of the optical functions for a lidar system to meet the specifications defined by the IDPA CO$_2$ lidar developed for a NASA mission.

# Contents

# Chapter 1

# Introduction

## 1.1  Remote Sensing

While the definition of the term "remote sensing" encompasses any sensor physically removed from the measured species, it typically refers to earth science observation instruments on satellites, aircraft, and, increasingly commonly, drones. Application areas of remote sensing include disaster management, urban planning, and monitoring of greenhouse gasses, sea levels, and ice sheet levels. Remote sensors may be "passive", where they rely on reflected sunlight, or "active", where they include an on-board radiation source. Cameras and spectrometers are both examples of passive remote sensors, while radar is an example of an active remote sensor. Lidar ("light detection and ranging") is the equivalent of radar in the optical frequency domain. Lidar systems use an on-board laser as the signal and information is deduced from the interaction of light with the environment. Lidar is a rapidly growing technology sector because it can provide extremely precise information

1

at a distance. For example, lidar, in combination with cameras, is being implemented in self-driving cars for mapping the surrounding landscape. Unlike passive cameras, lidar can provide information about object distance and velocity.

Remote sensing lidars in earth-orbiting satellites are providing scientists with detailed data regarding wind patterns and sea and ice levels [1]–[3]. In the most recent decadal survey released by NASA, lidar was identified as a key technology for providing precision monitoring of levels of greenhouse gasses, including carbon dioxide ($CO_2$) in the atmosphere. To address this priority, the Active Sensing of $CO_2$ Emissions over Nights, Days, and Seasons (ASCENDS) mission was enacted. The goal of the ASCENDS mission is to develop a $CO_2$ lidar to meet the 1 ppm measurement precision called for in the decadal survey [4]–[10].

## 1.2   Photonic Integrated Circuits

Photonic integration, where optical components are incorporated on a semiconductor chip via microfabrication, drastically reduces the size, weight and power consumption (SWaP) of optical systems, making it a key technology in the growing lidar sector. Photonic integration will enable a future of ubiquitous smart, compact sensors from lidars to lifi to wearable health monitors. While photonic integrated circuits (PICs) are analogous to electronic integrated circuits (EICs), they differ in their potential for volume production and device density scaling. PIC design pulls from a much wider set of materials and devices when compared to EICs. Therefore, most PIC design and prototyping today requires expertise and in-house fabrication or participation in expensive multi-project wafer (MPW) runs with a foundry

2

service, many of which use different simulation and layout software packages. While MPW runs give institutions with the expertise and resources the opportunity to develop application specific PICs (ASPICs), PIC development is not as accessible as application specific integrated circuit (ASIC) development. There is a push to make PIC prototyping standardized and more accessible, which will lead to an explosion of application spaces. The reduction in SWaP provided by PICs will enable the democratization of remote sensing experiments by enabling small form factor satellites, such as cubesats, with powerful instrumentation.

## 1.3 Scope of Thesis

The goal of this dissertation is to provide an example of how integrated photonic technology can be implemented for a compact spectroscopic lidar sensor. This is just the beginning of this application space, with many other PIC material platforms and target wavelengths realizable. In this thesis, a monolithic indium phosphide (InP) PIC for lidar spectroscopy of the 1572.335 nm absorption line of atmospheric carbon dioxide ($CO_2$) is presented. The selection of this specific application grew from a collaboration with the researchers at NASA Goddard Space Flight Center developing a lidar system from commercial-off-the-shelf (COTS) optical components as a part of the ASCENDS mission. Figure 1.1 illustrates the COTS system side-by-side with the PIC, which integrates most of the optical functionality of the lidar system. The PIC layout and target specifications were adapted from the system built at NASA. The PIC consists of a leader laser stabilized at 1572.335 nm using a frequency modulation locking technique with an integrated phase modulator. Output from a follower laser

offset-locked to the leader laser is pulsed and scanned $\pm 15$ GHz around 1572.335 nm to sample the $CO_2$ absorption line. An integrated photodetector tracks the beat note between the leader and follower lasers for the offset locking of the follower laser via an optical phase lock loop (OPLL).

The overall project involved three generations of fabrication runs for two different InP integration platforms, offset quantum well (OQW) and quantum well intermixing (QWI), with work contributed by several graduate students. In this project, we demonstrated the first monolithic PIC integrating most of the optical functionality for a differential absorption lidar system. The only off-chip optical components needed are a $CO_2$ Herriott cell used for stabilizing the leader laser and an erbium-doped fiber amplifier (EDFA) for amplifying the output pulses. My contributions to the project included epitaxial material design, mask layout, QWI laser design, design of a low residual amplitude modulation (RAM) phase modulator, and fabrication and characterization of a QWI platform lidar PIC.

This dissertation is organized into the following chapters: Chapter 2 gives an overview of photonic integration for remote spectroscopy. Chapter 3 provides detail on the lidar system operation and how it was translated to the PIC layout. Chapter 4 outlines the compound semiconductor material design and PIC fabrication process. In Chapter 5, the characterization results of several laser designs are presented. Chapter 6 covers the design and characterization of the low RAM phase modulator for improving the leader laser stabilization. In Chapter 7, the results of the PIC characterization for $CO_2$ sensing are presented. Finally, Chapter 8 summarizes the accomplishments of this dissertation and discusses future work.

**Existing Technology**

~ ½ rack of equipment

0.25 m

1 m

0.25 m

**Photonic Integrated Circuit**

Diode laser

Intensity modulator

Phase modulator

PIC  1 mm

8 mm

Couplers & splitters
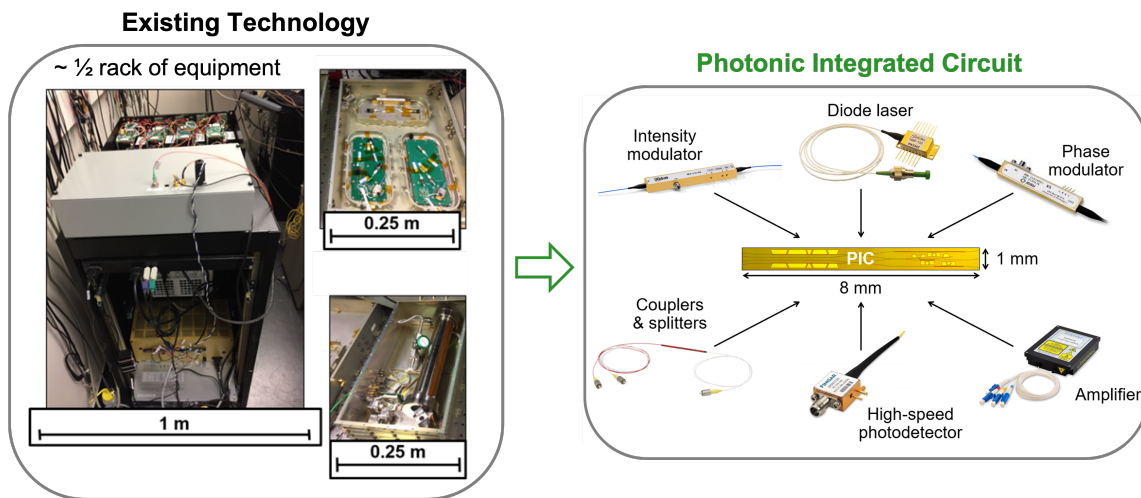
High-speed photodetector

Amplifier

Figure 1.1: Left: Photo of NASA lidar system assembled from commercial-off-the-shelf components comprising about half a rack of equipment. Right: An example of a PIC developed for this work with a representation of the individually packaged components it replaces.

# References

[1] NASA, *World class lidar science*, https://science.larc.nasa.gov/lidar/, Accessed: 2022-05-08.

[2] NASA, *Icesat-2*, https://icesat-2.gsfc.nasa.gov/space-lasers, Accessed: 2022-05-08.

[3] University of Maryland, *Gedi*, https://gedi.umd.edu/, Accessed: 2022-05-08.

[4] K. Numata, J. R. Chen, S. T. Wu, J. B. Abshire, and M. A. Krainak, "Frequency stabilization of distributed-feedback laser diodes at 1572 nm for lidar measurements of atmospheric carbon dioxide," *Applied Optics*, vol. 50, no. 7, pp. 1047–1056, 2011.

[5] K. Numata, J. R. Chen, and S. T. Wu, "Precision and fast wavelength tuning of a dynamically phase-locked widely-tunable laser," *Optics Express*, vol. 20, no. 13, 2012.

[6] J. R. Chen, K. Numata, and S. T. Wu, "Error analysis for lidar retrievals of atmospheric species from absorption spectra," *Optics Express*, vol. 27, no. 25, pp. 36 487–36 504, 2019.

[7] J. R. Chen, K. Numata, and S. T. Wu, "Error reduction in retrievals of atmospheric species from symmetrically measured lidar sounding absorption spectra," *Optics Express*, vol. 22, no. 21, pp. 26 055–26 075, 2014.

[8] G. R. Allan, J. B. Abshire, H. Riris, M. Jianping, W. E. Hasselbrack, K. Numata, J. Chen, R. Kawa, M. Rodriguez, and M. Stephen, "Lidar measurements of co2 column concentrations in the arctic region of north america from the ascends 2017 airborne cam-

paign," *SPIE Asia-Pacific Remote Sensing Conference*, vol. 10779, 2018. DOI: `10.1117/12.2325908`.

[9] J. B. Abshire, A. K. Ramanathan, H. Riris, G. R. Allan, X. Sun, W. E. Hasselbrack, J. Mao, S. Wu, J. Chen, K. Numata, S. R. Kawa, M. Y. M. Yang, and J. DiGangi, "Airborne measurements of co2 column concentrations made with a pulsed ipda lidar using a multiple-wavelength-locked laser and hgcdte apd detector," *Atmospheric Measurement Techniques*, vol. 11, pp. 2001–2025, 2018. DOI: `https://doi.org/10.5194/amt-11-2001-2018`.

[10] J. Mao, A. Ramanathan, J. B. Abshire, S. R. Kawa, H. Riris, G. R. Allan, M. Rodriguez, W. E. Hasselbrack, X. Sun, K. Numata, J. Chen, Y. Choi, and M. Y. M. Yang, "Measurement of atmospheric co2 column concentrations to cloud tops with a pulsed multi-wavelength airborne lidar," *Atmospheric Measurement Techniques*, vol. 11, pp. 127–140, 2018. DOI: `https://doi.org/10.5194/amt-11-127-2018`.

# Chapter 2

# Photonic Integration for Spectroscopy

The main market driving photonic integrated circuit (PIC) development has been the telecommunications industry. Semiconductor lasers and PICs are regularly used for short and long range communications over optical fiber to power the internet. Today, the advantages of PICs are being realized for myriad applications including data center interconnects, high performance computing, quantum communications, lidar, and free space communications. With an expanding application space, has come an array of PIC platform and device innovations. Section 2.1 gives an overview of gas sensing and lidar satellite missions at NASA. Section 2.2 briefly reviews photonic integration methods. Section 2.3 reviews recent work in PIC-based gas sensors and details the PIC platform used in this work.

## 2.1 Remote Spectroscopy

To date, the satellite data of atmospheric $CO_2$ that NASA has collected is measured using passive spectrometers known as the Orbiting Carbon Observatory (OCO) instrument series. The original OCO was scheduled to launch in February 2009, but was unsuccessful due to a launch vehicle failure and was replaced by OCO-2, which was launched in July 2014 [1]. OCO-3, assembled with spare materials from OCO-2 development, launched in May 2019 and resides onboard the International Space Station (ISS).

Because they rely on reflected sunlight, passive spectrometers have limited conditions under which they can collect data. To observe the regional distribution of $CO_2$ sources and sinks, satellite measurements of $CO_2$ mixing ratios must be precise to 1 ppm by volume, have a spatial resolution of 300 km, and a monthly temporal resolution [2]–[4]. These requirements cannot be met by passive spectrometers and necessitate a different sensor technology. This is where lidar comes in to play.

NASA does not currently have any absorption spectroscopy lidars in orbit, but there are satellite lidar Earth science missions monitoring ice and ocean levels, vegetation, aerosols, clouds, and wind. The NASA mission Lidar in Space Technology Experiment (LITE), operational during September 1994, was the first space-based lidar for Earth science sensing [5]. The ICESat mission in operation from 2003-2010 was the first Earth orbiting precision laser altimeter [6]. The Cloud-Aerosol Lidar and Infrared Pathfinder Satellite Observation (CALIPSO) system was launched in 2006, making it the longest space-based atmospheric lidar in operation [7]. January 2015 saw the launch of the Cloud-Aerosol Transport System

(CATS) lidar. Onboard the ISS, CATS made observations of cloud and aerosol layers until October 2017 [8]. ICESat-2 launched in September 2018. The Advanced Topographic Laser Altimeter System (ATLAS) lidar altimeter onboard the ICESat-2 sends laser pulses at a rate 250 times that of the lidar on the first ICESat [9]. Also launched in 2018, the Global Ecosystem Dynamics Investigation (GEDI) instrument onboard the ISS gave us the first high-resolution data on the vertical structure of forests [10].

The China National Space Administration launched the Atmospheric Environment Monitoring Satellite (AEMS), also known as DQ-1, on April 15th 2022. Onboard AEMS is the world's first $CO_2$ lidar system, a pulsed dual-wavelength differential absorption system operating around 1572 nm [11]. The next closest differential absorption lidar mission scheduled to launch is the Methane Remote Sensing Lidar Mission (MERLIN) with a planned launch in 2024 [12]. MERLIN is a collaboration between the German and French space agencies DLR and CNES. At NASA Goddard Space Flight Center (GSFC), an integrated path differential absorption (IPDA) $CO_2$ lidar system is in development under the Active Sensing of $CO_2$ Emissions over Nights, Days, and Seasons (ASCENDS) mission. The present work, in collaboration with the team at NASA GSFC, uses the design of the ASCENDS IPDA lidar in a photonic integrated circuit [13]–[19].

## 2.2 Photonic Integration Methods

Figure 2.1 gives the approximate operational wavelength ranges for various photonic material platforms along with some important atmospheric absorption lines. The solid lines

indicate group III-V compound semiconductor platforms that have optical gain and, therefore, can be fully monolithic, integrating both active and passive functions. Indium phosphide (InP)-based photonic integration is the most mature monolithic platform due to its importance in the telecommunications industry. The InP-based material systems typically covers wavelengths in the range of 1.2 - 1.6 $\mu$m which includes the important telecom wavelengths of 1.31 $\mu$m and 1.55 $\mu$m, used for short and long reach optical fiber communications, respectively. Recent work has been done to extend InP-based PICs up to 2 $\mu$m [20], [21].

For a monolithic PIC, the ideal epitaxial material layer structure for a laser is not the same as the ideal structure for a modulator or a purely passive waveguide. Therefore, multiple methods for integrating passive and active component structures have been developed and are covered in the sections below. Figure 2.2 illustrates the main active/passive integration methods for group III-V compound semiconductor PICs, with material structure cross-sections being parallel to the direction of light propagation.

The dotted lines in Figure 2.1 indicate passive waveguide platforms with transparency in the near- to mid-infrared region. These passive platforms are important for their CMOS-compatibility, low optical loss, and phase modulators. In order to take advantage of the best that group III-V compound semiconductor and passive platforms have to offer, multiple hybrid integration methods have been developed.

The following sections give a brief overview of various active/passive photonic integration methods.
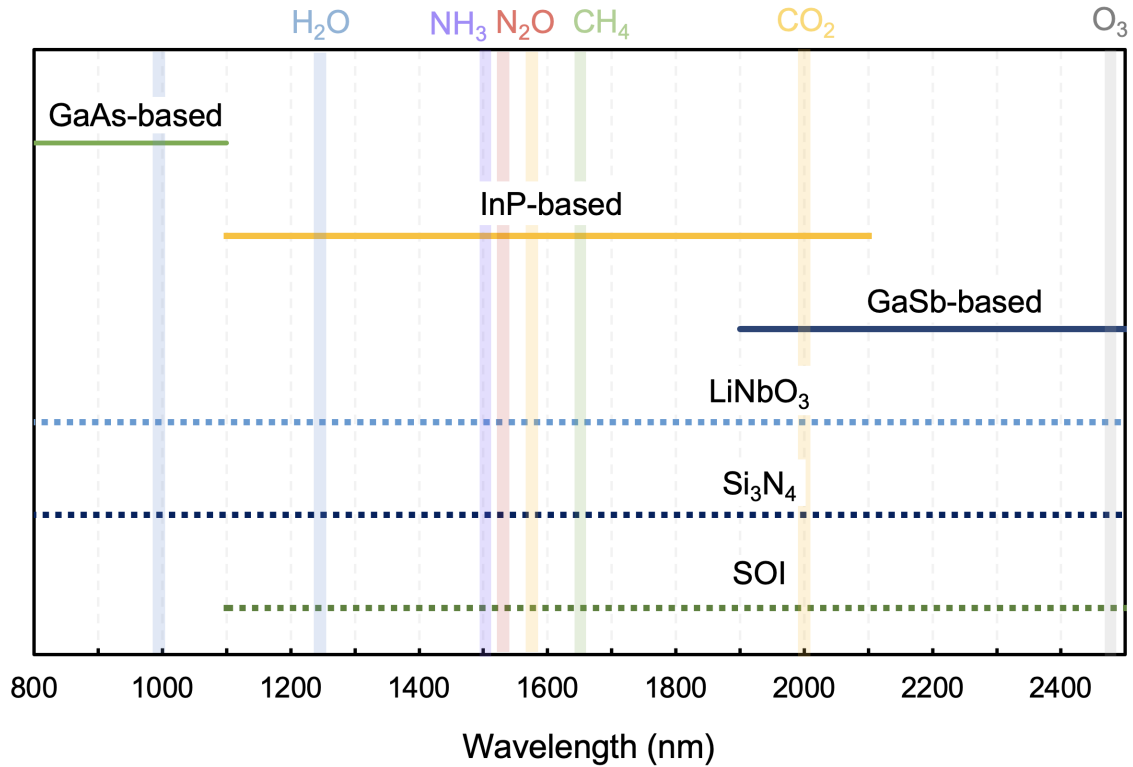
Figure 2.1: Approximate operational wavelength ranges of photonic material platforms in the near- to mid-infrared. The dotted lines indicate passive platforms with waveguide loss <1-2 dB/cm. [20]–[35]

**Butt-Joint Growth**

In the case of butt-joint growth (BJG), illustrated in the top left of Figure 2.2, an initial structure is epitaxially grown with layers optimized for the active devices. The InGaAsP multiquantum well (MQW) layers provide optical gain and the surrounding quaternary layers (depicted in yellow) help confine the optical mode. The layer-by-layer crystal growth (epitaxial growth) is most commonly accomplished by molecular beam epitaxy (MBE) or metalorganic chemical vapor deposition (MOCVD), which was used in this work. After the initial structure is grown, the active waveguide layers are selectively etched away and a second growth, or regrowth, is performed to form the passive region layers. The passive regions are
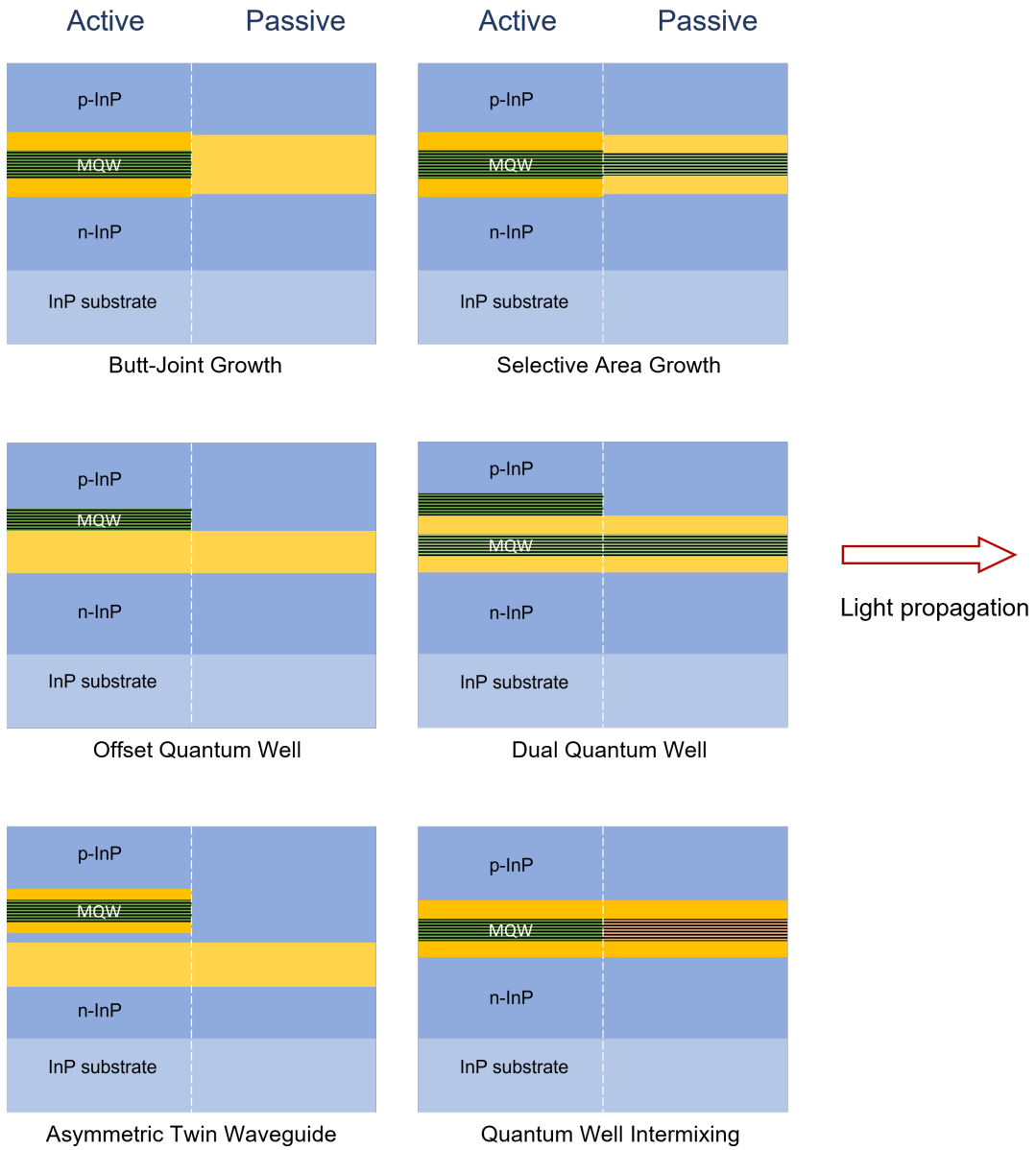
12

Figure 2.2: Illustration of active/passive integration methods in group III-V compound semiconductor photonic platforms.

designed with a larger bandgap than the active regions to reduce the optical loss. A final regrowth is used to form the p-doped cladding. When designing the p-dopant concentration profile, there is a tradeoff between efficient carrier transport and optical loss. Since the main advantage of BJG is the epilayer customization for each device type, this is often continued for the p-side cladding through the use of a separate regrowth for the active and passive regions with doping profiles optimized for each. To take full advantage of the BJG method, the number of regrowths can quickly add up, which can also create yield issues.

**Selective Area Growth**

For selective area growth (SAG), the wafer is patterned with a dielectric mask before the waveguide and MQW growth. Because the transport properties of the growth reactants are affected by the proximity and fill-factor of the dielectric pattern, multiple bandgap energies can be realized across the wafer in a single growth. The main drawback of SAG are limitations in the range of bandgaps that can be achieved and that the dielectric mask must be must be very carefully calibrated to achieve the desired result.

**Offset Quantum Well**

The offset quantum well (OQW) method, as the name implies, features a MQW stack grown on top of a waveguiding layer, rather than centered in the waveguiding layer. Although some optical mode overlap with the quantum wells (QWs) is sacrificed, the offset wells can be selectively etched away in the passive regions to create the active/passive interface. Unlike BJG and SAG, a single waveguide layer is continuous through all active and passive regions.

This is a disadvantage in that it creates a direct tradeoff between modulator efficiency and passive loss. The modulator efficiency is also reduced due to the lack of QWs in modulator regions. On the plus side, there are no regrowth interfaces at the center of the optical mode and only a single p-side regrowth is required. The step created by the etched MQW stack introduces only a small reflection loss at the active/passive interfaces.

**Dual Quantum Well**

The dual quantum well (DQW) approach is similar to OQW integration, but trades more efficient modulation for higher passive loss by including a MQW stack centered in the waveguide layer in addition to the offset wells.

**Asymmetric Twin Waveguide**

Asymmetric twin waveguide (ATG) integration, also called vertical integration, makes use of two separate vertically stacked waveguides and carefully designed mode conversion regions to couple the light from one waveguide to the other. The number of stacked waveguides is limited by the total layer strain and the insertion loss and length of the transitions between layers.

**Quantum Well Intermixing**

Finally, the quantum well intermixing (QWI) method uses incorporation of defects and a high temperature anneal to induce exchange of atoms between the quantum wells and barriers, resulting in a blueshift of the MQW photoluminescence (PL). A typical method is ion

implantation into a sacrificial cap layer [36]. Multiple MQW bandgaps can be defined across the sample using this method. The bandgap does not shift in areas protected from the implant with a hard mask. Removal of the sacrificial cap layer halts the blue shift during annealing. Therefore, an initial anneal could be followed by removal of the sacrificial cap in certain areas, followed by another anneal to further blue shift the areas that still have the cap. Since no regrowth or etching is required to create the transition between the active and passive regions, the transition loss is negligible. Optimization of the implant and anneal process to obtain repeatable and accurate PL shift across and between samples is required.

**Heterogeneous Integration**

Heterogeneous integration allows access to a large span of wavelengths in the near- to mid-infrared regions by allowing the mixing and matching of different material platforms. Heterogeneous integration methods vary from flip-chip soldering different chips to a common carrier to direct wafer bonding to crystal growth on nontraditional substrates and others [37]–[40]. Heterogeneous integration is a promising approach for providing all of the needed functionality in gas sensing PICs, but the various methods require specialized tooling and expert knowledge in the given process.

## 2.3 PIC-Based Gas Spectroscopy

### 2.3.1 Review of Photonic Integrated Gas Sensors

Photonic integrated circuits for compact biomedical, chemical, and environmental sensors have been identified as a key future technology for science and defense [41], [42]. One active area of research is waveguide enhanced gas sensors, where the gas or vapor analyte is contained on-chip in a flow channel or capsule where it interacts with an evanescent waveguide mode. Furthermore, functionalization of the waveguide surface can provide selective detection of analyte species. To accommodate a large wavelength range and interaction length, low loss silicon-on-insulator (SOI) or silicon nitride ($Si_3N_4$) waveguides, which are also CMOS compatible, are typically used for this application [42]–[44]. In 2020, researchers at Ghent University and the Vienna University of Technology demonstrated parts-per-billion (ppb) detection limits for on-chip measurement of acetone, isopropyl alcohol, and ethanol by monitoring refractive index variation using an unbalanced Mach-Zehnder interferometer [45]. Waveguide enhanced Raman spectroscopy (WERS) is of special interest and was notably demonstrated in 2018 by a collaboration with the Naval Research Laboratory to achieve sub-ppb detection of analytes that simulated chemical warfare agents [46], [47]

The transparency range of SOI and silicon nitride waveguides allows wavelength flexibility for detecting various species, but an off-chip laser source is required for these platforms. In 2019, researchers at the IBM T. J. Watson Research Center and Princeton Univer-

sity published an on-chip spectroscopic sensor for 1650 nm methane detection comprising an InP-based SOA and detector array flip-chip bonded to a silicon photonic chip [48]. The sensor yielded performance comparable to conventional free-space tunable diode laser spectroscopy (TDLAS) systems.

Hybrid integration of III-V gain materials with silicon nitride or silicon waveguides via wafer bonding allows the alignment and coupling between the active and passive regions to be defined by the processing and lithography rather than a pick-and-place process. Recent work, namely at Ghent University and University of California, Santa Barbara, in hybrid integration for TDLAS has focused on the 2-4 $\mu$m wavelength range where there are many molecular absorption lines of interest [49]–[53].

Interest in fully monolithic PICs for gas sensing has mainly targeted applications using wavelengths around the important telecommunications O- and C-bands because the InP-based PIC technology in this wavelength range is very mature [54]. Efforts to extend InP-based PIC technology to wavelengths around 2 $\mu$m is ongoing [20], [21], [55]–[58]. Researchers at Eindhoven University of Technology have demonstrated 2 $\mu$m InP-based tunable lasers using InGaAs quantum wells and barriers, but they are limited in tuning range, output power, and stability [20]. TDLAS has been demonstrated using monolithic InP lasers around 1550 nm to measure the absorption lines of acetylene at 1520 nm [59], hydrogen cyanide at 1555 nm [60], ammonia at 1522 nm [61], and methane at 1650 nm [62], [63].

The integrated laser demonstrations cited above showed absorption line scanning for TDLAS or IPDA measurements, but did not integrate all of the optical functions needed

18

for a lidar system, as demonstrated in the present work. Since the start of the work in this dissertation, a PIC for 1572 nm $CO_2$ absorption spectroscopy using a random-modulation continuous-wave (RM-CW) differential absorption lidar (DIAL) was developed at the Technical University of Madrid, Spain [64]–[66]. The PIC contains three DBR lasers: a reference laser maintained at 1572 nm and two lasers used for the $CO_2$ measurement, one having an emission wavelength on the absorption line and one with an emission wavelength off of the absorption line. Integrated semiconductor optical amplifiers (SOAs), photodiodes, and electro-absorption modulators (EAMs) are used to control the output power of the lasers, detect the beat notes between lasers for stabilization, and implement the pseudorandom modulation, respectively. The PIC was fabricated in a multi-project wafer run at SMART Photonics. Due to optical feedback, the lasers were not able to be tuned and stabilized with control electronics to demonstrate the full PIC functionality.

### 2.3.2   InP PIC for $CO_2$ Spectroscopy at 1572 nm

As described previously, the lidar system consists of two lasers, a phase modulator, high-speed photodetector, an intensity modulator for pulsing, and several optical combiners and splitters for routing the light. The team at NASA Goddard chose the 1572.335 nm absorption line of $CO_2$ for the ASCENDS lidar because it aligns closely with the important telecommunications wavelength of 1550 nm. This allowed the use of mature commercial-off-the-shelf (COTS) components when building the system. Similarly, the InP-based PIC platform enables devices that operate in the communications C- and O-bands. Because of this, InP de-

vices and PICs are very mature, having been developed for optical transceivers. In addition, active and passive components can be integrated together on a single substrate. Various hybrid integrated platforms use direct bandgap group III-V compound semiconductors to implement active and passive components in a single chip, but the fabrication methods are complex and under development. For these reasons, an InP-based PIC platform was chosen for integrating the $CO_2$ lidar system.

## 2.4    Chapter Summary

Chapter 2 reviewed past and current Earth science lidar satellites, photonic material and integration platforms relevant to near- and mid-infrared wavelengths for gas sensing and spectroscopy, and recent work in PICs for gas sensing. As of this writing, one satellite has been launched with a differential absorption lidar instrument for atmospheric gas detection, with at least two more in development, including the NASA ASCENDS mission for $CO_2$ measurement. Although there has been rapidly growing interest in PICs for gas sensing and spectroscopy applications within the past few years, the only other attempt at a fully integrated DIAL PIC suffered from detrimental optical feedback, preventing demonstration of active wavelength tuning and stabilization for sensing [65] .

# References

[1] NASA, *Orbiting carbon observatory*, https : / / www . jpl . nasa . gov / missions / orbiting-carbon-observatory-oco, Accessed: 2022-05-08.

[2] R. J. Engelen, A. S. Denning, K. R. Gurney, and G. L. Stephens, "Global observations of the carbon budget: 1. expected satellite capabilities for emission spectroscopy in the eos and npoess eras," *Journal of Geophysical Research*, vol. 106, pp. 20 055–20 068, 2001.

[3] P. J. Rayner and D. M. O'Brien, "The utility of remotely sensed co2 concentration data in surface source inversions," *Geophysical Research Letters*, vol. 28, pp. 175–178, 2001.

[4] C. E. Miller, D. Crisp, P. L. DeCola, S. C. Olsen, J. T. Randerson, A. M. Michalak, A. Alkhaled, P. Rayner, D. J. Jacob, P. Suntharalingam, D. B. A. Jones, A. S. Denning, M. E. Nicholls, S. C. Doney, S. Pawson, H. Boesch, B. J. Connor, I. Y. Fung, D. O'Brien, R. J. Salawitch, S. P. Sander, B. Sen, P. Tans, G. C. Toon, P. O. Wennberg, S. C. Wofsy, Y. L. Yung, and R. M. Law, "Precision requirements for space-based xco2 data," *Journal of Geophysical Research*, vol. 112, 2007.

[5] NASA, *Lite: Measuring the atmosphere with laser precision*, https://www.nasa.gov/centers/langley/news/factsheets/LITE.html, Accessed: 2022-05-08.

[6] X. Sun, J. B. Abshire, J. F. McGarry, G. A. Neumann, J. C. Smith, J. F. Cavanaugh, D. J. Harding, H. J. Zwally, D. E. Smith, and M. T. Zuber, "Space lidar developed at the nasa

goddard space flight center—the first 20 years," *IEEE Journal of Selected Topics in Applied Earth Observations and Remote Sensing*, vol. 6, no. 3, pp. 1660–1675, 2013.

[7]  NASA, *World class lidar science*, https://science.larc.nasa.gov/lidar/, Accessed: 2022-05-08.

[8]  NASA, *Cats*, https://cats.gsfc.nasa.gov/, Accessed: 2022-05-08.

[9]  NASA, *Icesat-2*, https://icesat-2.gsfc.nasa.gov/space-lasers, Accessed: 2022-05-08.

[10]  University of Maryland, *Gedi*, https://gedi.umd.edu/, Accessed: 2022-05-08.

[11]  OSCAR, *Acdl: Aerosol and carbon detection lidar*, https://space.oscar.wmo.int/instruments/view/acdl, Accessed: 2022-05-08.

[12]  CNES, *Merlin*, https://merlin.cnes.fr/en/MERLIN/index.htm, Accessed: 2022-05-08.

[13]  K. Numata, J. R. Chen, S. T. Wu, J. B. Abshire, and M. A. Krainak, "Frequency stabilization of distributed-feedback laser diodes at 1572 nm for lidar measurements of atmospheric carbon dioxide," *Applied Optics*, vol. 50, no. 7, pp. 1047–1056, 2011.

[14]  K. Numata, J. R. Chen, and S. T. Wu, "Precision and fast wavelength tuning of a dynamically phase-locked widely-tunable laser," *Optics Express*, vol. 20, no. 13, 2012.

[15]  J. R. Chen, K. Numata, and S. T. Wu, "Error analysis for lidar retrievals of atmospheric species from absorption spectra," *Optics Express*, vol. 27, no. 25, pp. 36 487–36 504, 2019.

[16] J. R. Chen, K. Numata, and S. T. Wu, "Error reduction in retrievals of atmospheric species from symmetrically measured lidar sounding absorption spectra," *Optics Express*, vol. 22, no. 21, pp. 26 055–26 075, 2014.

[17] G. R. Allan, J. B. Abshire, H. Riris, M. Jianping, W. E. Hasselbrack, K. Numata, J. Chen, R. Kawa, M. Rodriguez, and M. Stephen, "Lidar measurements of co2 column concentrations in the arctic region of north america from the ascends 2017 airborne campaign," *SPIE Asia-Pacific Remote Sensing Conference*, vol. 10779, 2018. DOI: `10.1117/12.2325908`.

[18] J. B. Abshire, A. K. Ramanathan, H. Riris, G. R. Allan, X. Sun, W. E. Hasselbrack, J. Mao, S. Wu, J. Chen, K. Numata, S. R. Kawa, M. Y. M. Yang, and J. DiGangi, "Airborne measurements of co2 column concentrations made with a pulsed ipda lidar using a multiple-wavelength-locked laser and hgcdte apd detector," *Atmospheric Measurement Techniques*, vol. 11, pp. 2001–2025, 2018. DOI: `https://doi.org/10.5194/amt-11-2001-2018`.

[19] J. Mao, A. Ramanathan, J. B. Abshire, S. R. Kawa, H. Riris, G. R. Allan, M. Rodriguez, W. E. Hasselbrack, X. Sun, K. Numata, J. Chen, Y. Choi, and M. Y. M. Yang, "Measurement of atmospheric co2 column concentrations to cloud tops with a pulsed multi-wavelength airborne lidar," *Atmospheric Measurement Techniques*, vol. 11, pp. 127–140, 2018. DOI: `https://doi.org/10.5194/amt-11-127-2018`.

[20] S. Latkowski, A. Hansel, P. J. van Veldhoven, D. D'Agostino, H. Rabbani-Haghighi, B. Docter, N. Bhattacharya, P. J. A. Thijs, H. P. M. M. Ambrosius, M. K. Smit, K. A. Williams,

and E. A. J. M. Bente, "Monolithically integrated widely tunable laser source operating at 2 $\mu$m," *Optica*, vol. 3, no. 12, 2016. DOI: 10.1364/OPTICA.3.001412.

[21]   T. Tanbun-Ek, Z. Xu, and J. Mott, "Advancements in broad area inp based high power lasers operating from 1100 nm to 2100 nm," *IEEE International Semiconductor Laser Conference (ISLC)*, 2018. DOI: 10.1109/ISLC.2018.8516195.

[22]   T. Delahaye, S. E. Maxwell, Z. D. Reed, H. Lin, J. T. Hodges, K. Sung, V. M. Devi, T. Warneke, P. Spietz, and H. Tran, "Precise methane absorption measurements in the 1.64 micron spectral region for the merlin mission," *Journal of Geophysical Research Atmospheres*, vol. 121, no. 12, pp. 7360–7370, 2016. DOI: 10.1002/2016JD025024.

[23]   V. Romaniello, C. Spinetti, M. Silvestri, and M. F. Buongiorno, "A sensitivity study of the 4.8 micron carbon dioxide absorption band in the mwir spectral range," *Remote Sensing*, vol. 12, no. 172, pp. 10 501–10 519, 2020. DOI: 10.3390/rs12010172.

[24]   J. K. Valiunas, G. Stewart, and G. Das, "Detection of nitrous oxide (n2o) at sub-ppmv using intracavity absorption spectroscopy (icas)," *IEEE Photonics Technology Letters*, vol. 28, no. 3, pp. 359–362, 2016.

[25]   T. Hosoda, G. Kipshidze, G. Tsvid, L. Shterengas, and G. Belenky, "Type-i gasb-based laser diodes operating in 3.1- to 3.3-$\mu$ wavelength range," *IEEE Photonic Technology Letters*, vol. 22, no. 10, pp. 718–720, 2010.

[26]   A. Vizbaras, E. Dvinelas, A. Trinkunas, I. Simonyte, M. K. Greibus, T. Zukauskas, R. Songaila, and K. Vizbaras, "High-performance mid-infrared gasb laser diodes for de-

fense and sensing applications," *SPIE Laser Technology for Defense and Security X,* vol. 9081, 2014.

[27] B.-C. Gao and Y. J. Kaufman, "Water vapor retrievals using moderate resoluation imaging spectroradiometer (modis) near-infrared channels," *Journal of geophysical research,* vol. 108, no. D13, 2003. DOI: 10.1029/2002JD003023.

[28] O. E. Garcia, M. Schneider, F. Hase, T. Blumenstock, E. Sepulveda, and Y. Gonzalez, "Quality assessment of ozone total column amounts as monitored by ground-based solar absorption spectrometry in the near infrared (>3000 cm−1)," *Atmospheric Measurement Techniques,* vol. 7, pp. 3071–3084, 2014. DOI: 10.5194/amt-7-3071-2014.

[29] X. Guo, F. Zheng, C. Li, X. Yang, N. Li, S. Liu, J. Wei, X. Qiu, and Q. He, "A portable sensor for in-situ measurement of ammonia based on near-infrared laser absoprtion spectroscopy," *Optics and Lasers in Engineering,* vol. 115, pp. 243–248, 2019.

[30] R. Soref, "Mid-infrared photonics in silicon and germanium," *Nature Photonics,* vol. 4, 2010.

[31] Y. Su, Y. Zhang, C. Qiu, X. Guo, and L. Sun, "Silicon photonic platform for passive waveguide devices: Materials, fabrication, and applications," *Advanced Materials Technologies,* vol. 5, 2010.

[32] D. J. Blumenthal, R. Heideman, D. Geuzebroek, A. Leinse, and C. Roeloffzen, "Silicon nitride in silicon photonics," *Proceedings of the IEEE,* vol. 106, no. 12, 2018.

[33] K. Worhoff, R. G. Heideman, A. Leinse, and M. Hoekman, "Triplex: A versatile dielectric photonic platform," *Advanced Optical Technologies*, vol. 4, no. 2, pp. 189–207, 2015.

[34] F. Pavanello, R. Wang, and G. Roelkens, "Iii-v/si mid-ir photonic integrated circuits," *Mid-infrared optoelectronics*, pp. 567–594, 2020.

[35] L. A. Coldren, S. W. Corzine, and M. L. Masanovic, *Diode Lasers and Photonic Integrated Circuits, 2nd Edition*. Hoboken, NJ: John Wiley and Sons, Inc., 2012.

[36] E. J. Skogen, J. W. Raring, G. B. Morrison, C. S. Wang, V. Lal, M. L. Masanovic, and L. A. Coldren, "Monolithically integrated active components: A quantum well intermixing approach," *IEEE Journal of Selected Topics in Quantum Electronics*, vol. 11, no. 2, pp. 343–355, 2005.

[37] B. Song, S. Tommaso Suran-Brunelli, S. Zhu, and J. Klamkin, "Low dark current and high speed ingaas photodiode on cmos-compatible silicon by heteroepitaxy," *IEEE Journal of Selected Topics in Quantum Electronics*, vol. 28, no. 2, 2022.

[38] B. Song, L. Megalini, S. Dwivedi, S. Ristic, and J. Klamkin, "High-thermal performance 3d hybrid silicon lasers," *IEEE Journal of Selected Topics in Quantum Electronics*, vol. 29, no. 14, 2017.

[39] T. Komljenoivic, D. Huang, P. Pintus, M. A. Tran, M. L. Davenport, and J. E. Bowers, "Photonic integrated circuits using heterogeneous integration on silicon," *Proceedings of the IEEE*, vol. 106, no. 12, pp. 2246–2257, 2018.

[40] M. R. Billah, M. Blaicher, T. Hoose, P.-I. Dietrich, P. Marin-Palomo, N. Lindenmann, A. Nesic, A. Hofmann, U. Troppenze, M. Moehrle, S. Randel, W. Freude, and C. Koos, "Hybrid integration of silicon photonics circuits and inp lasers by photonic wire bonding," *Optica*, vol. 5, no. 7, pp. 876–883, 2018.

[41] R. Chandrasekar, Z. J. Lapin, A. S. Nichols, R. M. Braun, and A. W. Fountain, "Photonic integrated circuits for department of defense-relevant chemical and biological sensing applications: State-of-the-art and future outlooks," *Optical Engineering*, vol. 58, no. 2, 2019.

[42] R. Baets, A. Z. Subramanian, A. Dhakal, S. K. Selvaraja, K. Komorowska, F. Peyskens, E. Ryckeboer, N. Yebo, G. Roelkens, and N. Le Thomas, "Spectroscopy-on-chip applications of silicon photonics," in *Proc. of SPIE*, ser. Integrated Optics: Devices, Materials, and Technologies XVII, 2013. DOI: 10.1117/12.2010498.

[43] H. Zhao, S. Clemmen, A. Raza, and R. Baets, "Stimulated raman spectroscopy of analytes evanescently probed by a silicon nitride photonic integrated waveguide," *Optics Letters*, vol. 43, no. 6, 2018. DOI: 10.1364/OL.43.001403.

[44] N. F. Tyndall, T. H. Stievater, D. A. Kozak, M. W. Pruessner, W. S. Rabinovich, N. M. Fahrenkopf, A. O. Antohe, and K. A. McComber, "A low-loss sin photonic integrated circuit foundry platform for waveguide-enhanced raman spectroscopy," in *Proc. of SPIE*, ser. Smart Photonic and Optoelectronic Integrated Circuits XXIII, 2021. DOI: 10.1117/12.2582529.

[45]   G. Antonacci, J. Goyvaerts, H. Zhao, B. Baumgartner, B. Lendl, and R. Baets, "Ultra-sensitive refractive index gas sensor with functionalized silicon nitride photonic circuits," *APL Photonics*, vol. 5, pp. 081301-1-081301–5, 2020. DOI: 10.1063/5.0013577.

[46]   T. H. Stievater, K. Koo, N. F. Tyndall, S. A. Holmstrom, D. A. Kozak, P. G. Goetz, R. A. McGill, and M. W. Pruessner, "Chemical sensors fabricated by a photonic integrated circuit foundry," in *Proc. of SPIE*, ser. Frontiers in Biological Detection: From Nanosensors to Systems X, 2018. DOI: 10.1117/12.2294059.

[47]   S. A. Holmstrom, T. H. Stievater, D. A. Kozak, M. W. Pruessner, N. Tyndall, W. S. Rabinovich, R. A. McGill, and J. B. Khurgin, "Trace gas raman spectroscopy using functionalized waveguides," *Optica*, vol. 3, no. 8, 2016. DOI: 10.1364/OPTICA.3.000891.

[48]   C. Xiong, Y. Martin, E. J. Zhang, J. S. Orcutt, M. Glodde, L. Schares, T. Barwicz, C. C. Teng, G. Wysocki, and W. M. J. Green, "Silicon photonic integrated circuit for on-chip spectroscopic gas sensing," in *Proc. of SPIE*, ser. Silicon Photonics XIV, 2019. DOI: 10.1117/12.2511793.

[49]   R. Wang, M. Muneeb, A. Vasiliev, A. Malik, S. Sprengel, G. Boehm, I. Simonyte, A. Vizbaras, K. Vizbaras, R. Baets, M.-C. Amann, and G. Roelkens, "Iii-v/silicon photonic integrated circuits for spectroscopic sensing in the 2 $\mu$m wavelength range," in *Proc. of SPIE*, ser. Smart Photonic and Optoelectronic Integrated Circuits XX, 2018. DOI: 10.1117/12.2287380.

[50]   N. Hattasan, L. Cerutti, J. B. Rodriguez, E. Tournie, D. van Thourhout, and G. Roelkens, "Heterogeneous gasb/soi mid-infrared photonic integrated circuits for spectroscopic

applications," in *Proc. of SPIE*, ser. Quantum Sensing and Nanophotonic Devices VIII, 2011. DOI: 10.1117/12.874659.

[51]  R. Wang, S. Sprengel, A. Vasiliev, G. Boehm, J. Van Campenhout, G. Lepage, P. Verheyen, R. Baets, M.-C. Amann, and G. Roelkens, "Widely tunable 2.3 $\mu$m iii-v-on-silicon vernier lasers for broadband spectroscopic sensing," *Photonics Research*, vol. 6, no. 9, pp. 858–866, 2018. DOI: 10.1364/PRJ.6.000858.

[52]  R. Wang, A. Vasiliev, M. Muneeb, A. Malik, S. Sprengel, G. Boehm, M.-C. Amann, I. Simonyte, A. Vizbaras, K. Vizbaras, R. Baets, and G. Roelkens, "Iii-v-on-silicon photonic integrated circuits for spectroscopic sensing in the 2-4 $\mu$m wavelength range," *MDPI Sensors*, vol. 17, 2017. DOI: 10.3390/s17081788.

[53]  A. Spott, "Heterogeneous integrationg of mid-infrared lasers on silicon," Ph.D. dissertation, University of California, Santa Barbara, 2018.

[54]  A. Hansel and M. J. R. Heck, "Feasibility of telecom-wavelength photonic integrated circuits for gas sensors," *MDPI Sensors*, vol. 18, 2018. DOI: 10.3390/s18092870.

[55]  S. Latkowski, K. A. Williams, and E. A. J. M. Bente, "Monolithically integrated laser sources for applications beyond telecommunications," in *Proc. of SPIE*, ser. Physics and Simulation of Optoeletronic Devices XXVIII, 2020. DOI: 10.1117/12.2552784.

[56]  A. Latkowski, P. J. van Veldhoven, A. Hansel, D. D'Agostino, H. Rabbani-Haghighi, B. Docter, N. Bhattacharya, P. Thijs, H. Ambrosius, M. Smit, K. Williams, and E. A. J. M. Bente, "Indium phosphide monolithic photonic integrated circuits for gas sensing applications," in *18th European Conference on Integrated Optics (ECIO)*, 2016.

[57] D. D'Agostino, M. S. Tahvili, S. Latkowski, P. J. van Veldhoven, H. Rabbani-Haghighi, C. Jin, B. Docter, H. P. M. M. Ambrosius, E. A. J. M. Bente, D. Lenstra, and M. K. Smit, "Monolithically integrated widely tunable coupled cavity laser source for gas sensing applications around 2.0 $\mu$m wavelength," in *OSA Advanced Photonics*, 2015.

[58] A. Latkowski, A. Hansel, D. D'Agostino, P. J. van Veldhoven, H. Rabbani-Haghighi, B. Docter, N. Bhattacharya, P. J. A. Thijs, H. P. M. M. Ambrosius, M. K. Smit, K. A. Williams, and E. A. J. M. Bente, "Long wavelength monolithic photonic integration technology for gas sensing applications," in *International Conference on Transparent Optical Networks (ICTON)*, 2016.

[59] S. Latkowski, A. Hansel, N. Bhattacharya, T. de Vries, L. Augustin, K. Williams, M. Smit, and E. Bente, "Novel widely tunable monolithcally integrated laser source," *IEEE Photonics Journal*, vol. 7, no. 6, 2015.

[60] A. Hansel and M. J. R. Heck, "Widely tunable laser on an inp photonic integrated circuit," *IEEE Photonics Technology Letters*, vol. 32, no. 2, 2020.

[61] A. Hansel, A. I. Adamu, C. Markos, A. Feilberg, O. Bang, and M. J. R. Heck, "Integrated ammonia sensor using a telecom photonic integrated circuit and a hollow core fiber," *MDPI Photonics*, vol. 7, no. 93, 2020. DOI: 10.3390/photonics7040093.

[62] G. Morrison, J. Sherman, S. Estrella, R. Moreira, and P. Leisher, "New semiconductor laser technology for gas sensing applications in the 1650nm range," in *Proc. of SPIE*, ser. Optical Engineering + Applications, 2017. DOI: 10.1117/12.2275215.

[63]    H. Riris, K. Numata, S. Wu, J. Sherman, and G. Morrison, "A new laser transmitter for methane and water vapor measurements at 1.65 $\mu$m," in *Proc. of SPIE*, ser. Defense + Commercial Sensing, 2020. DOI: 10.1117/12.2558816.

[64]    A. Perez-Serrano, C. Quevedo-Galan, V. R. Aguilera, P. Castera, J. M. G. Tijero, and I. Esquivias, "Differential absorption lidar transmitter based on a photonic integrated circuit for carbon dioxide sensing," in *OSA Frontiers in Optics*, 2021.

[65]    A. Perez-Serrano, C. Quevedo-Galan, V. R. Aguilera-Sanchez, J. M. G. Tijero, and I. Esquivias, "Differential absorption lidar transmitter based on an indium phosphide photonic integrated circuit for carbon dioxide sensing," *IEEE Journal of Selected Topics in Quantum Electronics*, vol. 28, no. 5, 2022.

[66]    M. Quatrevalet, X. Ai, A. Perez-Serrano, P. Adamiec, J. Barbero, A. Fix, J. M. G. Tijero, I. Esquivias, J. G. Rarity, and G. Ehret, "Atmospheric $co_2$ sensing with a random modulation continuous wave integrated path differential absorption lidar," *IEEE Journal of Selected Topics in Quantum Electronics*, vol. 23, no. 2, 2017. DOI: 10.1109/JSTQE.2016.2619325.

# Chapter 3

# Lidar Operation and PIC Layout

The photonic integrated circuit (PIC) design was adapted from the ASCENDS lidar system developed at NASA GSFC, which was built using commercial-off-the-shelf (COTS), fiber-coupled optical components. The ASCENDS system uses an integrated path differential absorption (IPDA) lidar, where transmission through the atmosphere of laser wavelengths spanning the absorption line yields the concentration of $CO_2$ in a given atmospheric column. At each laser wavelength step, the ASCENDS system emits a pulse before stepping to the next wavelength and emitting another pulse. Each pulse is separated in time by about 130 $\mu$s, which is the time it takes for each pulse to reach the ground from low Earth orbit (LEO), reflect, and return to an on-board photodetector, while preventing crosstalk from cloud scattering [1]. Figure 3.1 illustrates how the resulting train of laser pulses samples the absorption line. Multiple wavelength scans are averaged to increase accuracy.
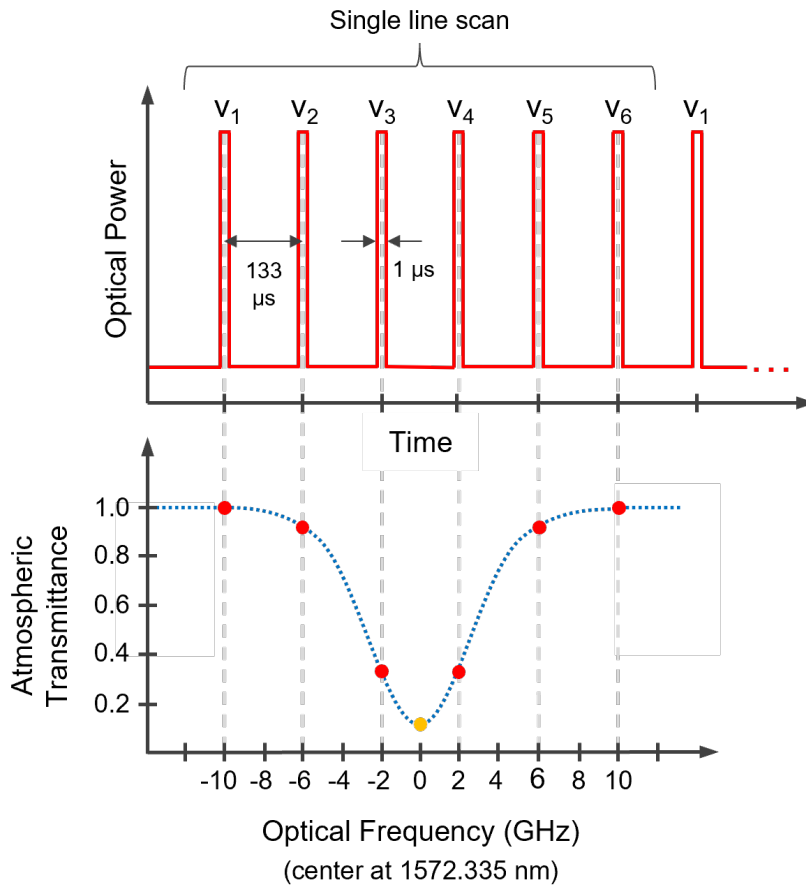
Figure 3.1: Cartoon diagram illustrating how the pulse train generated by the IPDA lidar system samples the $CO_2$ absorption line.

## 3.1 System Architecture

A general schematic of the lidar system is illustrated in Figure 3.2. Two lasers are used to achieve the desired output pulse train. The components in Figure 3.2 are purposefully generic for later discussion of integrated device selection. The wavelength of the first laser (the "leader laser") is maintained at 1572.335 nm through a frequency modulation locking technique using an optical phase modulator and a wavelength reference. Integrated or compact solutions are available for the wavelength reference, however the work presented

here uses a $CO_2$ Herriott gas cell borrowed from NASA. The second laser ("follower laser") is offset locked to the leader laser via an optical phase locked loop (OPLL). After the follower laser is locked at each frequency step, an intensity modulator generates a high extinction ratio pulse, resulting in the train of pulses in time and frequency illustrated at the top of Figure 3.1.
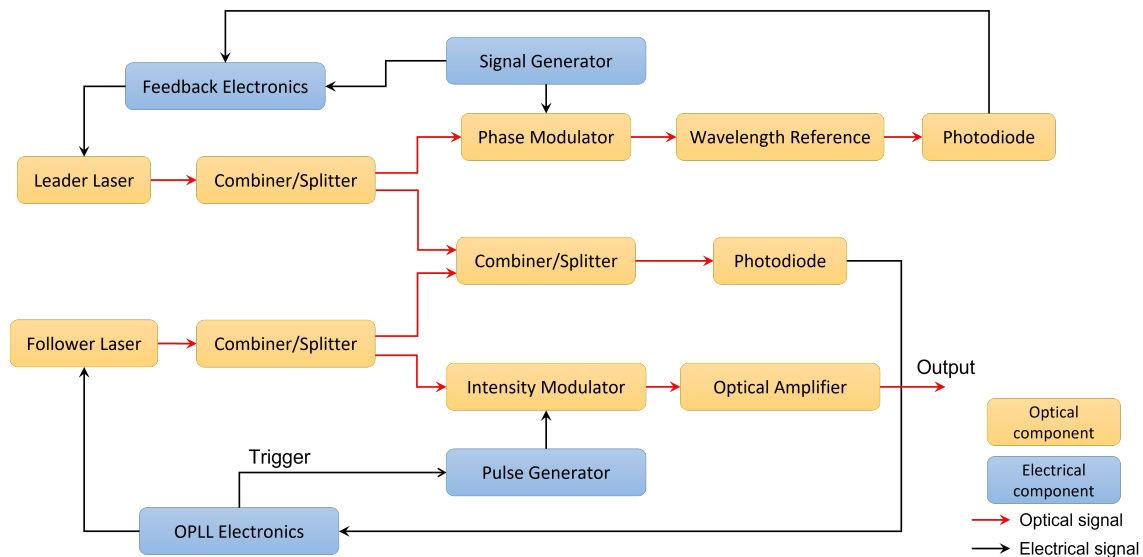


Figure 3.2: Schematic illustrating the overall operation of the IPDA lidar system.

## 3.2 PIC Component Selection

To best address the system requirements listed in Figure 3.3, two different photonic integration platforms were used to fabricate the PICs: offset quantum well (OQW) and quantum well intermixing (QWI). Compared to the QWI PICs, the OQW PICs have a simpler fabrication flow and, consequently, higher yield. Even though the QWI process is more complicated, it is easier to integrate distributed feedback (DFB) lasers and efficient modulators

| Parameter | Target value |
| --- | --- |
| Center wavelength | 1572.335 nm |
| Side-mode suppression ratio (SMSR) | 40 dB |
| Linewidth (over 1 µs) | < 50 MHz |
| Center wavelength drift (over 1 s) | < 100 MHz |
| Center wavelength standard deviation | < 3 MHz |
| Follower laser wavelength tuning | +/- 15 GHz |
| Pulse width | 1 µs |
| Pulse repetition rate | 7.5 kHz |
| Pulse extinction ratio | 35 dB |
| Peak pulse power | 10 mW |

Figure 3.3: Required specifications for the IPDA lidar system [1]–[4]

using QWI. This dissertation focuses on the design, fabrication, and performance of the QWI PICs. This section reviews the selection of integrated devices for each of the optical components shown in Figure 3.2.

### 3.2.1 Lasers

For the leader and follower lasers, the required linewidth, tuning, side mode suppression ratio (SMSR), and target wavelength must be considered. As stated above, the QWI platform allows easy integration of DFB lasers, which are narrow linewidth, single frequency lasers well suited for use as the leader laser in the lidar system. Although a DFB laser would meet all of the requirements for both the leader and follower lasers, the modelling and fabrication accuracy must be very high to target an exact wavelength. With thermal tuning and current injection, the DFB laser exhibits only a few nanometers of wavelength tuning and, ideally, the laser would operate in a low temperature, high current injection regime for the best

output power. Each laser in the PIC must also be able to meet the target wavelength at the same stage temperature as the other laser in the PIC. Therefore, if the material refractive indices used in the laser modelling and/or the period of the fabricated DFB grating mirror are not accurate, the DFB laser might not reach the target wavelength. To mitigate this risk, sampled grating distributed Bragg reflector (SGDBR) lasers were also included as leader and follower lasers in the QWI PICs. Although the wide continuous tuning range of an SGDBR laser (about 40 nm) is not needed for this specific application, an SGDBR laser can easily meet the linewidth and SMSR requirements, while being more tolerant to modelling and fabrication inaccuracies in terms of reaching the target wavelength.

### 3.2.2   Phase Modulator

For the phase modulator, the main concern is residual amplitude modulation (RAM), which limits the locking performance of the leader laser [5]–[7]. The required phase shift of $\pi$ radians and 125 MHz modulation speed are easily achievable. In indium phosphide (InP)-based phase modulators, some bias dependent absorption loss always accompanies the desired index change. Because of this, the RAM of an InP-based modulator will never match that of a lithium niobate phase modulator, but it can be mitigated. To explore this, a novel shift-and-dump phase shifter (SDPS) design that uses an unbalanced Mach-Zehnder architecture to compensate for loss in the modulated arm was implemented in some of the PICs [8], [9]. Chapter 6 gives details of the design and characterization of the phase modulators.

### 3.2.3   Photodiode

To meet the bandwidth requirement of at least 15 GHz for the integrated photodiode, the main considerations were the length of the photodiode and parasitic capacitance due to the contact pad area. The material layer structure in the photodiode region was the same as that in the laser gain and semiconductor optical amplifier (SOA) regions. Since there is a tradeoff between bandwidth and responsivity, several photodiode lengths were included in different PICs ranging from 20 to 50 $\mu$m long. Although a smaller contact pad is better for the photodiode bandwidth, the minimum pad size was limited by wire-bonding capabilities. Various pad sizes were also included for mitigating the risk associated with this tradeoff.

### 3.2.4   Intensity Modulator

For the intensity modulator, achieving an extinction ratio (ER) of at least 35 dB was the biggest challenge. The 7.5 kHz repetition rate and 1 $\mu$s pulse width are both easily met by conventional InP-based modulators. Typically, InP-based intensity modulators are either Mach-Zehnder modulators (MZMs) or electro-absorption modulators (EAMs). An MZM is an integrated Mach-Zehnder interferometer with a phase modulator in each arm. When one or both arms are modulated, constructive or destructive interference at the output waveguide results in an "on" or "off" level signal. InP MZMs are frequently used for high repetition rate pulse generation, but do not typically achieve a 35 dB ER, which is limited by bias dependent loss in the phase modulators and the accuracy of the 50/50 splitting ratio at the input splitter and output coupler. It is easier to achieve a high ER using an EAM, but

EAM insertion loss is high and requires a more complicated epitaxial design and/or fabrication process to add another band edge to the PIC. Therefore, a nontraditional approach was considered where an SOA was modulated in forward bias to produce a high ER pulse. Since the repetition rate is low and the pulse width is large for this PIC, the SOA response time is not a limiting factor. In addition, the SOA bias can be swept from reverse into forward for further increasing the ER. In the layout, PIC variations with only SOAs and with an MZM followed by an SOA were both included.

### 3.2.5   Couplers

For splitting and combining light in the PIC, two types of couplers were considered. Mulitmode interference (MMI) couplers use the self-imaging effect in a multimode waveguide to split or combine light with a 50/50 ratio. Although MMI couplers are simple to design and fabricate, they are typically limited to a 50/50 splitting ratio and introduce unwanted reflections, which could degrade the performance of the PIC. Directional couplers use two parallel waveguides with a chosen spacing and length to achieve an arbitrary coupling ratio and do not suffer from parasitic back reflections, but they are relatively difficult to fabricate. Although no specific splitting ratio is required for the PIC operation, it is advantageous to send most of the light from the leader and follower lasers to the phase modulator and intensity modulator, respectively, to meet the performance requirements. Since MMI and directional couplers both have their advantages and disadvantages, PICs were fabricated with all MMI couplers, all directional couplers, and with a combination of both.

## 3.3  Mask Layout

To incorporate many variations in PIC design, two QWI mask sets were generated in the latest fabrication generation, as shown in Figure 3.4. Between the two mask layouts, there are 13 different PIC designs. When laying out the masks, many considerations went into making the final PICs a success. Firstly, the PICs were made to be as short as possible, which was important for several reasons. The PICs were fabricated on quarters of a 2" InP wafer, so the area per sample was limited. As the PIC length (and, consequently, die size) gets larger, there are fewer devices per sample and it becomes harder to produce a fully operational individual PIC. The larger the PIC footprint, the more likely it is for a defect to occur somewhere in any given PIC. In addition, a large length:width ratio makes it difficult to cleave out individual PICs without them cracking or breaking. And finally, it is beneficial for the operation of the PIC to keep the total passive waveguide length as small as possible to keep the optical losses low.

The PIC length is mainly limited by the choice of device types and their lengths and widths and the required contact pad size and spacing. For example, for PICs containing MMI couplers, 2x2 MMI couplers are longer than 1x2 MMI couplers, but 2x2 MMI couplers have smaller parasitic back reflections and offer an extra input and/or output waveguide for testing, so 2x2 MMI couplers were used throughout. In the case of directional couplers, their length is dependent on the coupler waveguide widths and spacing. The narrower the waveguides and the gap between them, the shorter the directional coupler can be. The minimum values for the waveguide widths and gap are limited by their waveguiding properties
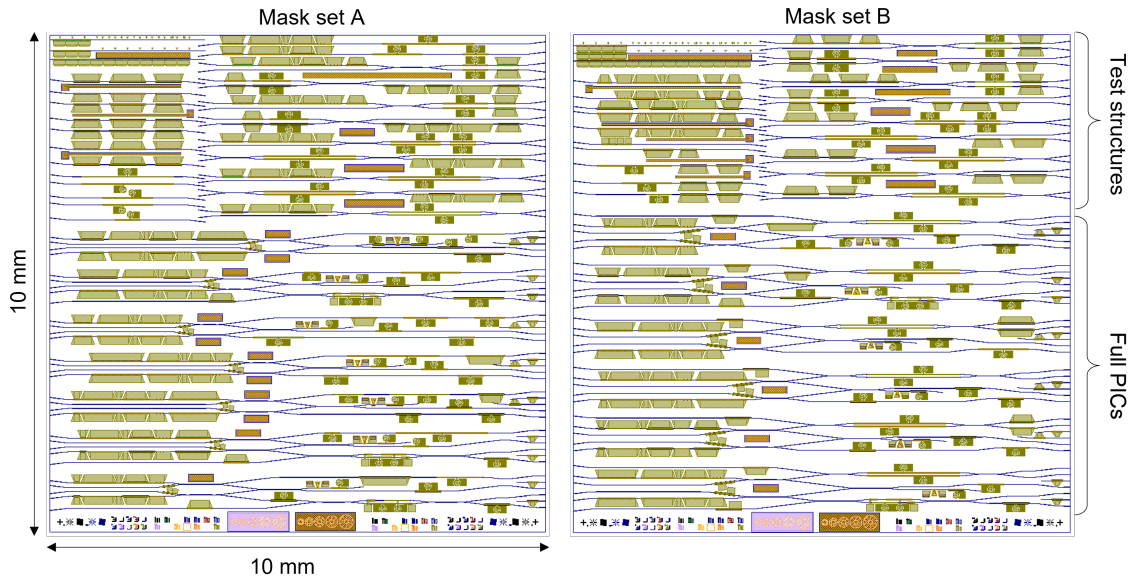
Figure 3.4: The two sets of mask layouts used for the third generation of the QWI fabrication.

and lithographic capabilities. A directional coupler gap of 1 $\mu$m was used to keep the directional couplers short, but this gap was difficult to accurately and reproducibly resolve with the lithographic process that was used.

The total PIC length was minimized by keeping the various arms within the PIC as close together vertically as possible. This is because all of the bends in the PIC were limited to seven degrees to prevent severe undercut of the waveguide during the crystallographic wet etch used to finish the ridge etch. Since the angled waveguides were limited to such a shallow angle, they had to be fairly long to create enough vertical space between different arms of the PIC. To address this, the device contact pads, which are the largest features in the layout, were carefully arranged and packed to keep the PIC width, and therefore length, as small as possible. The device contact pad size and spacing was limited by wirebonding capabilities. The pads need to be large enough and spaced far enough from adjacent pads so

40

that the wire bond ball does not touch the adjacent pad.

Another consideration for the pad arrangement, was to space the pads for ease of wire-bonding to a custom designed carrier. Although most of the devices are operating at DC or at low speeds (e.g. 125 MHz for the phase modulator), it is advantageous to keep the wire bonds relatively short for good wire bonding yield. Thus, pad layout was determined with a carrier design in mind. The pad for the one high-speed device, the 15 GHz bandwidth photodiode, was kept as close to one edge of the PIC as possible to minimize the wire bond length for this device.

In addition to keeping the PIC length as short as possible, an effort was also made to keep the features with critical lithographic dimensions, namely the directional couplers containing a narrow 1 $\mu$m gap between the parallel waveguides, near the center of the lithographic field (die area) where the focus of the lithography tool is best. Therefore, the PICs containing only MMI couplers were placed at the bottom of the field, so that the PICs with directional couplers were placed as close as possible to the center of the field.

Several output waveguide options and extra input and output waveguides were included to facilitate testing and packaging. Only two output waveguides are required for the intended PIC operation - the leader laser side output from the phase modulator and the follower laser side pulse train output - but additional outputs were useful for characterization and testing in the lab. For example, if there is not enough power exiting the leader laser side to send the signal to a fiber splitter before coupling to the reference cell, the output from the backside of the leader laser can be used to monitor the leader laser spectrum to make sure

the laser is locked to 1572.335 nm. In case a certain path in the PIC does not work, other outputs may be able to be used to still demonstrate most of the system operation. For example, if the on-chip photodiode does not have the required bandwidth, the second output of the 2x2 coupler that leads to the photodiode, which is routed to the edge of the PIC, could be used to couple light to an off-chip detector for testing all of the other PIC components.

At the main output PIC facet (on the right in Figure 3.4), there are two options for placement of the facet cleave. The first, farther in from the die edge, was designed for testing in the lab with individually aligned fibers. For this first case, the two main output waveguides were angled in opposite directions to make it easy to access both outputs at the same time. The output waveguides are angled to prevent reflections at the facet from propagating back into the waveguide, but if the two waveguides were angled in the same direction, it would be very hard to physically get two fibers close enough to access both outputs at the same time. The second facet cleave option, at the very right edge of the die, was included for attaching a fiber array. The waveguides at this output are perpendicular to the facet (not angled) and regularly spaced by 127 $\mu$m.

## 3.4   Chapter Summary

In Chapter 3, the architecture, operation, and required specifications of the $CO_2$ lidar system were outlined. The device selection for implementing the lidar in a PIC and considerations for the mask layout were discussed. To meet the requirements set by the lidar system developers at NASA, many PIC variations were included, considering the trade-off for various

component implementations. For example, PICs with directional couplers were expected to suffer from less parasitic back reflections than PICs with MMI couplers, but MMI couplers are much easier to fabricate. Therefore, several PICs with directional couplers and several PICs with MMI couplers were included in the mask layout. SGDBR lasers, while providing a larger wavelength tuning range than needed, were used for both the leader and follower lasers to ensure that the lasers could always be tuned to 1572.335 nm.

# References

[5]  S. Andreou, K. A. Williams, and E. A. J. M. Bente, "Residual amplitude modulation in inp-based integrated phase modulators and its effect in pound-drever-hall frequency stabilization," *OSA Advanced Photonics Congress IPR*, 2017.

[6]  S. Andreou, K. A. Williams, and E. A. J. M. Bente, "Steady-state analysis of the effects of residual amplitude modulation of inp-based integrated phased modulators in pound-drever-hall frequency stabilization," *IEEE Photonics Journal*, vol. 11, no. 3, 2019.

[7]  E. A. Whittaker, M. Gehrtz, and G. C. Bjorklund, "Residual amplitude modulation in laser electro-optic phase modulation," *Journal of the Optical Society of America B*, vol. 2, no. 8, 1985.

# Chapter 4

# Epitaxial Material Design and Device Fabrication

## 4.1 Epitaxial Structure

In this work, quantum well intermixing (QWI) was used for the integration of active and passive photonic integrated circuit (PIC) regions. The epitaxial structure used seven quantum wells centered in a 1.24Q waveguide. The multi-quantum well (MQW) stack was designed to have a photoluminescence (PL) emission at 1565 nm, to account for emission red-shift with heating during laser operation. Only one intermixing anneal was performed, resulting in the passive and modulator regions having the same band edge. One of the reasons a QWI platform was chosen is that it readily accommodates the integration of distributed feedback (DFB) lasers, which make sense for the leader laser in the lidar PIC layout. Additionally, QWI

results in very low loss transitions between the active, and passive and modulator regions. This is important for such a large PIC that is sensitive to feedback from reflections. Finally, an unintentionally doped (UID) indium phosphide (InP) cap is required for the QWI process and this cap is kept in the passive regions to increase the p-doping setback and therefore reduce passive losses. An offset quantum well (OQW) platform was explored in parallel and, while not the focus of this dissertation, will be touched upon in Chapter 7.

## 4.2   Fabrication Process

### 4.2.1   Process Flow Summary

A summary of the fabrication steps is shown in Figure 4.1. The starting epitaxial structure (0) consists of a seven MQW stack centered in a 1.24Q waveguide. A UID InP cap layer above the waveguide captures implanted vacancies during the QWI implant with phosphorous ions (1). The active regions are masked during the implant to prevent intermixing from occurring there. After the implant, the sample is annealed at 675 °C to drive the implanted vacancies into the MQW layers and induce compositional intermixing between the quantum wells and barriers (2). The anneal time determines the amount of band edge shift. The sample is encapsulated in thin $Si_3N_4$ for the anneal to prevent indium desorption. Next, the UID cap layer is etched away everywhere except in the passive regions (3). The UID cap acts as an extra p-dopant setback layer in the purely passive regions [1]. After the cap etch, the laser mirror gratings are patterned using electron-beam lithography (EBL) and etched into the

top 1.24Q waveguide layer (4). Next, a p-side regrowth is performed (5) and the waveguide ridge is etched (6). To aid in reducing parasitic capacitance in the high-speed photodiode regions, a so-called "passivation" etch is performed (7). The high-speed passivation etch entails etching into the 1.24Q waveguide layer on either side of the ridge to remove any p-dopants that diffused into the waveguide layer during the regrowth. Next, to electrically isolate adjacent components, the top InGaAs contact layer is etched away between device sections (8). For easy screening of devices before thinning and carrier mounting, top side n-contacts are formed by etching down to the substrate and depositing metal (9). Finally, vias are etched to expose the InGaAs p-side contact layer and probe metal is deposited (10).

# 0. Epitaxial Material

UID InP
1.24 Q InGaAsP
MQW
1.24 Q InGaAsP
n-InP

# 1. QWI: P⁺ Implant

Hard mask

# 2. QWI: Intermixing Anneal

# 3. Undoped Cap Etch

# 4. Grating Etch
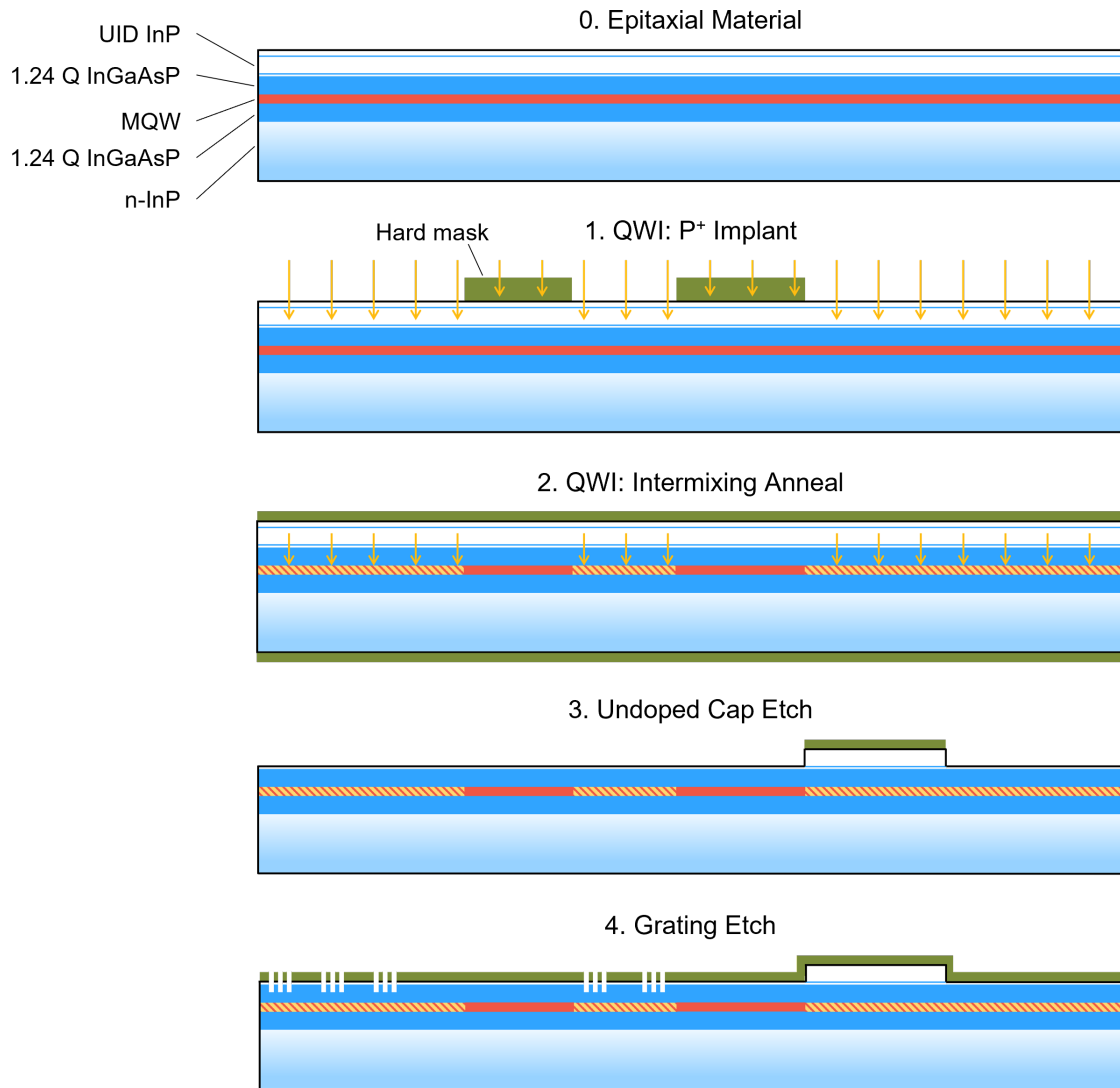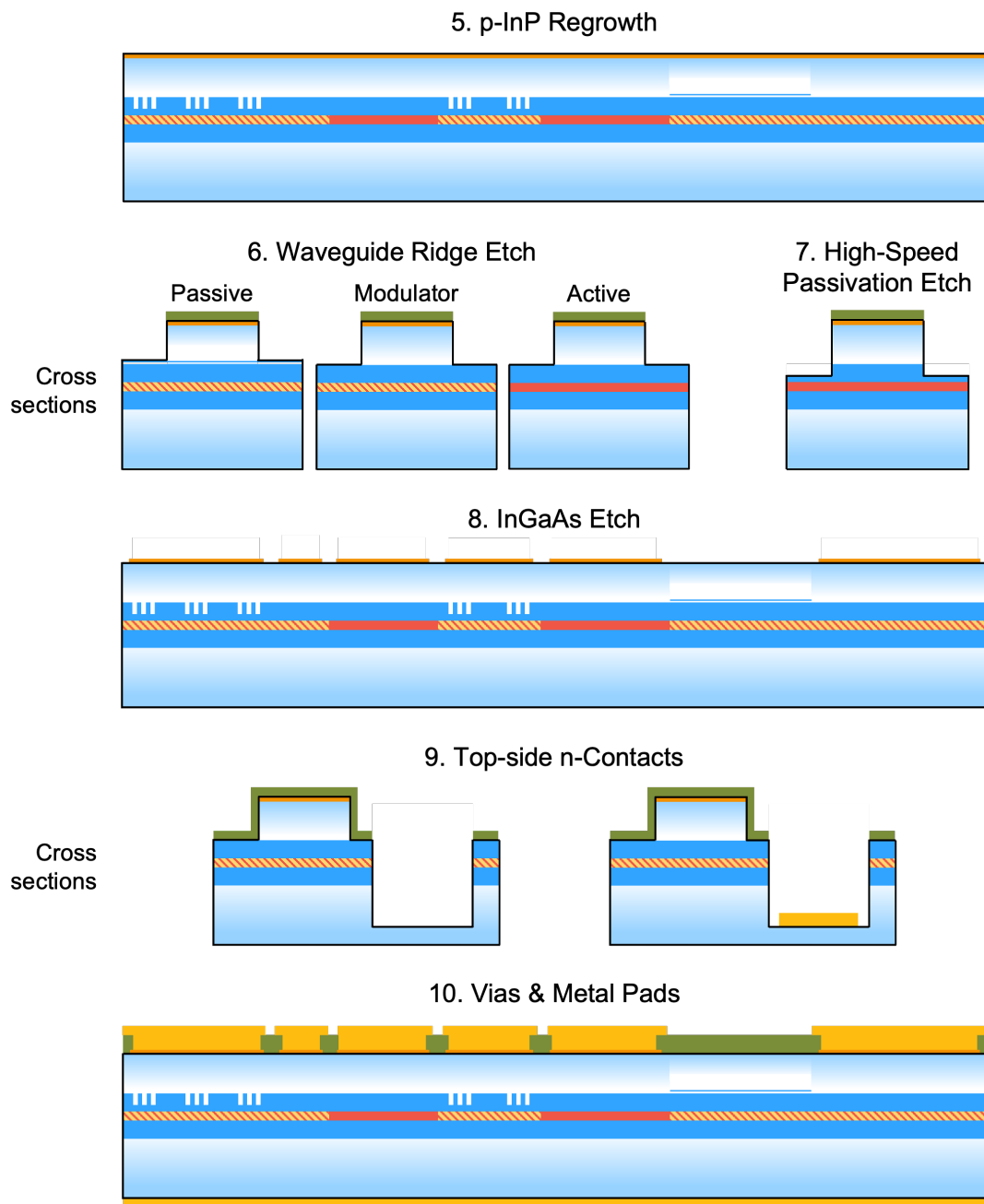
Figure 4.1: Fabrication steps for the QWI PIC platform process.

## 4.2.2 Active/Passive Definition

Figure 4.2(a) shows an optical micrograph of a sample with patterned $Si_3N_4$ ready for the $P^+$ QWI implant. The samples were implanted with phosphorous ions at a dose of 5e14 $cm^2$, with an energy of 100 keV, at a temperature of 200 °C and with a 7° tilt. The regions protected by $Si_3N_4$ (dark green) will become active regions. Figure 4.2(b) shows an optical micrograph of a sample after $P^+$ implant and $Si_3N_4$ removal. Even though the hard mask has been removed, there is contrast between the implanted and protected regions due to implant induced damage to the crystal lattice. This is also observed as a step height of 5 nm from the implanted to protected regions. The color contrast was observable with the naked eye as illustrated in Fig. 4.2(c).



(a)                                       (b)                                       (c)
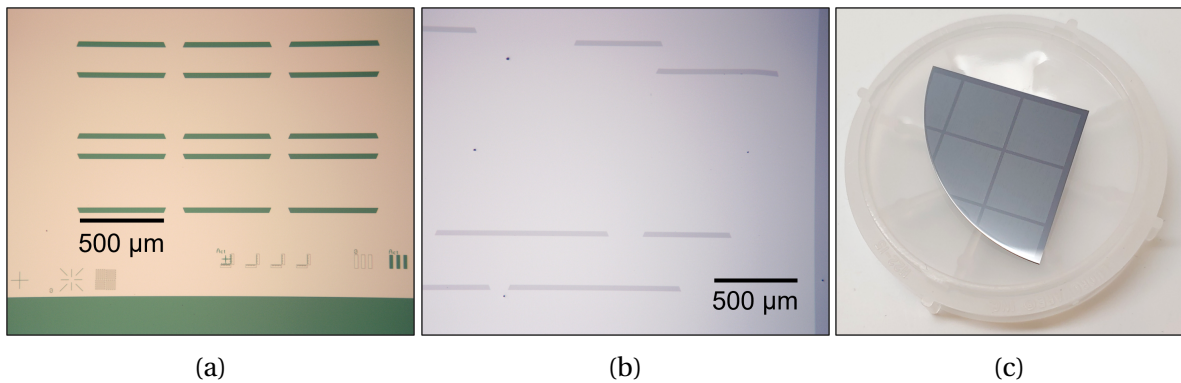
Figure 4.2: (a) Optical micrograph of patterned $Si_3N_4$ hard mask before $P^+$ implantation. The masked (green) areas will become gain (active) regions. (b) Optical micrograph of a sample after $P^+$ implantation and hard mask removal. (c) Photo of a 2-inch quarter after $P^+$ implantation and hard mask removal.

To prevent the desorption of indium during the QWI anneal, each sample was coated with 40 nm of $Si_3N_4$ on the top and bottom. It is very important that there be no particles under the $Si_3N_4$ film and no holes or scratches in the film. Therefore, careful cleaning and

handling procedures are required for the encapsulation step. The $Si_3N_4$ is deposited on the top side of the sample first, using plasma enhanced chemical vapor deposition (PECVD). The deposition is performed in two layers. After the first layer, the sample was cooled and its placement rotated, to minimize the formation of pinholes through both $Si_3N_4$ layers. Depositing $Si_3N_4$ on the top surface first gives some protection for when the sample is flipped over for the backside deposition. Figure 4.3(a) shows how the sample is loaded face down in the tool for the backside deposition. A clean Si carrier wafer is used to prevent the top surface from being scratched. The sample is surrounded by Si pieces to prevent the sample from sliding during tool vaccum and venting, which may cause scratches. Figure 4.3(b) shows an example of a scratch in the top $Si_3N_4$. Depending on where a scratch or particle lands, it could create problems for a PIC during the QWI anneal. A scratch such as that shown in Fig. 4.3(b) did not look significantly different after the anneal and did not result in any film cracking during the anneal.



(a)   (b)
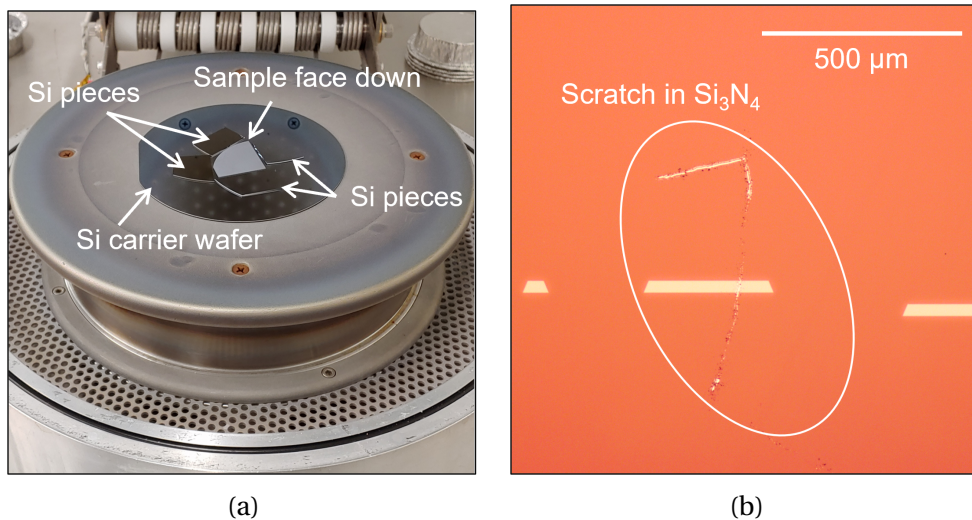
Figure 4.3: (a) Loading for backside deposition to minimize scratches. (b) Example of a scratch in the top side $Si_3N_4$ encapsulation hard mask.

A rapid thermal processor manufactured by AET was used for the QWI anneal. As shown in Figure 4.4, the sample sits on a Si carrier wafer and a thermocouple (TC) contacts the carrier wafer near the sample. For repeatability, each InP sample was positioned in roughly the same location relative to the TC head on the carrier wafer.



(a)                          (b)
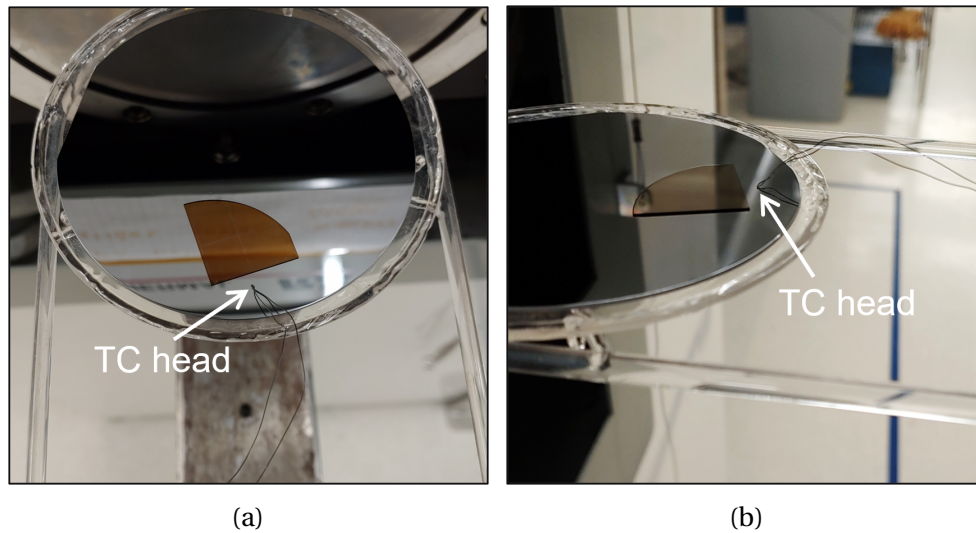
Figure 4.4: Position of the sample relative to the thermocouple in the RTA. (a) Top view and (b) oblique view.

Figure 4.5 plots the room temperature photoluminesence (PL) spectrum of QWI calibration samples for various anneal times from 30 to 120 seconds. As the anneal time increases, the peak PL wavelength blue shifts further and further. From 30 seconds to about 70 seconds, the PL intensity increases due to implant induced crystal damage being annealed out. Implanted samples that have not been annealed do not have a discernable PL peak. The dotted line in Figure 4.5 shows the PL spectrum for a sample that was annealed for 120 seconds, but was not implanted. The peak PL wavelength of the non-implanted, annealed sample closely matches that of the sample that was not implanted or annealed, as

expected. The notch in intensity around 1400 nm is inherent to the PL measurement setup used to capture the PL spectrum and is not a real feature of the material.
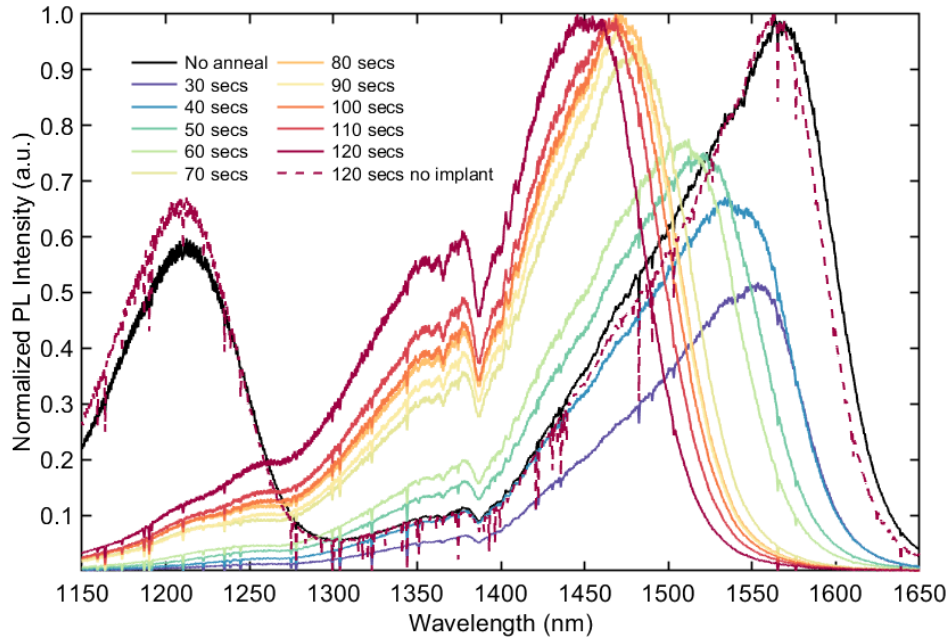


Figure 4.5: Photoluminescence spectra of QWI calibration samples annealed at 675° C from 30 to 120 seconds. Notch around 1390 nm is from the PL setup and may be due to water condensation in the system.

Figure 4.6(a) plots the amount of peak PL wavelength shift with anneal time for the calibration samples. Figure 4.6(b) shows the same plot, but for the 2-inch wafer quarter samples. Some of the samples were annealed multiple times to achieve the desired band edge shift and the points plotted in Figure 4.6 are for the first anneal performed on each sample. Table 4.1 shows the anneal times and wavelength shifts for four different samples with the same epitaxial structure. The peak PL wavelength is an average of multiple points across the sample, labelled in Figure 4.7. As can be seen from Table 4.1, a peak PL wavelength blue-shift of 10-20 nm was observed in the active regions of the samples where a shift in the

MQW band edge was undesired. This varied quite a bit between samples and may be due to defects in the base epitaxial material or uneven stress in the $Si_3N_4$ encapsulation layers. For all four samples, the average detuning of the passive/modulator band edge from the operating wavelength of 1572 nm was 109 nm. Figure 4.8 shows the typical final active and passive/modulator PL spectra for a 2-inch wafer quarter.
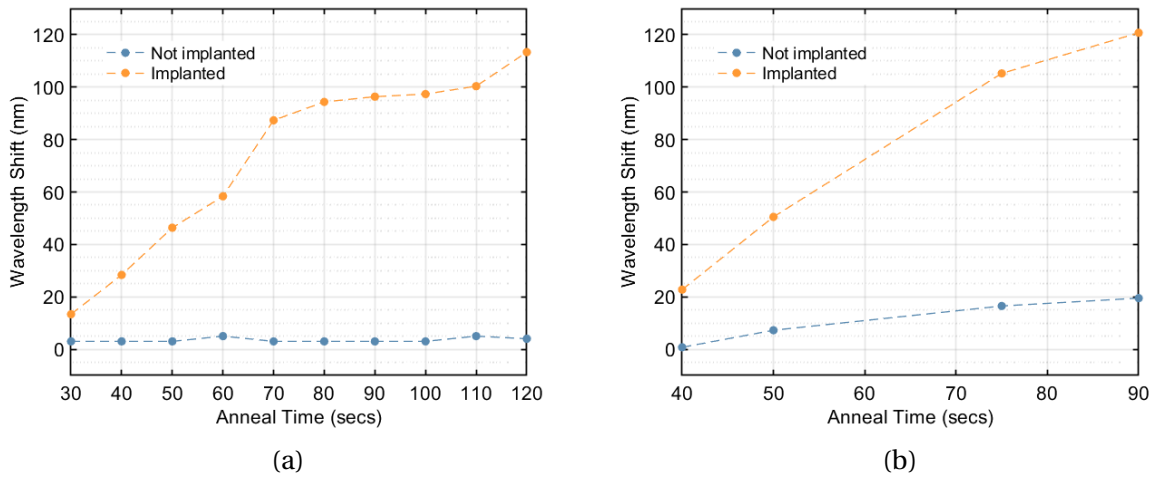


Figure 4.6: Peak PL wavelength shift with anneal time for (a) calibration samples and (b) patterned 2" wafer quarter samples.

| Sample | Anneal time (s) | Avg. $\lambda$ before annealing (nm) | Avg. active $\lambda$ (nm) | Avg. passive $\lambda$ (nm) |
|---|---|---|---|---|
| 1 | 40 + 30 + 30 + 40 | 1564 | 1553 | 1472 |
| 2 | 75 | 1570 | 1553 | 1464 |
| 3 | 90 | 1566 | 1547 | 1446 |
| 4 | 50 + 30 + 40 | 1567 | 1558 | 1471 |

Table 4.1: Anneal times and peak PL wavelengths before and after annealing for each fabricated sample.
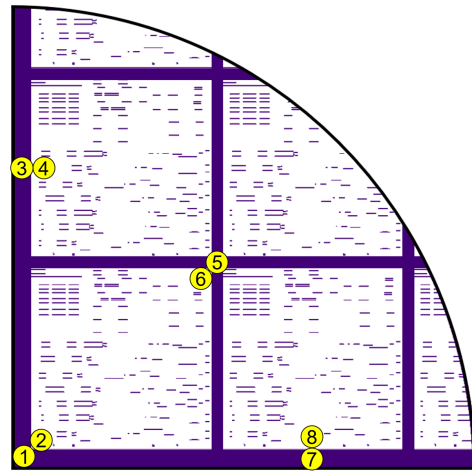
Figure 4.7: Locations used for PL measurements on patterned 2-inch wafer quarters. Points 1, 3, 5, and 7 are in the active region and points 2, 4, 6, and 8 are in the intermixed passive region.
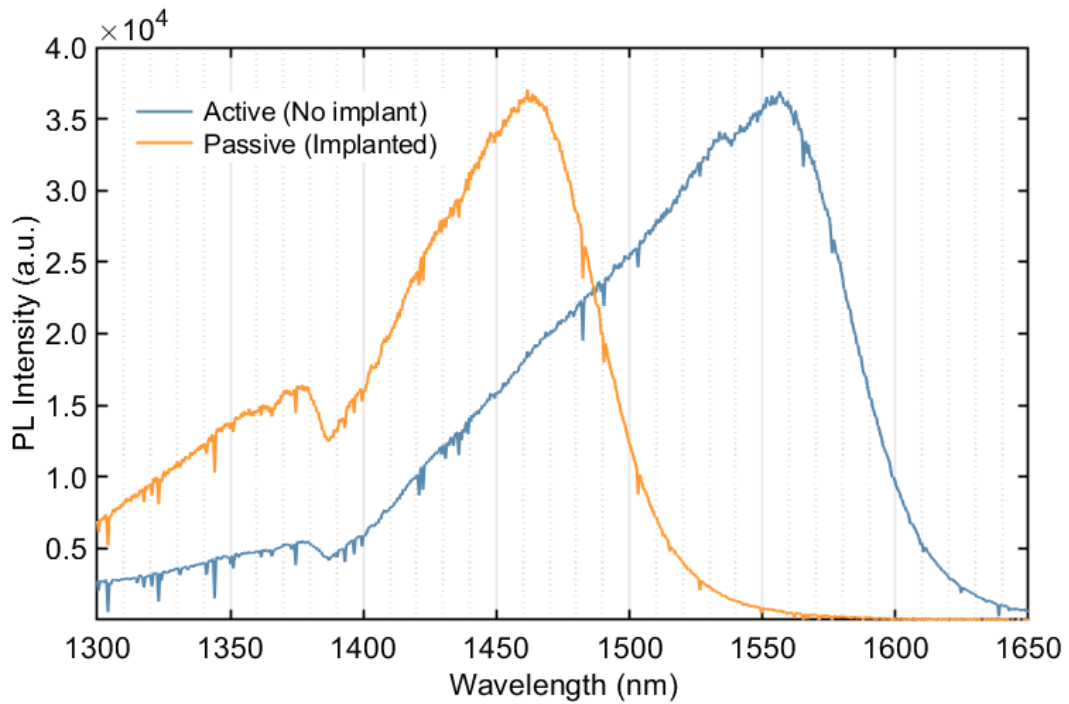


Figure 4.8: Typical photoluminescence spectra for the active (not implanted) and passive (implanted) regions of the samples.

54

### 4.2.3 Unintentionally Doped Passive Cap

After the QWI anneal, the sample is patterned for the selective removal of the UID InP cap layer. The cap layer is removed using a timed wet etch. Figure 4.9 shows optical microscope images of the patterned cap layer.
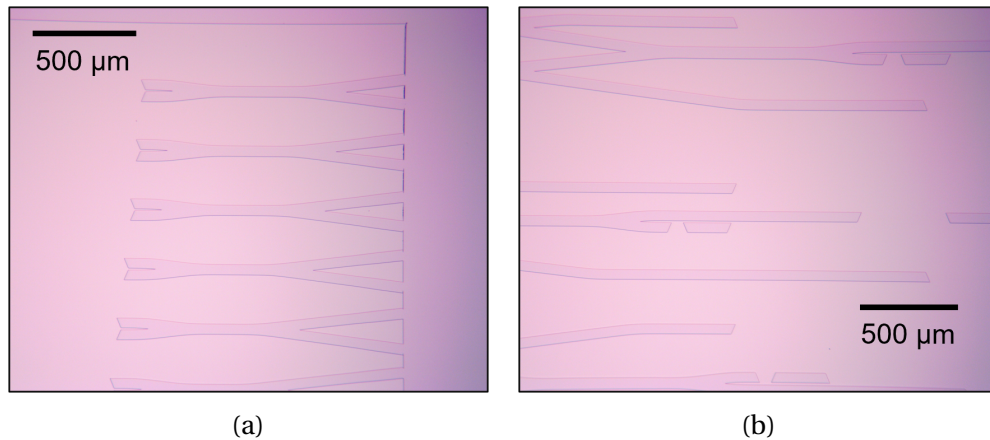


Figure 4.9: Optical micrographs showing examples of the UID InP cap in the passive waveguide regions.

### 4.2.4 Grating Formation

Following the UID InP cap layer etch, the gratings that will form the laser mirrors are patterned using electron beam lithography. An $SiO_2$ hard mask is etched using an inductively coupled plasma (ICP) etch and the etch into the quaternary waveguide layer is performed using reactive ion etching (RIE) with a methane/hydrogen/argon chemistry. Figure 4.10 shows scanning electron and atomic force microscope images of an etched grating.

(a)                                                    (b)
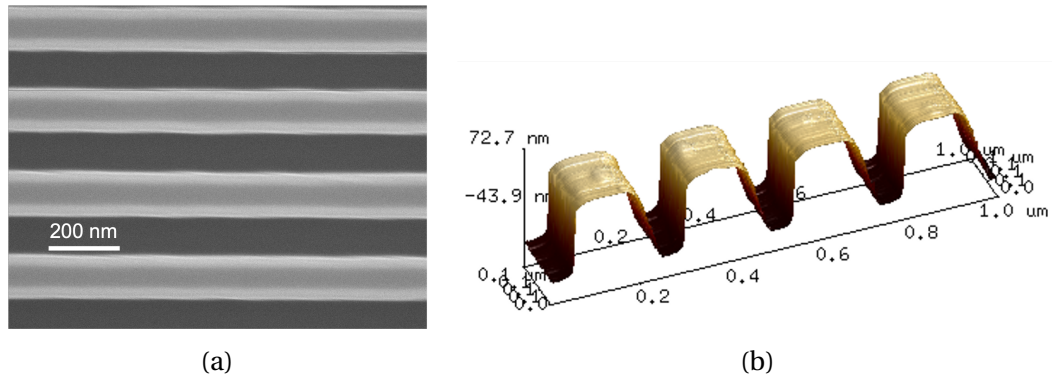
Figure 4.10: (a) Scanning electron micrograph of etched grating. (b) Atomic force microscope scan of etched grating.

### 4.2.5 P-Side Regrowth

After the grating etch, the samples are prepared for the p-side MOCVD regrowth. An important factor for the regrowth is filling in and planarizing over the etched gratings. Figure 4.11 shows an example of a quality regrowth where the surface is planar over the grating regions. The pattern in the image is from the UID InP cap layer, which has about a 400 nm step height.
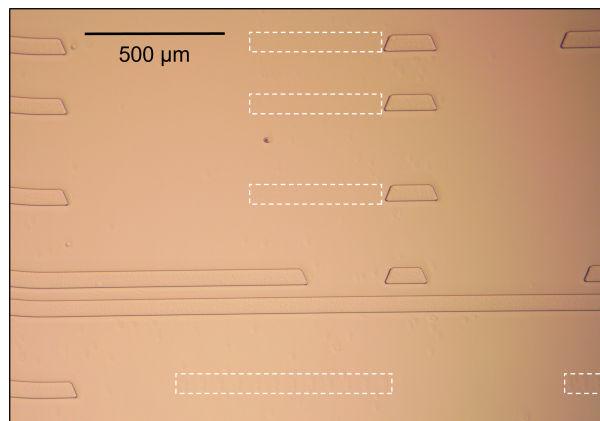


Figure 4.11: Optical micrograph of sample surface after p-side regrowth demonstrating planarization over the etched gratings (outlined by white dashed boxes).

### 4.2.6 Waveguide Ridge Etch

After the regrowth, the waveguide ridge etch is performed. The ridge is first dry etched using an ICP etch at 200 °C and a $Cl_2/H_2/Ar$ chemistry. After dry etching the ridge most of the way, the ridge etch is completed with a 3:1 $H_3PO_4$:HCl wet etch that stops on the top 1.24Q waveguide layer. The wet etch creates atomically smooth ridge sidewalls so that no scattering loss is added to the waveguide mode. Figure 4.12(a) shows a scanning electron microscope (SEM) image of a waveguide ridge cross section after the dry etch. A thick $SiO_2$ hard mask is seen on top of the ridge. Figure 4.12(b) is an SEM image of two parallel waveguide ridges after the dry etch. Figure 4.13(a)-(c) show top-down SEM images of an MMI coupler at a few magnification settings. Similarly, Figure 4.13(d)-(f) show top-down images of a directional coupler. Figure 4.14 shows an optical micrograph of the sample after the waveguide ridge dry and wet etches.



|        (a)        |        (b)        |
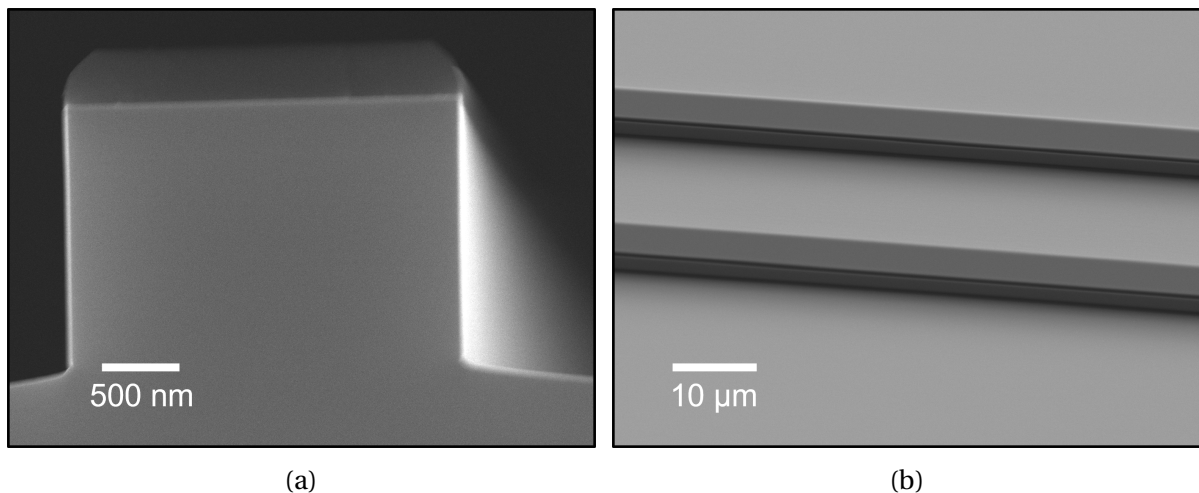
Figure 4.12: SEM image of (a) a cross-section of a waveguide ridge and (b) an oblique view of two waveguide ridges following the dry etch.

(a)  (b)  (c)

(d)  (e)  (f)
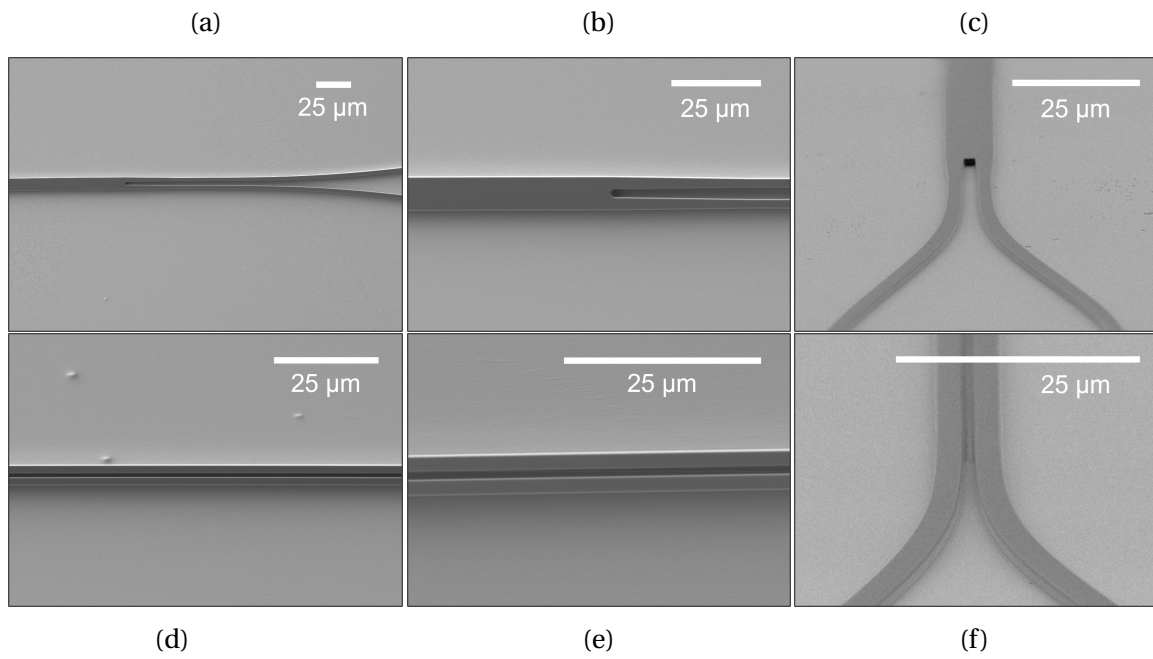
Figure 4.13: SEM images of the etched waveguide ridge for a multimode interference (MMI) coupler (a)-(c) and a directional coupler (d)-(f)
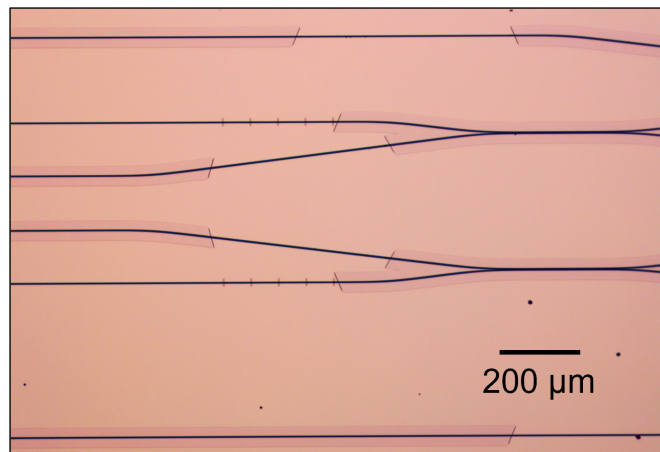


Figure 4.14: Optical micrograph showing waveguides after the dry and wet ridge etching.

### 4.2.7 Back End Steps

**High-Speed Passivation Etch**

Figure 4.15 shows (a) the patterned photoresist mask used for the high-speed passivation etch and (b) the photodiode region after the passivation etch and subsequent hard mask deposition. By etching about 80 nm into the top 1.24Q waveguide layer where the photodiode probe metal will be deposited, the idea is that p-dopants that diffused into the top waveguide layer during the regrowth are removed, thus reducing the parasitic capacitance for the high-speed photodiode.
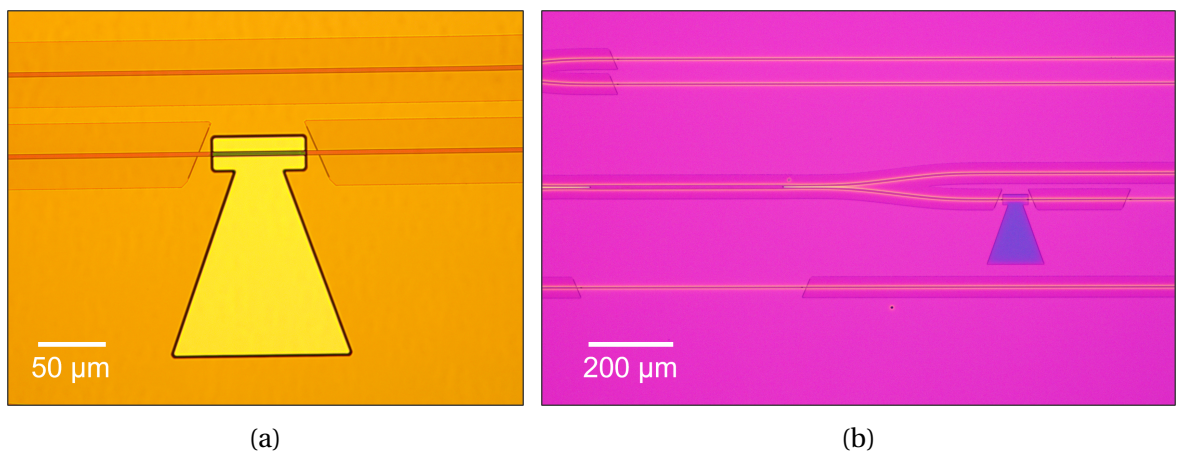


Figure 4.15: (a) Optical micrograph showing high-speed passivation lithography pattern. (b) Optical micrograph showing etched high-speed passivation pattern. Hard mask deposited on the surface provides contrast between the etched high-speed passivation and surrounding area.

**Electrical Isolation Etch**

Following the high-speed passivation etch, a wet etch of the InGaAs contact layer between device sections was performed to electrically isolate adjacent sections. To align the photore-

sist mask to the top of the ridge, a semi-self aligned process was used. In this process, large squares are patterned around the regions where the InGaAs will be removed, but these regions are only partially exposed and developed such that the photoresist is thinned but not developed away entirely. The top of the ridge is revealed by a series of $O_2$ plasma dry etches and inspections to determine when to stop the etching. Because the resist is thinner on top of the ridge than surrounding it, the top of the ridge is revealed first. Figure 4.16(a) shows an optical micrograph of the electrical isolation regions partway through the resist etch. The green dashed circle shows a region where the top of the ridge has not yet been revealed and the blue dashed circle shows a region where the top of the ridge is visible, distinguishable by its bright color due to the hard mask on top of the ridge. Figure 4.16(b) shows a couple of optical micrographs of several locations where the top of the ridge covered with hard mask has been revealed after etching away the photoresist. The image in Figure 4.16(c) shows the electrical isolation regions after the hard mask on the top of the ridge has been etched away. After etching the hard mask, a 3:1 $H_3PO_4$:HCl wet etch is used to remove an InP cap and then a 3:1:50 $H_3PO_4$:$H_2O_2$:$H_2O$ is used to remove the highly doped InGaAs contact layer to improve the electrical isolation between adjacent devices.

**Top-Side N-Contact Formation**

After the electrical isolation etch, top side n-contacts are formed. In the first step, trenches are etched down to the highly n-doped substrate using a $CH_4$/$H_2$/Ar reactive ion etch (RIE) as shown in Figure 4.17(a). Once the trenches are created, the n-contact metal stack consisting of Ni/AuGe/Ni/Au is deposited using electron-beam evaporation. Figure 4.17(b) shows
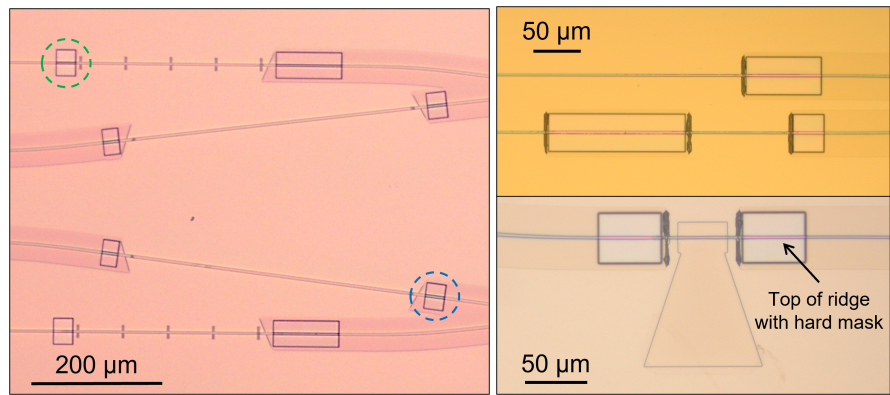
(a)



(b)
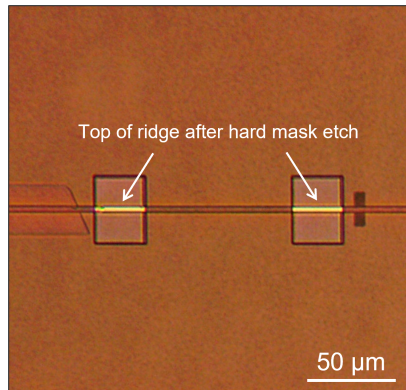


(c)

Figure 4.16: (a) Optical microscope image showing in progress etch of the photoresist in the semi-self aligned process. The color of the top of the ridge inside the green and blue dashed circles differs because the thickness of the photoresist is different in each region. (b) Optical micrograph showing regions where the top of the ridge has been exposed after etching away the photoresist. The top of the ridge appears pink because of the hard mask covering it. (c) Top of the ridge after the hard mask has been dry etched.

the sample after metal deposition and liftoff, leaving the contact metal only in the trenches. To form the final low resistance contact, the sample is annealed at 430 °C for 30 seconds. The anneal causes the metal to change color and become rough in appearance as an alloy is formed, which can be seen in Figure 4.17(c) compared to Figure 4.17(b). Next, a $Si_3N_4$ hard mask is deposited everywhere and vias are etched over the n-metal and on top of the ridges for the p-contact.



|   (a)   |   (b)   |   (c)   |
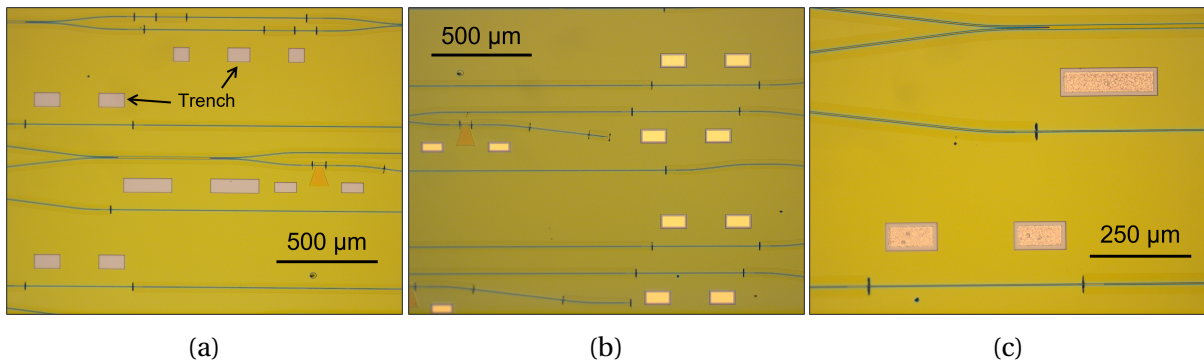
Figure 4.17: (a) Optical micrograph showing trenches etched for top-side n-contacts. (b) Top-side n-contacts immediately after metal deposition and (c) after anneal.

**Via Etch**

The alignment of the via layer within the top of the 3 $\mu$m wide ridge is a critical step. Figure 4.18(a) and (b) shows examples of the via opened on top of the waveguide ridge. After the hard mask has been etched away in the vias, a 3:1 $H_3PO_4$:HCl wet etch is performed to remove the InP protective cap layer and reveal the InGaAs p-contact layer. In Figure 4.18(a), an area where the InGaAs contact layer was removed during the electrical isolation step can be seen between two p-side vias. The edge on either side of the via in 4.18(b) is also due to the previous removal of the InGaAs layer between devices.
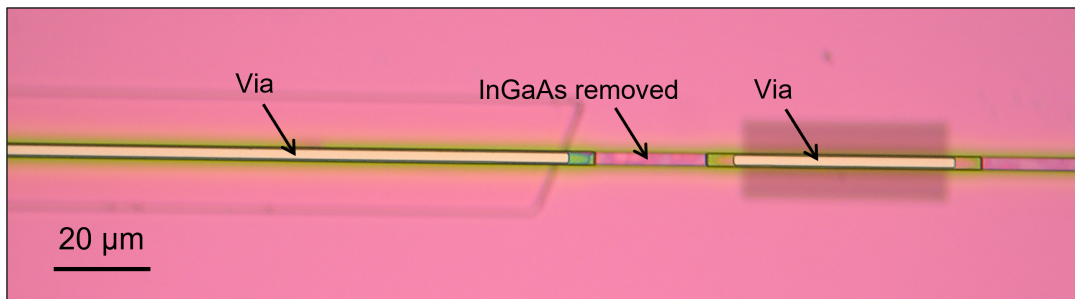
(a)
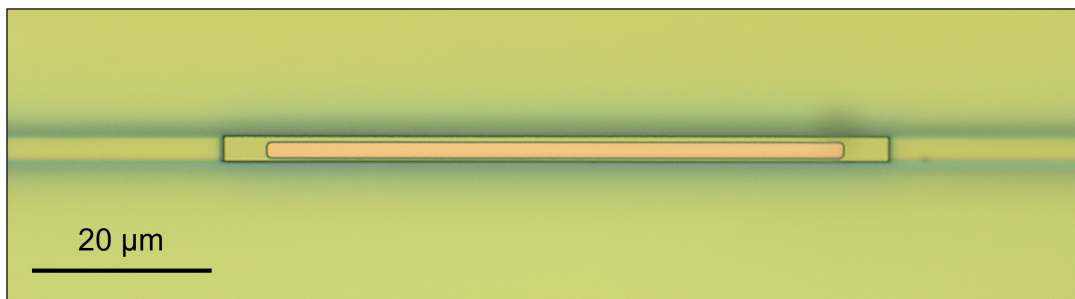


(b)

Figure 4.18: Optical micrographs showing etched p-side vias.

**P-Metal Deposition**

After the n- and p-vias are opened, the contact pad layer pattern is defined with lithogra-phy, the pad metal is deposited everywhere and the excess metal is lifted off. The pad metal stack consists of Ti/Pt/Au/Ti/Au. Liftoff is achieved by soaking the sample in the photore-sist stripper NMP (1-Methyl-2-pyrrolidon) at 80 °C. The photo in Figure 4.19(a) shows the sample and excess metal film that has been removed immediately after liftoff. The optical micrograph in Figure 4.19 (b) shows a close-up view of the metal pads. Following liftoff, the sample is annealed at 390 °C for at least 30 seconds. Composite photos of the die for each of the two layouts used in the last fabrication generation are shown in Figure 4.20.

(a)                                                    (b)
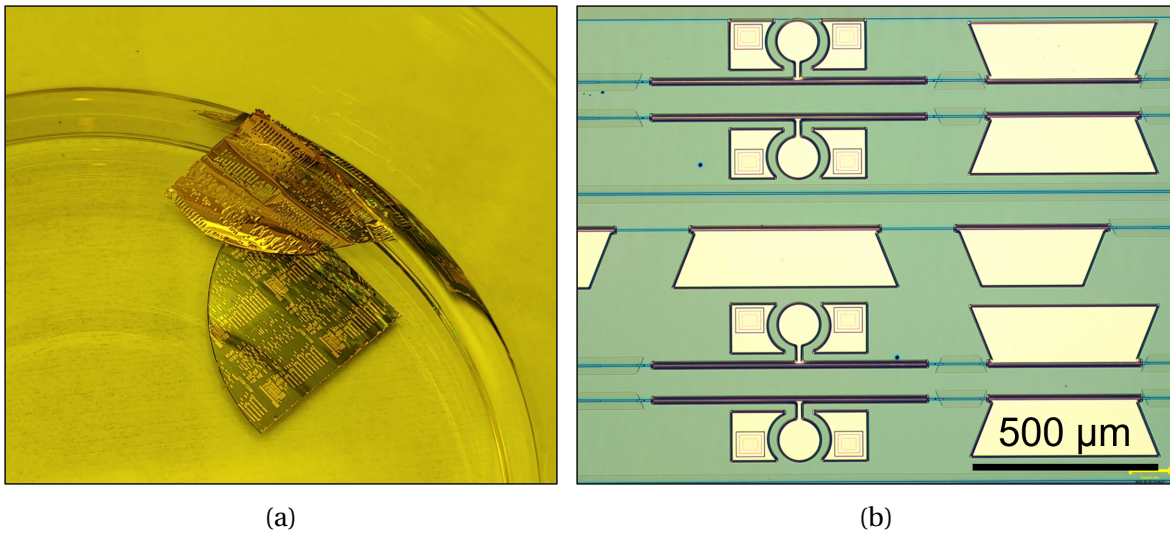
Figure 4.19: (a) Photo of sample in NMP immediately following metal liftoff. (b) Optical micrograph showing metal pads.

**Preparation for Testing**

After contact annealing, on-chip testing of the diodes is performed to ensure that good contacts were formed. After the diode performance was verified, each sample was thinned by mechanical lapping to about 150 $\mu$m thick, backside n-contact metal was deposited, and the samples were cleaved into bars. Figure 4.21 (a) and (b) shows a quarter of a 2-inch wafer sample before lapping and cleaving. After cleaving into bars, an anti-reflective coating is deposited on the facets and the bars are further cleaved into single PICs. Each PIC is solder mounted on a custom designed aluminum nitride (AlN) carrier with RF and DC transmission lines. Wire bonding is used to connect the device pads on the PIC to the carrier transmission lines, as shown in Figure 4.22.

<center>(a)</center> <center>(b)</center>
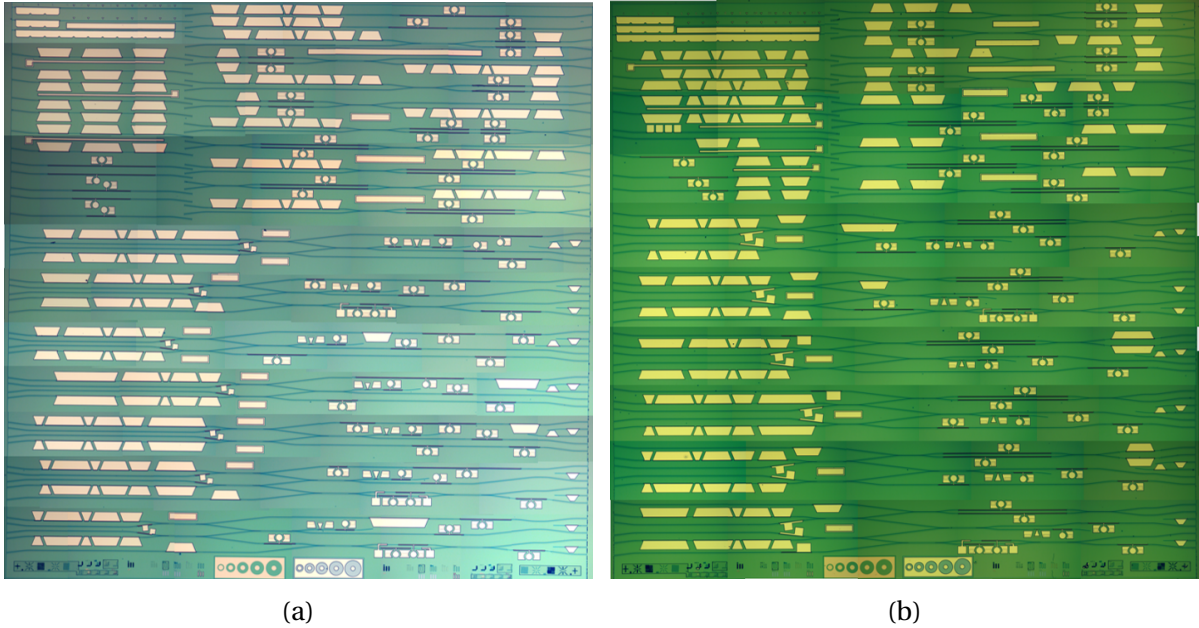
Figure 4.20: Composite optical micrographs of the two layouts fabricated in generation three.

## 4.3 Chapter Summary

Chapter 4 reviewed the epitaxial material platform and the fabrication process for producing the photonic integrated circuit characterized in this work. The PIC employed a quantum well intermixing method to define the active, modulator, and passive regions. The modulator and passive regions used the same intermixed quantum well band edge, but the passive regions retained the unintentionally doped InP cap after the QWI process. The retention of the cap layer reduced the optical loss in the passive regions by creating an extra doping setback on the p-side.

<div align="center">(a)　　　　　　　　　　　(b)</div>
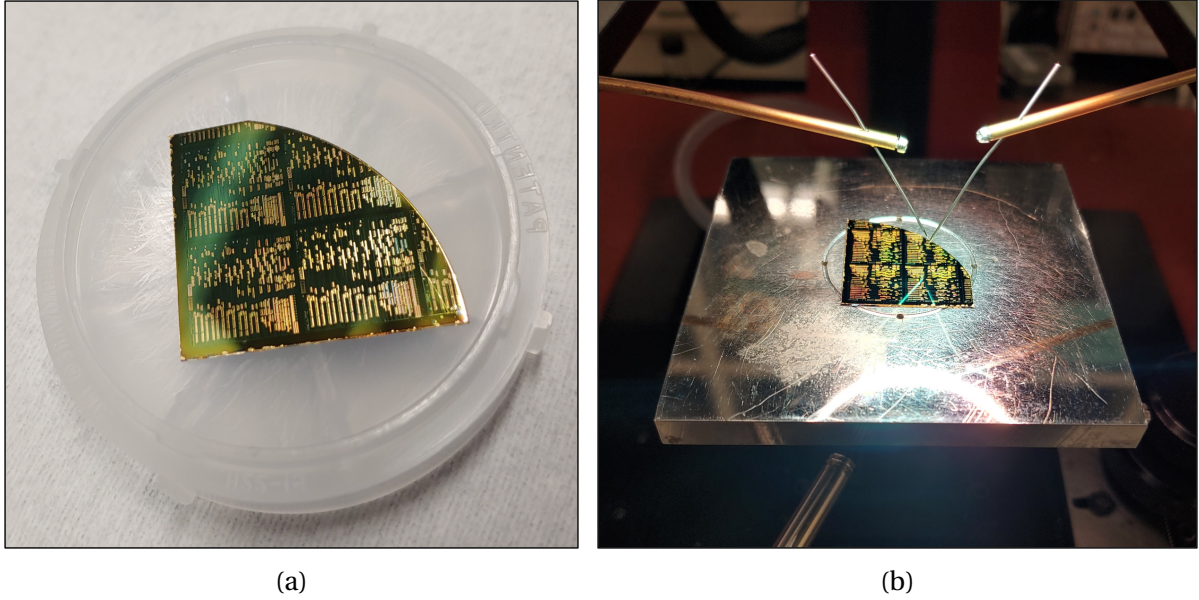
Figure 4.21: (a)-(b) Photos of 2-inch wafer quarter sample after metal deposition. (b) Top-side characterization of diodes before thinning and cleaving.



<div align="center">(a)　　　　　　　　　(b)　　　　　　　　(c)</div>
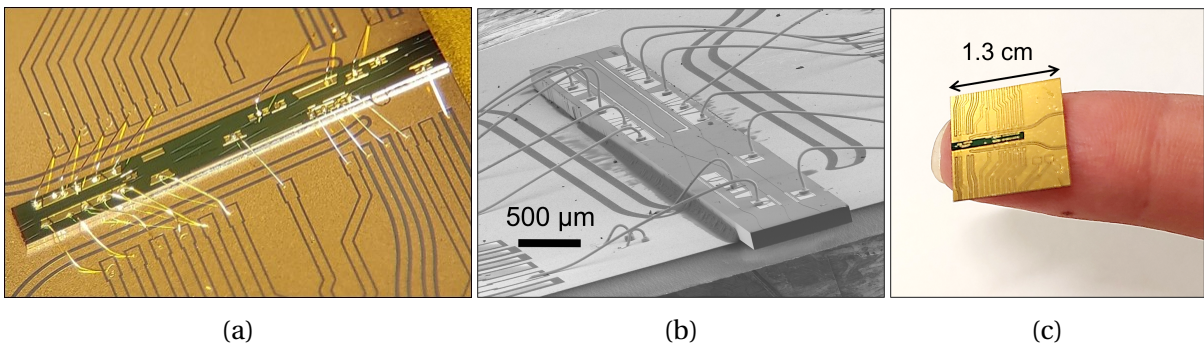
Figure 4.22: (a) Close-up photo of a PIC mounted and wire-bonded to a carrier. (b) Scanning electron microscope (SEM) image of a mounted PIC. (c) Wider view photo of PIC on a carrier, showing the size of the PIC and carrier relative to my finger.

# References

[1] S. C. Nicholes, M. L. Masanovi, J. Barton, E. J. Norberg, E. Lively, B. Jevremovic, L. A. Coldren, and D. J. Blumenthal, "Novel application of quantum well intermixing implant buffer layer to enable high-density photonic integrated circuits in inp," *IEEE International Conference on Indium Phosphide and Related Materials*, 2009.

# Chapter 5

# Laser Design and Performance

## 5.1  Sampled Grating Distributed Bragg Reflector Lasers

The mirrors in a distributed Bragg reflector (DBR) laser are created by selective etching to form a periodic grating that overlaps with the optical mode. In a sampled grating distributed Bragg reflector (SGDBR) laser, a sampling function is applied to the continuous grating resulting in regularly spaced grating bursts as shown in Figure 5.1. Each sampled mirror has a comb response in the frequency domain with an envelope width inversely proportional to the grating burst length. The channel frequency spacing is inversely proportional to the sampling period. The FWHM of each channel is inversely proportional to the mirror effective length. An example sampled grating response for both a rear and front laser mirror are plotted in Figure 5.2(b), the design of which is discussed in the next section. By tuning the rear and front mirrors independently, the user can select which channels of the two mirrors overlap and therefore result in the highest reflectivity supermode. This Vernier tuning

mechanism enables SGDBR lasers to have a wide tuning range, typically 40 nm, while maintaining a high side mode suppression ratio (SMSR) of at least 40 dB. If continuous tuning is desired across the entire tuning range, the channel spacing must not be greater than the achievable phase shift due to current injection [1].
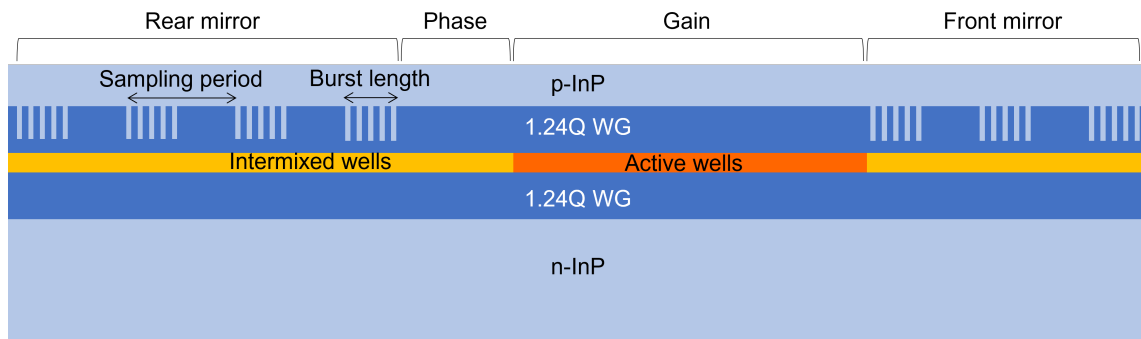


Figure 5.1: Diagram of SGDBR laser structure.

## 5.1.1   First Generation

Figure 5.2(a) gives the design parameters of the first generation SGDBR lasers. Figure 5.2(b) shows the simulated response of the rear and front mirrors. Mirror designs were initially optimized for a center wavelength of 1572.335 nm, but after the fabrication had started, the grating pitch had to be adjusted to meet the requirements of the electron-beam lithography (EBL) tool. The parameters and simulation in Figure 5.2 are shown for the values that were actually fabricated.

Figure 5.3 shows the performance of the first generation SGDBR laser design. Figure 5.3(a) shows the light-current-voltage curve of the laser. The output laser power was measured by a reverse-biased SOA immediately following the laser. The responsivity of the SOA

was assumed to be 1 A/W. The threshold current is reasonable, but not excellent, at 30 mA, and the maximum power output of 6 mW at a 200 mA gain current is far less than the expected 20 mW or so. The jump in power at about 100 mA is due to a longitudinal mode hop. In Figure 5.3(b), overlaid laser spectra show the tuning range and SMSR at each supermode. Although the mirror simulation was centered at 1600 nm, some of the fabricated lasers came out centered near 1570 nm. Figure 5.3(c) shows the laser spectrum when it is tuned to 1572.335 nm. Although the first generation lasers were able to reach the target wavelength, the SMSR at 1572.335 was only 30 dB, which does not reach the target for the lidar system and is less than expected for this laser design.

| Etch depth (nm) | 80 |
| Grating period (nm) | 248 |
| Grating gap width (µm) | 0 |
| Rear/front mirror sampling period (µm) | 61.4/69.6 |
| Rear/front burst length (µm) | 6/4 |
| Rear/front number of bursts | 12/5 |

(a)
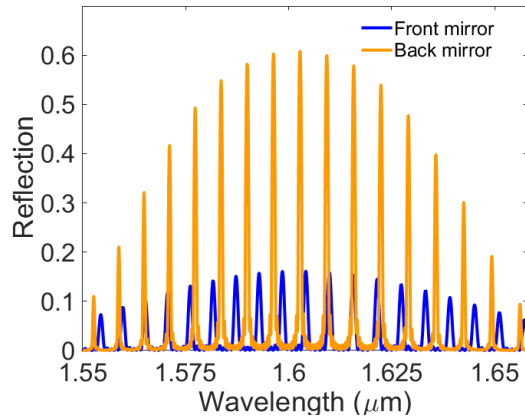


(b)

Figure 5.2: (a) Design parameters for the first generation SGDBR lasers. (b) Simulated front and rear mirror spectral response for the first generation SGDBR laser design [2].

## 5.1.2 Second Generation

The table in Figure 5.4 gives the design parameters for the second generation SGDBR lasers. Figure 5.5 shows the simulated mirror responses for each design. Design A is similar to the

70
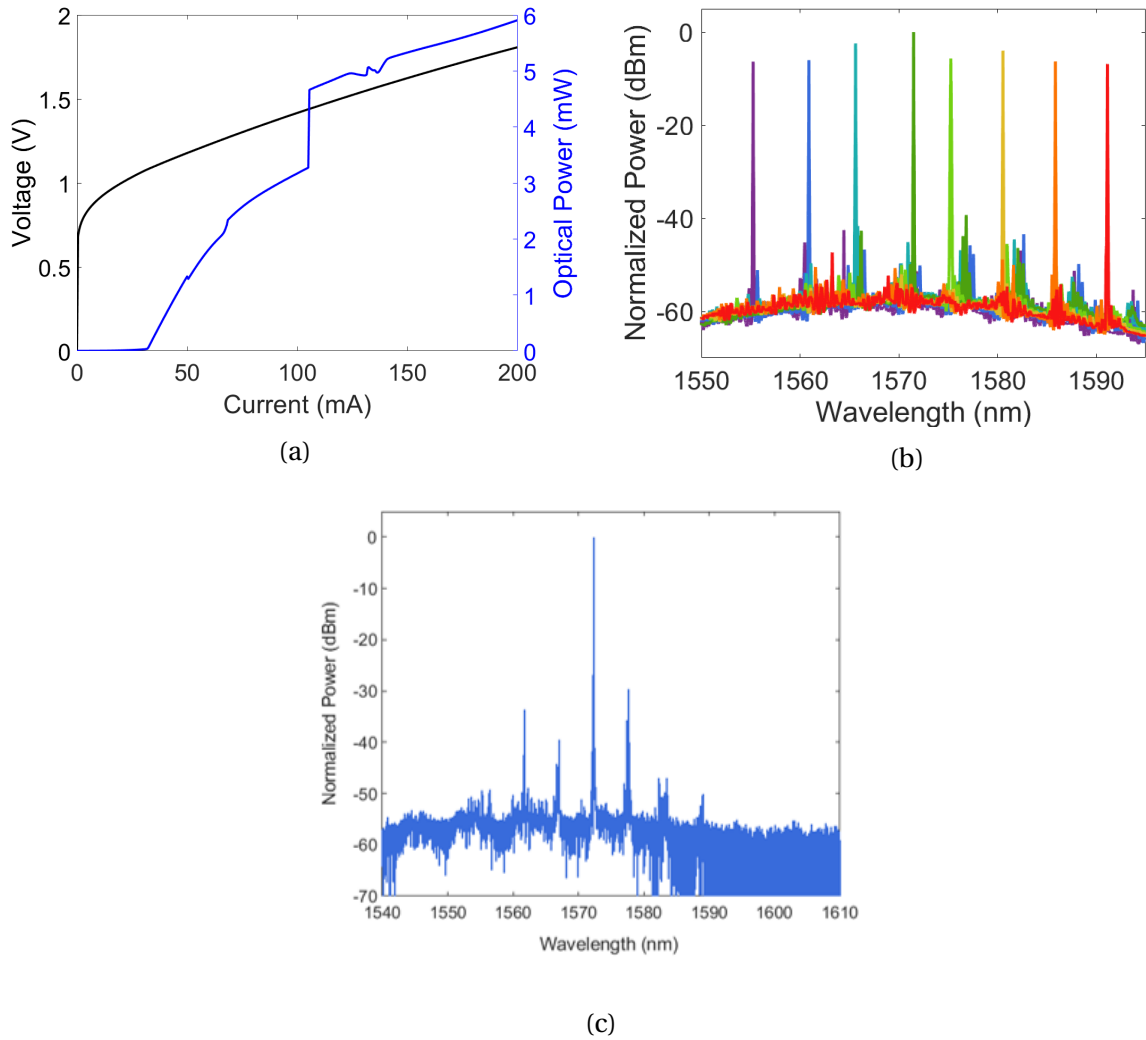
Figure 5.3: Plots showing characterization of first generation SGDBR lasers: (a) light-current-voltage curve, (b) overlaid optical spectra showing the SGDBR laser tuning range, and (c) optical spectrum of SGDBR laser tuned to 1572.335 nm with an SMSR of 30 dB [2].

first generation design, but updated to correct the center wavelength. The center wavelength of the designs was chosen to be a couple of nanometers red-shifted from 1572.335 nm. This was done for convenience, since injecting current into the mirrors blue-shifts the mirror spectrum.

Design B is the same as design A, but with a shorter front mirror sampling period. With a

| | Grating | | Rear Mirror | | | | Front Mirror | | | | |
|---|---|---|---|---|---|---|---|---|---|---|---|
| Design | Etch Depth (nm) | Period (nm) | # of bursts | Burst Length (μm) | Sampling Period (μm) | Δλ (nm) | Number of bursts | Burst Length (μm) | Sampling Period (μm) | Δλ (nm) | Center Wavelength (nm) |
| A | 100 | 244 | 12 | 6.1 | 61.5 | 5.3 | 5 | 3.904 | 68.295 | 4.7 | 1574.6 |
| B | 100 | 244 | 12 | 6.1 | 61.5 | 5.3 | 5 | 3.904 | 52.744 | 6.1 | 1574.6 |
| C | 100 | 244 | 12 | 6.1 | 61.5 | 5.3 | 4 | 5.124 | 45.703 | 7 | 1574.6 |

Figure 5.4: Design parameters for second generation SGDBR lasers.

shorter front mirror sampling period, the total front mirror reflectivity is increased and the total length of the front mirror is decreased. The shorter sampling period also results in a larger channel spacing. Design A has a front mirror channel spacing of 4.7 nm and design B has a front mirror channel spacing of 6.1 nm. Design A was optimized for continuous tuning across the entire tuning range, so the channel spacing was kept narrow. But, as can be seen by comparing Figure 5.5(b) and (d), by increasing the difference in channel spacing between the rear and front mirrors, the overlap of the next adjacent supermodes is reduced, potentially resulting in a better SMSR than design A over the whole tuning range, while potentially sacrificing continuous tunability, depending on the wavelength shift achievable in the intermixed material.

In design C, the front mirror sampling period is further reduced for a front mirror channel spacing of 7 nm. As can be seen in Figure 5.5(f), the relative channel spacing of the rear and front mirrors results in secondary supermodes forming farther from the center supermode than in the case of design A or B. Although the reflectivity of the secondary supermodes is greater in design C than in design B, the secondary supermodes are farther from the designed gain peak. To keep the front mirror reflectivity approximately the same as the
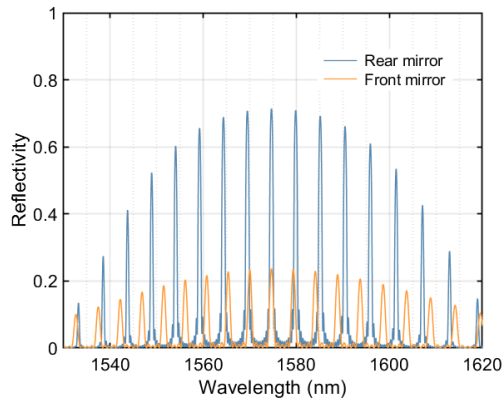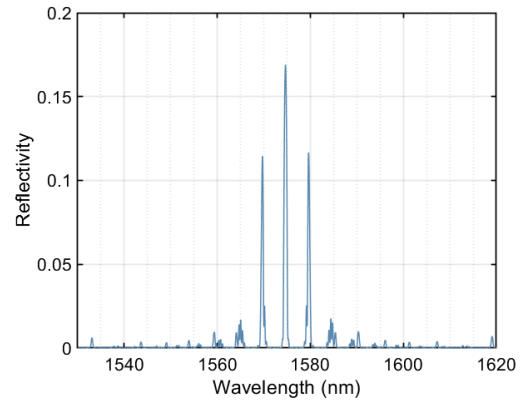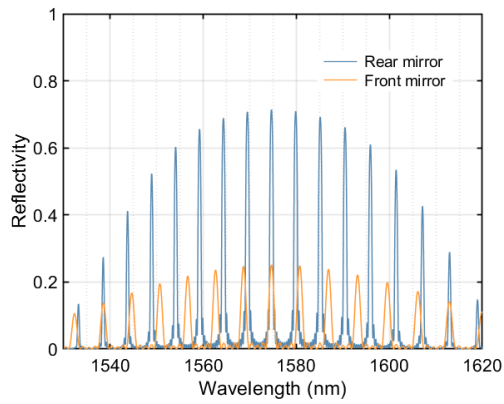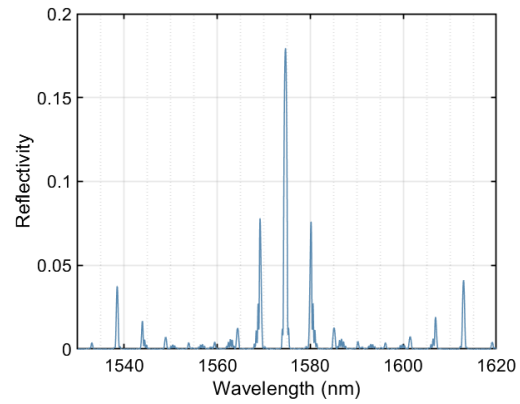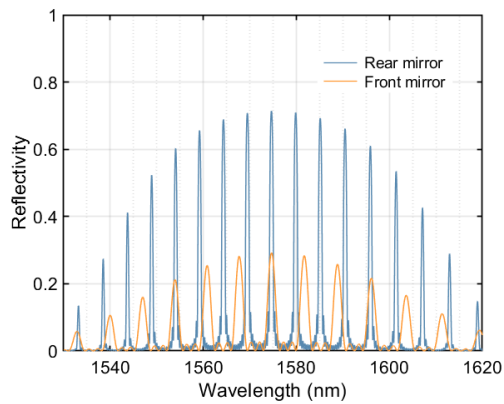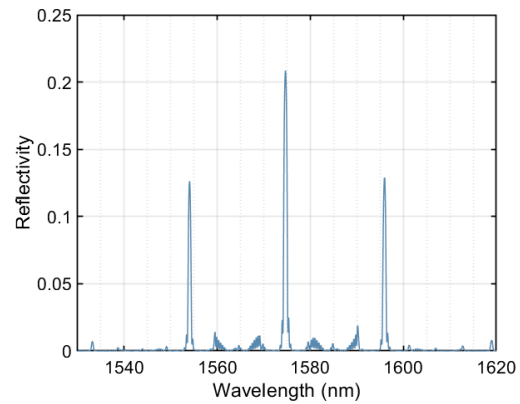
Figure 5.5: Calculated response of the second generation SGDBR laser mirrors. (a),(c),(d): The rear and front mirror reflectivity of designs A, B, and C, respectively. (b), (d), (f): Total mirror reflectivity of designs A, B, and C, respectively.

other designs, the number of front mirror bursts is reduced to four. The reduction in burst length and number of bursts, gives SGDBR design C the shortest front mirror. Less passive loss in the front mirror could lead to higher output power.

In summary, design A is the design from the first generation with the parameters updated to reach the target wavelength. Since output power and SMSR are more important for the $CO_2$ lidar PIC than wide and continuous tunability (as long as the target wavelength is reached), designs B and C compromise tunability for potential gains in SMSR and output power.

Figure 5.6 plots the light-current-voltage (LIV) curves for SGDBR laser designs A, B, and C. The power output of each laser was measured by an SOA immediately following the laser and a stage temperature of 20 °C. The fluctuation in power is most likely due to mode hops. The three laser designs had a similar LIV performance with threshold currents of 25 mA and maximum output powers of about 30 mW at a 200 mA gain section bias. The power output is much improved from the first generation design, which showed 6 mW of output power at a 200 mA gain section bias.

The tuning and SMSR performance of the SGDBR lasers is shown in Figure 5.7. As expected, the supermode spacing increases from design A through design C which can be seen in Figure 5.7(a), (c), and (e). The SMSR along with the rear and front mirror current used for tuning to each supermode is plotted for each design in Figure 5.7(b), (d), and (f). Over all of the supermodes, design C has the highest mean and median SMSR, but design B has the greatest maximum SMSR of 57 dB at 1580.224 nm. Although the amount of index tuning
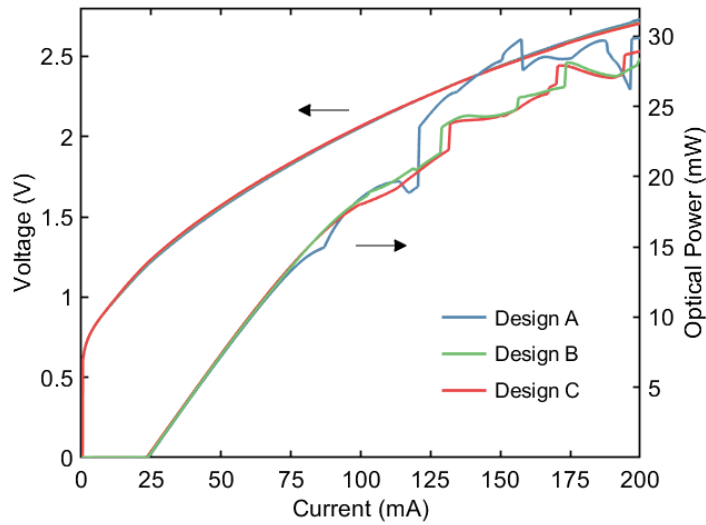
Figure 5.6: Light-current-voltage curves measured for SGDBR laser designs A, B, and C.

was not directly characterized, the tuning of design C was "jumpy" and probably not use-

ful for continuous tuning over the entire tuning range. It also had a narrower tuning range

than designs A and C (about 20 nm versus 30-35 nm). Design B is a reasonable compro-

mise between design A and C in terms of tunability and SMSR, but did not give a significant

improvement in SMSR over design A.


## 5.2   Distributed Feedback Lasers

As discussed in Section 3.2, part of the reason for pursuing the QWI platform was for ease

of integrating DFB lasers, which would be ideal for the single wavelength leader laser on the

$CO_2$ lidar PIC. SGDBR lasers require a grating $\kappa$ value around 300 cm$^{-1}$ whereas DFB lasers

(depending on the length) usually require grating $\kappa$ values less than 100 cm$^{-1}$. Typically in

InGaAsP/InP integration methods, the grating etch depth alone determines the amount of
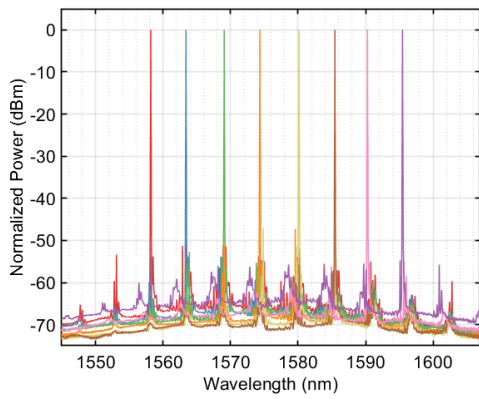
(a) Design A
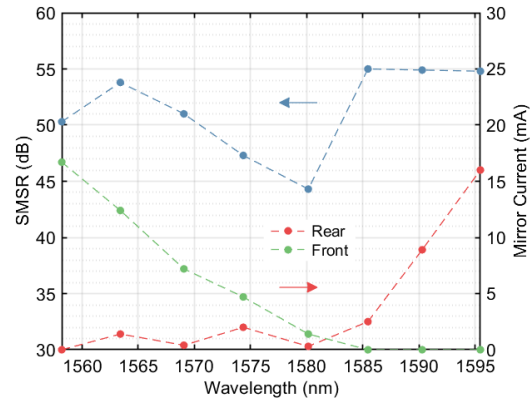
(b) Design A
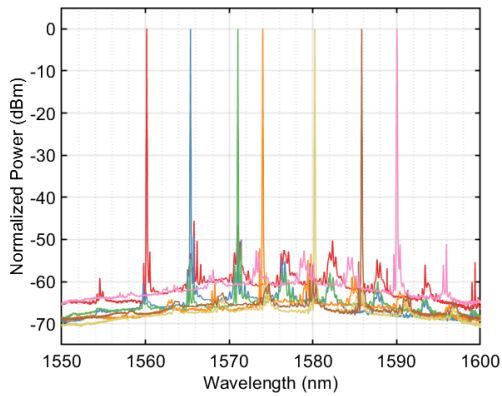
(c) Design B
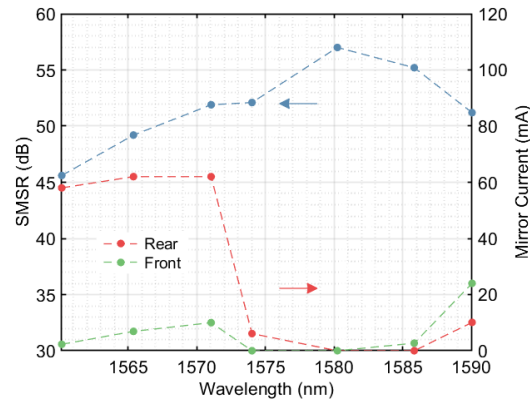
(d) Design B
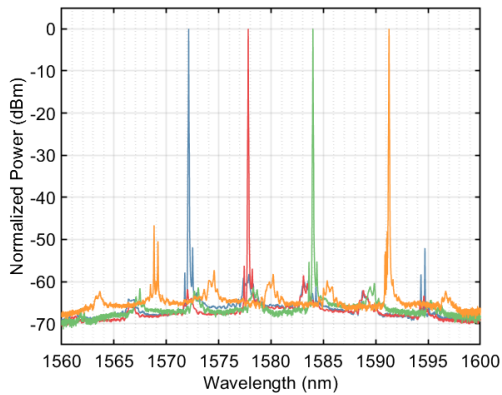
(e) Design C
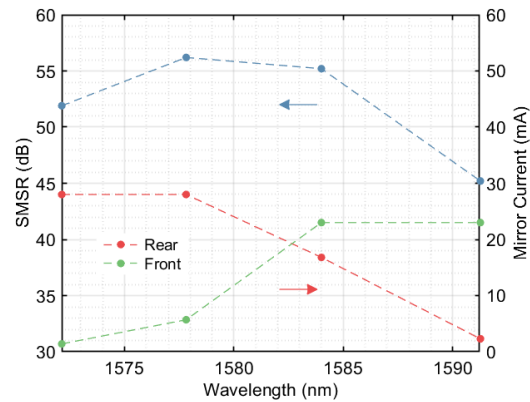
(f) Design C

Figure 5.7: Plots showing characterization of second generation SGDBR laser designs. (a),(c),(d): Overlaid optical spectra showing the tuning range of designs A, B, and C, respectively. (b), (d), (f): SMSR and mirror currents versus lasing wavelength for the tuning of designs A, B, and C, respectively.

76

index contrast in the grating and thus the grating $\kappa$ value. This means that a separate series of EBL patterning and grating etches would be required for each type of laser. Since the grating patterning and etching is a time-consuming and crucial step, a novel approach to the DFB laser grating patterning was used to fabricate the gratings of the SGDBR and DFB lasers in a single lithography and etch series [2].

### 5.2.1   One-Step Grating Formation

Figure 5.8(a) illustrates the novel grating patterning used for the DFB lasers. To reduce the index contrast (and thus $\kappa$ value) of the DFB laser grating, while using the same etch depth as was used for the SGDBR lasers, an unetched gap parallel and centered to the ridge was introduced, called a "fishbone" grating. Figure 5.8(b) plots the simulated grating $\kappa$ and Bragg wavelength versus the grating gap width for a 100 nm grating etch depth. Single mode operation was achieved in all of the designs by including a quarter-wavelength shift halfway through the length of the grating, as depicted in Figure 5.8(a).

### 5.2.2   First Generation

Figure 5.9 gives the design details and simulated grating response of the first generation DFB laser design. As with the first generation SGDBR lasers, the grating period was updated during fabrication, resulting in a grating centered at 1600 nm. Plotted in Figure 5.10 is the measured laser spectrum and LIV curve. The DFB laser exhibited single mode lasing at 1605 nm with an SMSR of 51.6 dB. The threshold current was 30 mA and the maximum output
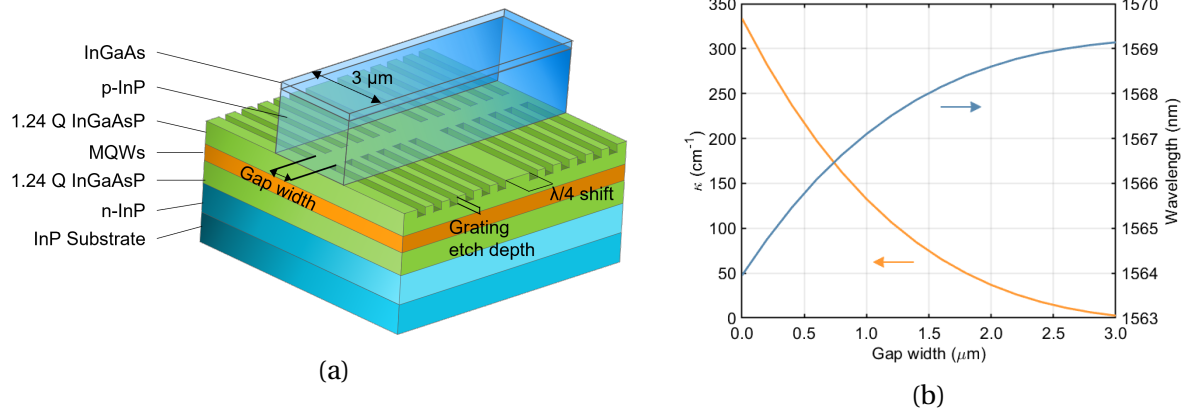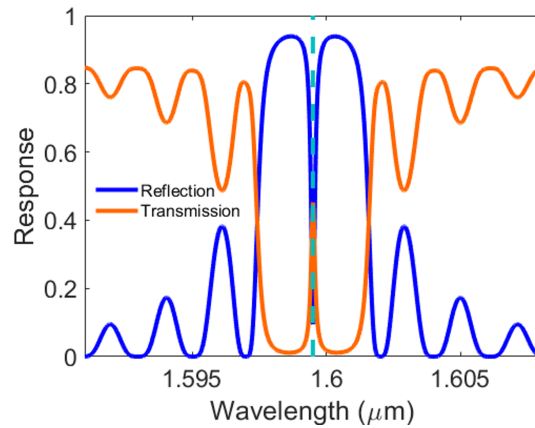
Figure 5.8: (a) Diagram showing the structure of the quarter-wavelength shifted fishbone grating DFB laser [2]. (b) An example of simulated Bragg wavelength and $\kappa$ as a function of fishbone grating gap.

| Etch depth (nm) | 80 |
|---|---|
| Grating period (nm) | 248 |
| Grating gap width (μm) | 1.0 |
| Laser length (μm) | 350 |

(a)



(b)

Figure 5.9: (a) Design parameters and (b) simulated mirror response for the first generation DFB lasers [2].

power was 5 mW at a bias of 150 mA. Just as for the first generation SGDBR lasers, the laser output power was much less than expected. The threshold current was reasonable and the SMSR excellent.

Accurate design and fabrication process control of the DFB laser are crucial to achieving the target wavelength since the laser has very little wavelength tunability. Figure 5.10(c) shows overlaid first generation DFB laser spectra for stage temperatures from 12.5 to 20.2 °C. The tuning achieved for this temperature range is 0.7 nm. Further tuning can be achieved by changing the gain bias current.
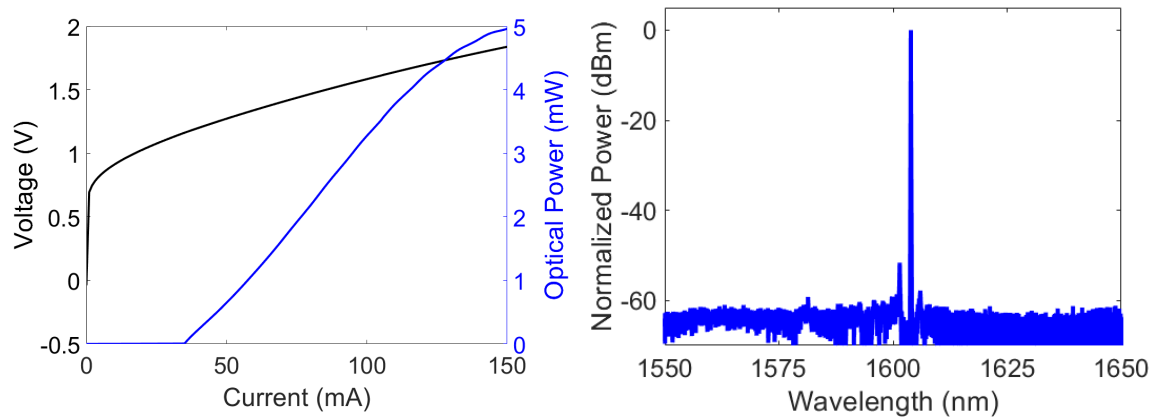
(a)



(b)
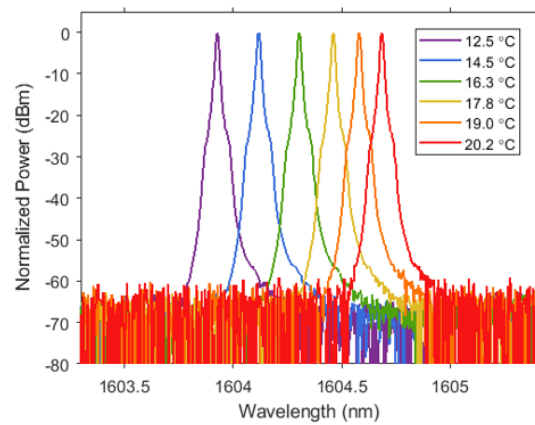


(c)

Figure 5.10: Plots showing (a) LIV curve, (b) optical spectrum, and (c) thermal tuning of first generation DFB laser [2].

### 5.2.3   Second Generation

In the second generation, several DFB laser designs were fabricated. The design parameters of the best performing laser are given in Figure 5.11. The length was increased from 350 $\mu$m to 500 $\mu$m between the first and second generation. The DFB laser length was not extended past 500 $\mu$m because this was limited by the size of the EBL writing field. While it is possible to write a longer grating, there is the possibility of a stitching error between fields. The chosen period of 242 nm gives a simulated center wavelength of 1568.5 nm, as shown in the simulated mirror response plotted in Figure 5.12(a). Patterns written using EBL were limited to a 1 nm grid, so the chosen period had to be an integer multiple of 1 nm. A grating period of 243 nm has a simulated center wavelength of 1573.9 nm, so a designed wavelength of 1572.335 nm could not be exactly targeted.

| | |
|---|---|
| Etch Depth (nm) | 100 |
| Grating period (nm) | 242 |
| Grating gap width (µm) | 1.9 |
| Laser length (µm) | 500 |
| $\lambda_{\text{Bragg}}$ (nm) | 1568.5 |

Figure 5.11: Design parameters of second generation DFB lasers.

As shown in Figure 5.12(c) and (d), the DFB laser exhibited single mode lasing at 1570.5 nm for a bias of 150 mA and with the stage maintained at 20 °C. The SMSR at 1570.5 nm was 60 dB. To tune the laser to 1572.335 nm, the laser bias was increased to 220 mA and the stage temperature was increased to 27 °C. Figure 5.12(e) and (f) show the laser spectrum at

1572.335 nm with an SMSR of 58 dB. Figure 5.12(b) gives the laser LIV curve at 15, 20, and 27 °C. The laser output power exceeds 25 mW at 15 °C, but is still a reasonable 20 mW at 27 °C. The output power was measured by reverse biasing an SOA directly following the laser and assuming a 1 A/W responsivity.

A study of the laser wavelength tuning with bias current and stage temperature was performed and the results are shown in Figure 5.13. As can be seen in Figure 5.13(a), a total wavelength tuning range of about 3 nm is achieved by varying the laser bias current and stage temperature. Figure 5.13(b) and (c) show the laser SMSR and output spectrum with increasing laser current, respectively. Figure 5.13(d) gives the laser LIV performance with temperatures from 14 to 25 °C.

Since the SMSR of DFB lasers is known to degrade with an integrated SOA [3], a study of SMSR versus SOA bias was performed. For the spectrum measurements in Figures 5.12 and 5.13, the laser light was coupled off chip and an SOA behind the DFB laser was reverse biased at -3 V. There was no SOA in front of the laser. In Figure 5.14, a forward bias was applied to the SOA behind the DFB laser to see the effect on SMSR. This is important to examine since a DFB laser acting as the leader laser in the lidar PIC would be subject to back reflections from other components in the PIC. To help reduce the DFB laser sensitivity to back reflections and ASE, a slightly high $\kappa$L value of 2.1 was used.

Figure 5.14(a) shows overlaid DFB laser optical spectra for a rear SOA bias of 30 and 210 mA, illustrating a degradation in SMSR for the higher SOA bias. Figure 5.14(b) plots a measure of the amount of ASE injected into the DFB laser. With the DFB laser reverse biased
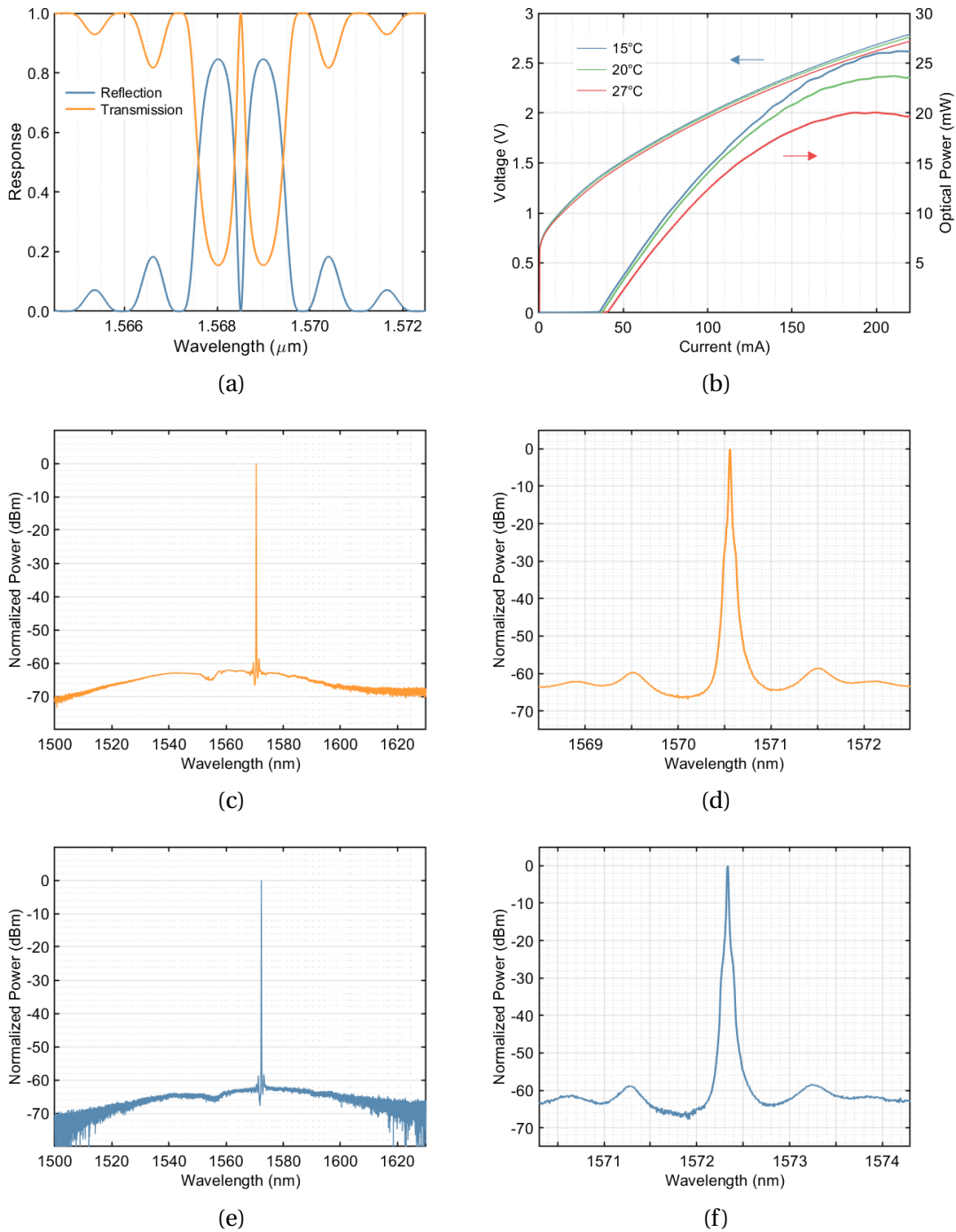
Figure 5.12: Second generation DFB laser design and performance. (a) Simulated DFB laser mirror response. (b) LIV curves at 15, 20, and 27 °C. Laser spectrum at 20 °C for (c) a wide wavelength range showing single mode operation and (d) a narrow wavelength range showing the SMSR of 60 dB. Laser spectrum tuned to 1572.335 nm by setting the stage temperature to 27 °C. (e) shows single mode operation from 1500 to 1620 nm and (f) shows the SMSR of 58 dB.
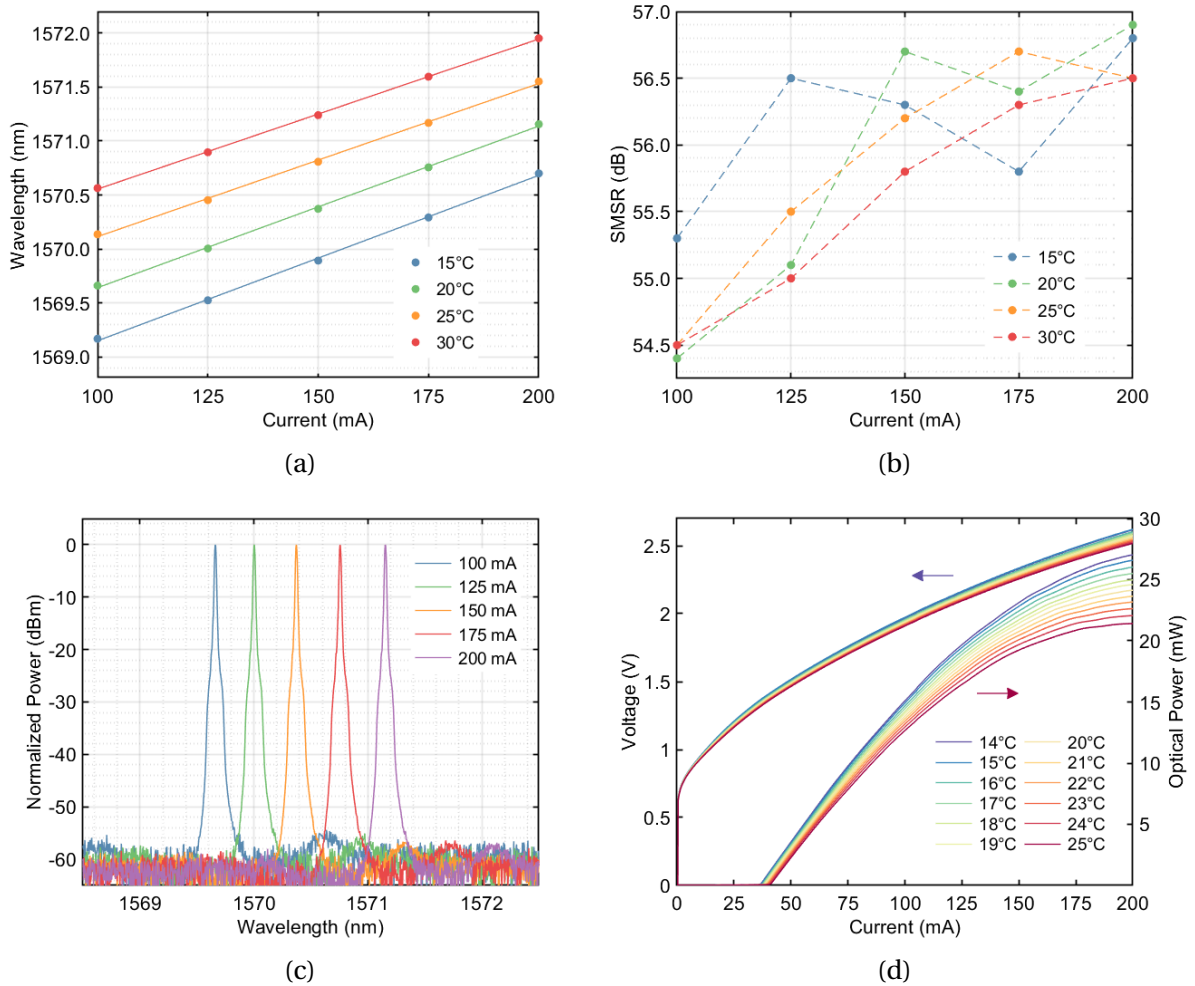
Figure 5.13: (a) Wavelength with current injection from 15 - 30 °C with a linear fit. (b) SMSR with current injection at various temperatures. Dashed lines to guide the eye.(c) Overlaid laser spectra at 20 °C for various bias currents. (d) LIV performance for similar stage temperatures and currents shown in plots (a)-(c).

at -3V, the photocurrent at the DFB laser was measured as the SOA current was increased. Assuming a 1 A/W responsivity, about 0.5 mW of peak ASE power makes into the DFB laser cavity. Figure 5.14(c) and (d) plot the DFB laser SMSR as a function of laser current and rear SOA current, respectively. As the SOA current increases from 30 to 210 mA, the DFB laser SMSR degrades from about 55 to 51.5 dB for a laser current of 200 mA. Although the SMSR degrades as expected, an excellent SMSR is still maintained.
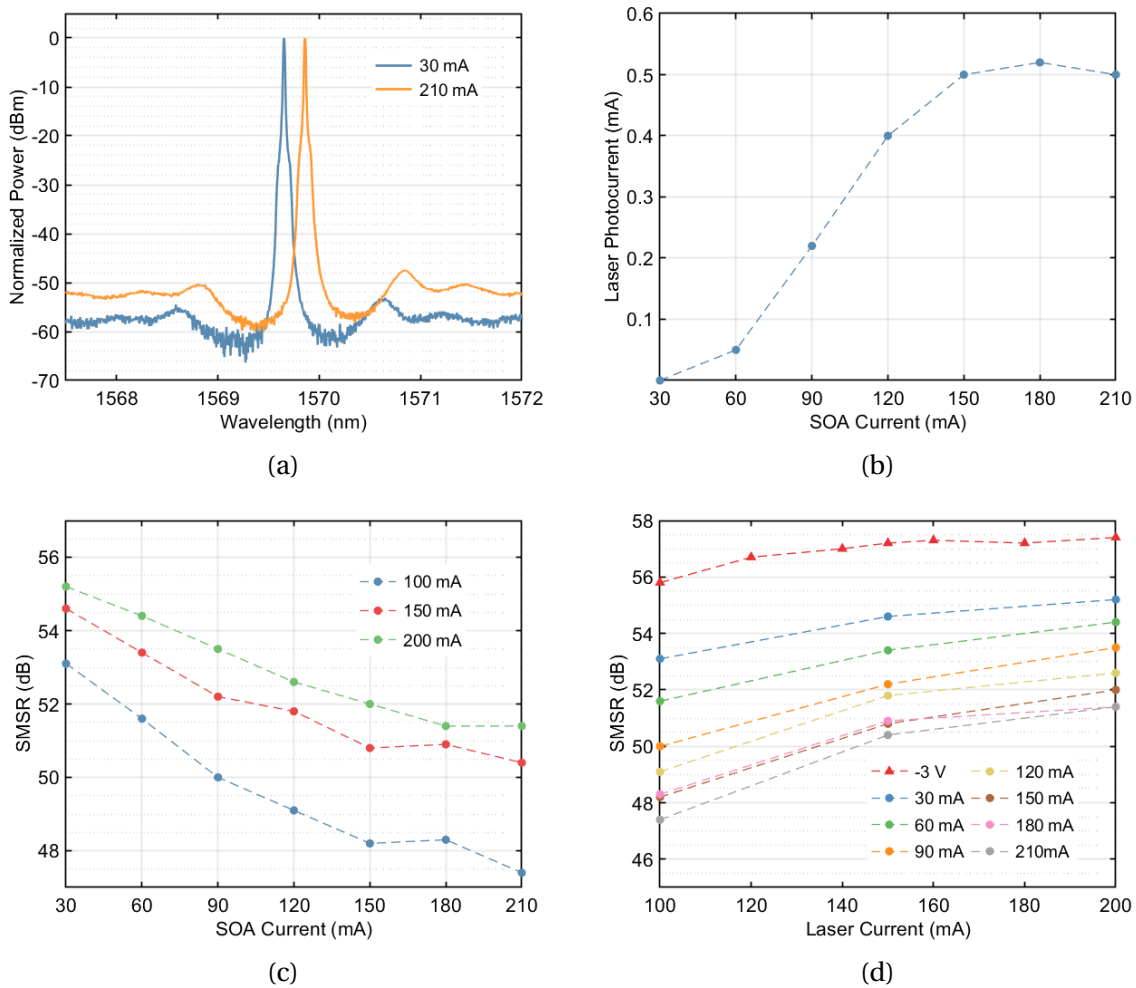
Figure 5.14: Study of the effect of ASE on DFB laser SMSR. (a) DFB laser spectrum showing a decrease in SMSR for a rear SOA bias of 30 versus 210 mA. (b) ASE power into the DFB laser as measured by photocurrent generated at the DFB laser reverse biased at -3 V. (c) DFB laser SMSR versus rear SOA current for various laser biases. (d) DFB laser SMSR as a function of laser current for various rear SOA biases.

To demonstrate that the one-step grating method is effective for fabricating lasers with different grating $\kappa$ values on the same sample, the performance of an SGDBR laser from the same bar as the DFB lasers characterized in Figures 5.12, 5.13, and 5.14 was measured. The data is plotted in Figure 5.15. The laser spectrum plotted in Figure 5.15(d) and (e) was measured with a stage temperature of 27 °C, to show that the SGDBR laser can be tuned to 1572.335 nm at the same temperature as that required to tune the DFB laser to 1572.335 nm.

**Super-period Gratings**

As stated earlier, increasing the DFB laser period by 1 nm results in a simulated center wavelength of 1573.9 nm. Because the placement of written features is limited to a 1 nm resolution grid for the EBL tool, a wavelength of 1572.335 nm could not be exactly targeted with the existing epitaxial material structure. To confirm this, the spectrum from a DFB laser fabricated with a 243 nm period is plotted in Figure 5.16. At a stage temperature of 20 °C and laser bias of 150 mA, the center wavelength is 1577 nm, which cannot be tuned down to 1572 nm.

Although the 242 nm period DFB laser design was able to be tuned to 1572.335 nm, the temperature had to be increased to reach the target wavelength, which degrades the power output. To remedy this, several DFB designs with a superstructured period were included. Adapted from [4], the superstructure grating periodically alternates between two different grating periods. Figure 5.17 gives the design parameters of the best performing superstructured DFB laser and illustrates the grating pattern. Figure 5.18(a) gives the simulated DFB mirror spectrum for the design in Figure 5.17. Figure 5.18(b) and (c) plot the DFB laser
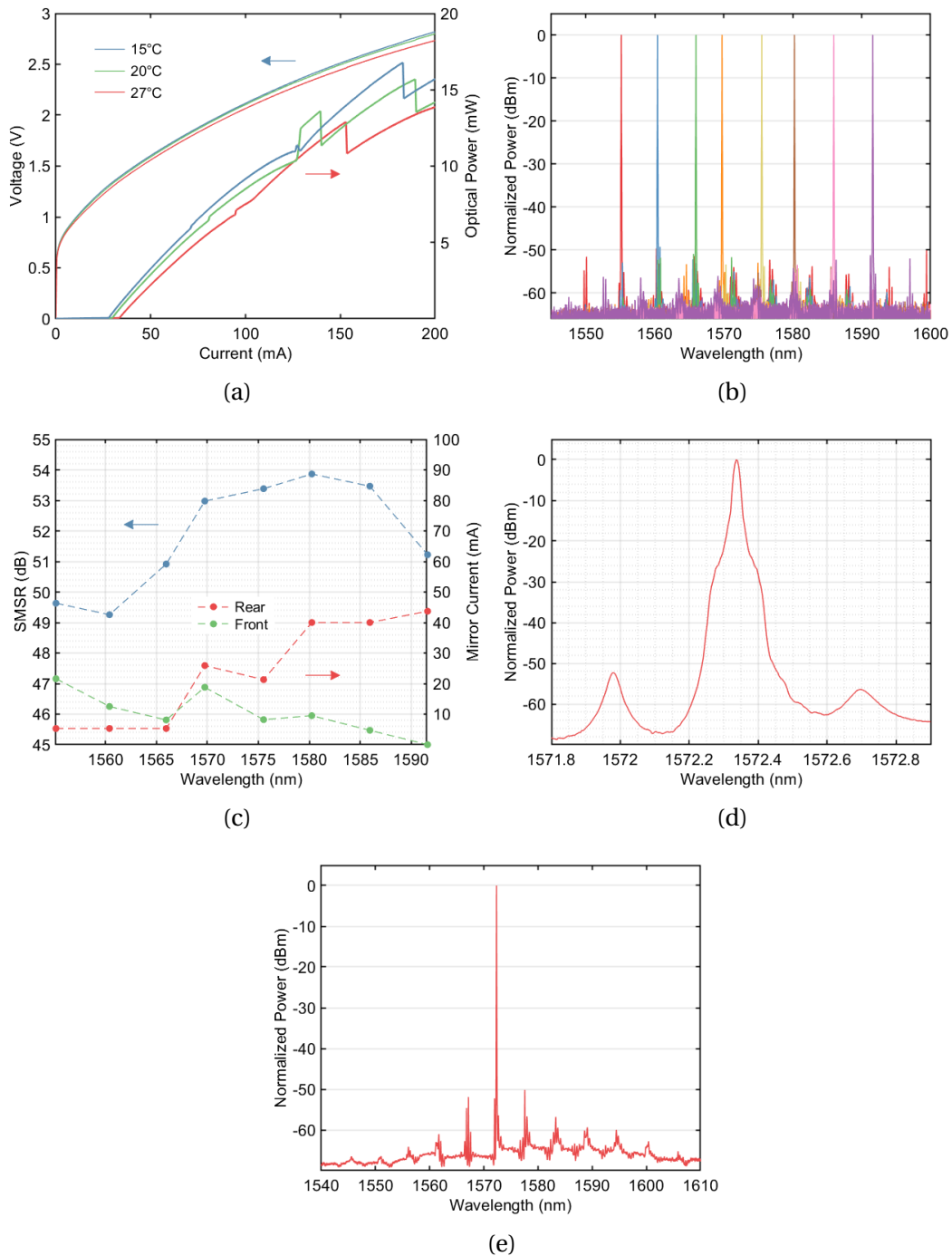
Figure 5.15: Characterization of SGDBR laser from the same sample as the fishbone grating DFB laser: (a) LIV curve, (b) overlaid optical spectra with mirror tuning, (c) SMSR and mirror current versus lasing wavelength, and optical spectrum at 1572.335 nm plotted in a narrow (d) and wide (e) wavelength range.

spectrum over a wide and narrow wavelength range, respectively. The lasing wavelength was 1572.335 nm for a stage temperature of 18.5 °C and a 103 mA bias current. Despite the presence of a second longitudinal mode, the SMSR was 49 dB. The LIV curve plotted in Figure 5.18(d) shows a threshold current of 30 mA and a maximum output power of about 27 mW at a 200 mA bias.
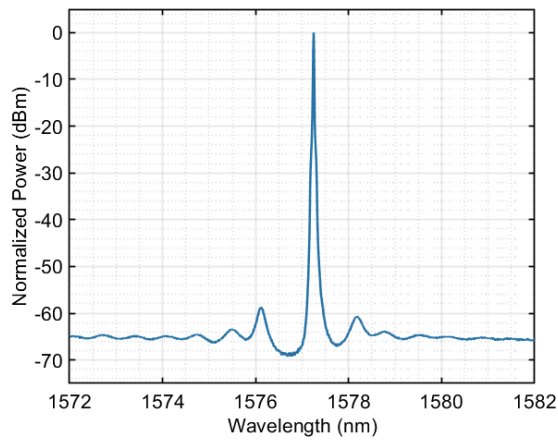


Figure 5.16: Spectrum of DFB laser with 243 nm period yielding a lasing wavelength of 1577 nm at 20 °C and 150 mA.

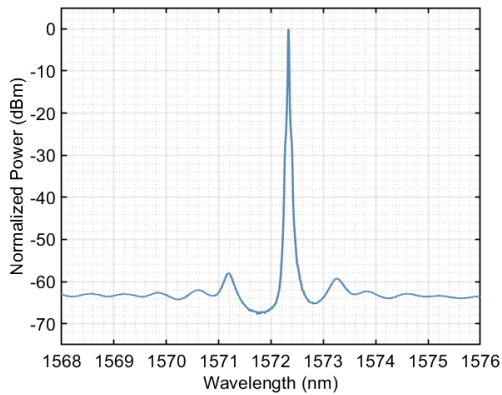| | |
|---|---|
| Etch Depth (nm) | 100 |
| Grating period 1 (nm) | 241 |
| Period 1 repeat | 4 |
| Grating period 2 (nm) | 243 |
| Period 2 repeat | 7 |
| Grating gap width (µm) | 1.9 |
| Laser length (µm) | 500 |
| $\lambda_{Bragg}$ (nm) | 1570.0 |

(a)
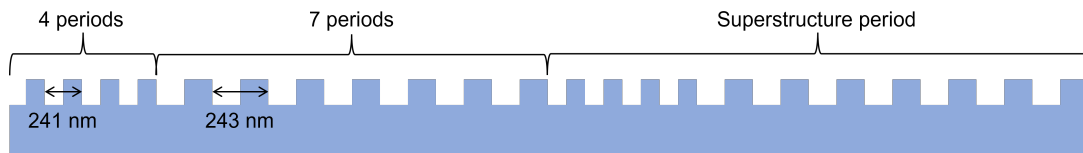


(b)

Figure 5.17: (a) Design parameters for super-period DFB laser. (b) Diagram showing arrangement of the alternating periods in the super-structured grating.
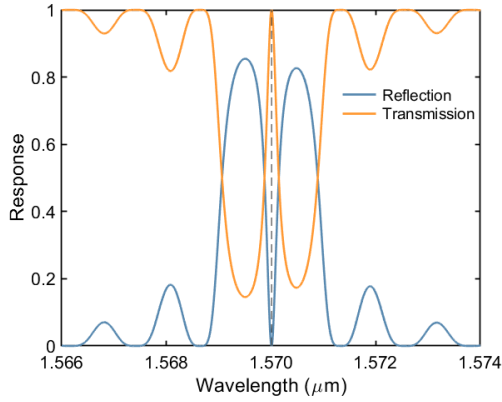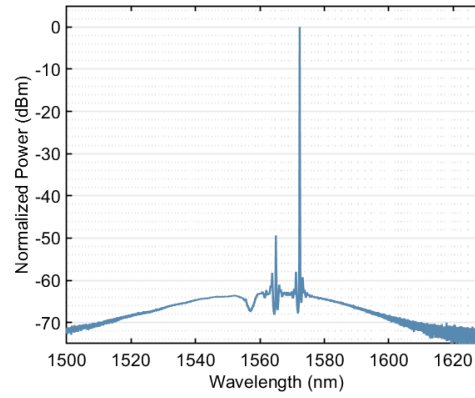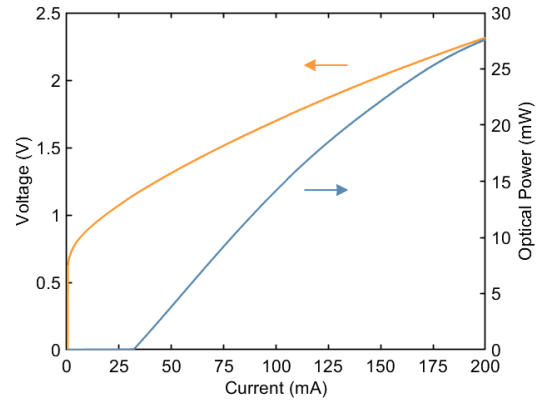
Figure 5.18: (a) Simulated mirror response of the super-structure grating design from Figure 5.17(a). Measured spectrum of the superperiod grating DFB laser at 19 °C and 103 mA bias for (b) a wide wavelength range showing 50 dB SMSR and (c) narrow wavelength range showing the center wavelength is at 1572.335 nm. (d) LIV curve of superperiod DFB laser at 19 °C.

## 5.3   Chapter Summary

Chapter 5 discussed the SGDBR and DFB laser designs and characterization for two generations of devices. Significant improvements were obtained in the second generation due to an updated choice of grating period and changes to the fabrication process based on learning from the first generation. In the first generation, the SGDBR laser peak output power was 6 mW and the SMSR at 1572 nm was 30 dB, whereas the second generation SGDBR lasers reached an output power of up to 30 dB and a 50 dB SMSR at 1572 nm. The first generation DFB lasers had an emission wavelength of 1600 nm with a peak output power of about 5 mW. The second generation DFB lasers had a 58 dB SMSR at 1572 nm and output up to 25 mW of optical power. Future work should include a study of the linewidth and noise characteristics of the fishbone DFB laser design as compared to SGDBR lasers fabricated on the same sample.

## References

[1]   L. A. Coldren, S. W. Corzine, and M. L. Masanovic, *Diode Lasers and Photonic Integrated Circuits, 2nd Edition.* Hoboken, NJ: John Wiley and Sons, Inc., 2012.

[2]   V. Rosborough, F. Sang, J. Fridlander, H. Zhao, B. Song, S. T. S. Brunelli, J. R. Chen, M. A. Stephen, L. Coldren, and J. Klamkin, "Monolithic integration of widely-tunable dbr and dfb lasers with one-step grating formation," *OSA Advanced Photonics Congress Integrated Photonics Research (IPR)*, 2019.

[3]  B. Moeyersoon, G. Morthier, and M. Zhao, "Degradation of the mode suppression in single-mode laser diodes due to integrated optical amplifiers," *IEEE Journal of Quantum Electronics*, vol. 40, no. 3, pp. 241–244, 2004.

[4]  C. Kaden, U. Griesinger, H. Schweizer, and M. H. Pilkuhn, "Fabrication of nonconventional distributed feedback lasers with variable grating perids and phase shifts by electron beam lithography," *Journal of Vacuum Science and Technology B*, vol. 10, no. 6, pp. 2970–2973, 1992.

# Chapter 6

# Phase Modulator Design and Performance

Time-varying residual amplitude modulation (RAM) (unwanted intensity fluctuation in a phase modulated system) is known to be the main source of noise in the frequency modulation locking technique used to stabilize the leader laser [1]–[5]. Most RAM is generated in the phase modulator. In LiNbO$_3$ phase modulators, RAM has been studied extensively and is mainly due to etalon and photorefractive effects and polarization misalignment [1], [5]. RAM has not been thoroughly studied and optimized in InP-based phase modulators. Due to the phase modulation mechanisms in InP-based modulators, there is always some absorption loss associated with the desired refractive index change as illustrated in Figure 6.1. In reverse bias, propagation loss increases with reverse bias due mainly to electro-absorption effects. In bulk material waveguides, electro-absorption manifests as the Franz-Keldysh effect. In the presence of quantum wells, electro-absorption occurs through the quantum confined Stark effect (QCSE). In this chapter, offset quantum well (OQW) devices

94

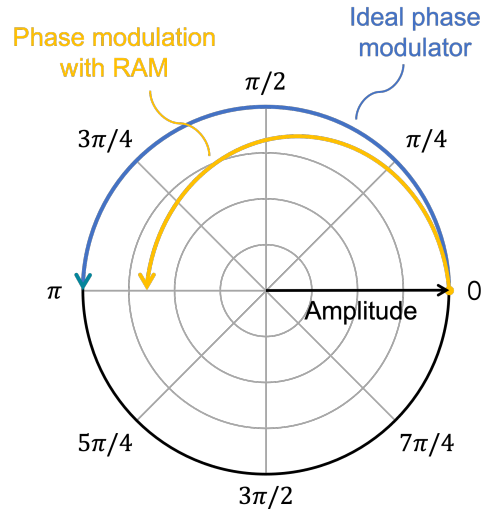with a bulk 1.3Q InGaAsP waveguide layer will be discussed.



Figure 6.1: Cartoon polar plot illustrating phase change for an ideal (pure) phase modulator versus an InGaAsP/InP phase modulator with residual amplitude modulation due to electro-absorption.

In one study that has been done on the effect of RAM in InP-based phase modulators on Pound-Drever-Hall laser stabilization, it was found that frequency deviations from the locking point less than $3x10^{-3}$ of the full-width half-maximum (FWHM) of the reference spectrum could be achieved using a bulk InGaAsP reverse biased waveguide phase modulator [3], [6]. For the case of the $CO_2$ lidar PIC, the FWHM of the reference $CO_2$ absorption line is 3.3 GHz. According to the findings in [3], the achievable frequency deviation is limited to about 9.9 MHz. While this meets the minimum requirement of less than 100 MHz center wavelength drift for the $CO_2$ lidar system, there is room for improvement to make InP-based PICs widely viable for applications requiring low-RAM phase modulators such as quantum communications, spectroscopy, and gyroscopes. To this end, a "shift-and-dump" phase shifter (SDPS) design first demonstrated in a silicon on insulator platform [7], [8] was

adapted for the InP platform. The SDPS is a Mach-Zehnder interferometer-based device with directional couplers at the input and output as shown in Figure 6.2. By choosing the correct phase modulator length and directional coupler splitting ratios, the device yields an almost constant total loss despite varying loss in the modulated arm. The exact definition of RAM is the ratio of the intensity fluctuation and the power in the purely phase modulated signal, but just the change in intensity will be discussed here [5].
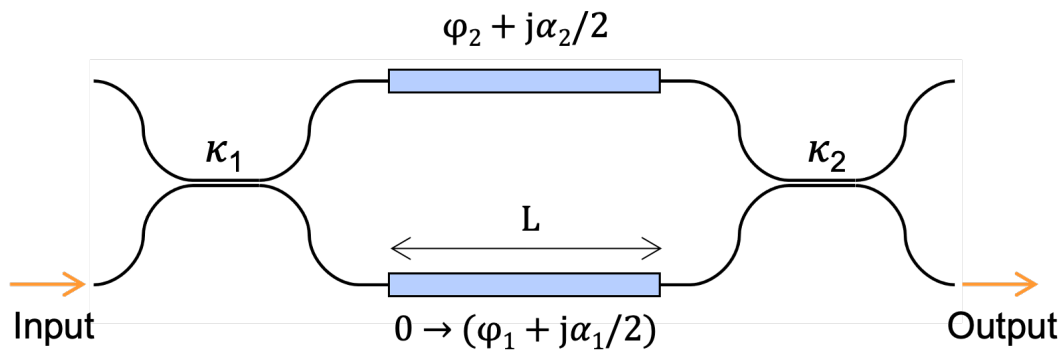


Figure 6.2: Diagram of the SDPS for operation in an InGaAsP/InP material platform [9].

## 6.1 Straight Phase Modulator Characterization

The first generation straight waveguide phase modulators were characterized to extract the phase modulation efficiency and loss with reverse bias. A cross section of the phase modulator waveguide and the corresponding optical mode are shown in Figure 6.3.

The method described in [10] was used to characterize the phase modulator efficiency and the test setup is diagrammed in Figure 6.4. The linear component of the Fourier spectrum of the phase modulation is plotted in Figure 6.5 for a modulation speed of 500 kHz
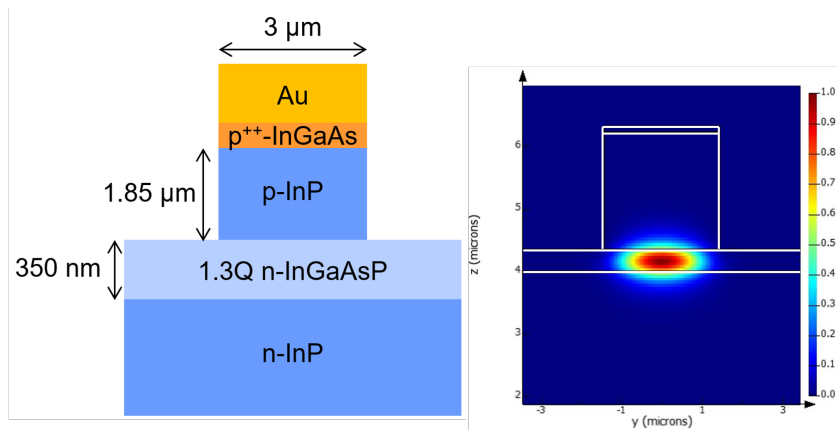
Figure 6.3: Left: Waveguide structure for the SDPS device [9]. Right: Simulated optical mode profile in the SDPS waveguide.

around a bias point of -1.5 V. The modulation efficiency was approximately 30°/Vmm. Once

the modulation efficiency was characterized, which gives the required reverse bias to achieve

the desired phase shift for a given modulator length, the loss with reverse bias needed to be

characterized to find the absorption loss at the needed applied bias.
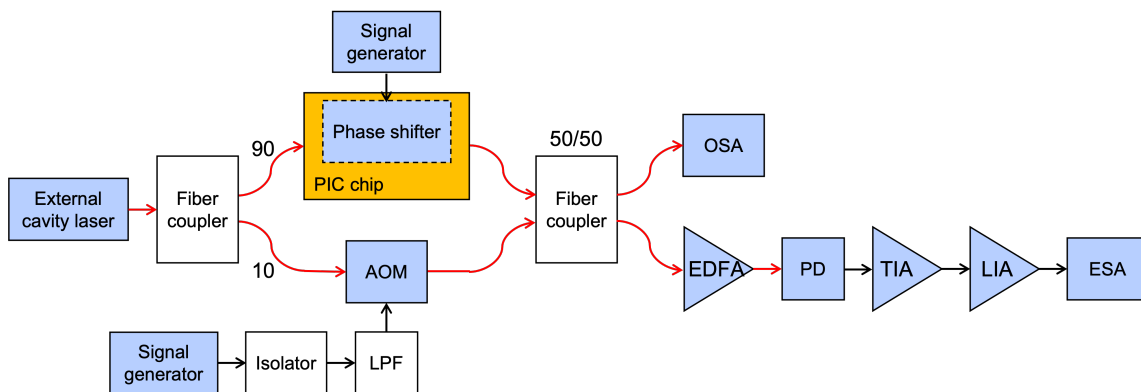


Figure 6.4: Test setup used to characterize the phase modulator efficiency [9].

Loss as a function of reverse bias was measured using a test structure consisting of an

integrated SGDBR laser and 2.5 mm long straight phase modulator as shown in Figure 6.6.

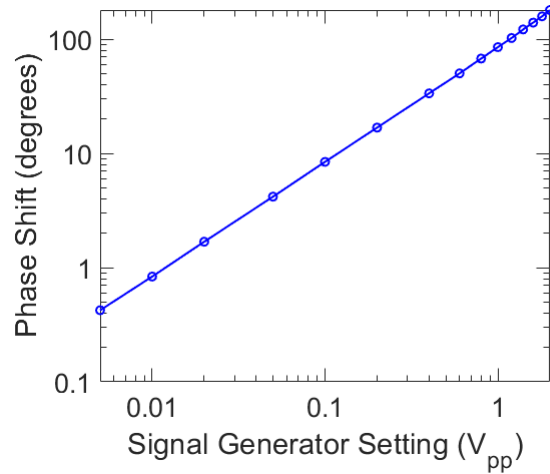The photocurrent generated in the reverse biased phase modulator was measured with the

97

Figure 6.5: Plot showing the linear component of the Fourier spectrum of the phase modulation as measured by the test setup shown in Figure 6.4 [9].

laser turned on and used to calculate the absorption loss with reverse bias. The results are
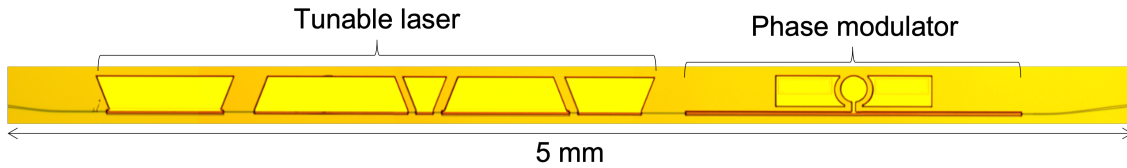
plotted in Figure 6.7.



Figure 6.6: Optical micrograph of laser plus phase modulator test structure used to characterize absorption loss in the straight waveguide phase modulator.

## 6.2   Low-RAM Phase Modulator Design and Characterization

This section begins with a description of the modelling and design of the SDPS low RAM

phase modulator. To minimize the RAM at the output of the SDPS, the transmission at zero

phase shift is set equal to the transmission at the maximum phase shift:
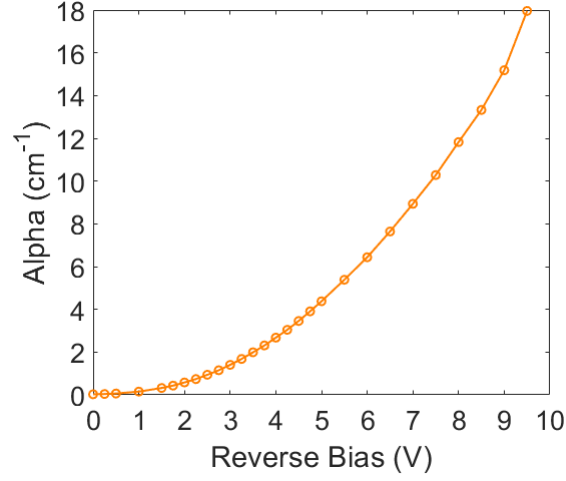
98

Figure 6.7: Plot of the absorption coefficient as a function of reverse bias in the OQW straight waveguide phase modulator [9].

$$T_{out}(\varphi_1 + j\frac{\alpha_1}{2}) = T_{out}(0)e^{j\varphi_1} \tag{6.1}$$

To keep the directional couplers as short as possible, given the difficulty of accurately resolving the 1 $\mu$m gap between the coupler waveguides, the power coupling ratio was kept < 0.5. Since most of the light needs to go to the phase modulated arm, this means that the phase modulated arm is placed at the throughput arm of the directional couplers, as depicted in Figure 6.2. For the device configuration shown in Figure 6.2, $T_{out}(\varphi_1 + j\frac{\alpha_1}{2})$ becomes:

$$T_{out}(\varphi_1 + j\frac{\alpha_1}{2}) = P_{in}[\sqrt{(1-\kappa_1)(1-\kappa_2)}e^{(j\varphi_1 - \frac{\alpha_1\Gamma L}{2})} - \sqrt{\kappa_1\kappa_2}e^{(j\varphi_2 - \frac{\alpha_2\Gamma L}{2})}] \tag{6.2}$$

With $\varphi_1$ and $\alpha_1$ being the maximum phase shift and corresponding loss on the modulated arm and $\varphi_2$ is a constant bias applied to the top arm with accompanying loss $\alpha_2$. $\Gamma$ is the confinement of the optical mode in the modulator material and L is the modulator length. The negative sign in front of the second term in Equation 6.2 comes from a factor of $e^{j\pi}$

representing the 90° phase shift that occurs at each directional coupler crossover. $\kappa_1$ and $\kappa_2$ are the directional coupler power coupling coefficients. Similarly, $T_{out}(0)$ becomes:

$$T_{out}(0) = P_{in}[\sqrt{(1-\kappa_1)(1-\kappa_2)} - \sqrt{\kappa_1\kappa_2}e^{(j\varphi_2 - \frac{\alpha_2\Gamma L}{2})}] \tag{6.3}$$

Equation 6.1 then becomes:

$$e^{j\varphi_1}\sqrt{(1-\kappa_1)(1-\kappa_2)}(1-e^{\frac{-\alpha_1\Gamma L}{2}}) + e^{j\varphi_2 - \frac{\alpha_2\Gamma L}{2}}\sqrt{\kappa_1\kappa_2}(1-e^{j\varphi_1}) = 0 \tag{6.4}$$

An electrical pad was included on the opposite (non-modulated) arm for testing, but, to simplify the design, $\varphi_2$ was set to 0. In addition, to limit the number of solutions without compromising the device performance, the splitting ratios of the two directional couplers were set equal to one another ($\kappa_1 = \kappa_2 = \kappa$), resulting in:

$$e^{j\varphi_1}\sqrt{(1-\kappa)(1-\kappa)}(1-e^{\frac{-\alpha_1\Gamma L}{2}}) + \kappa(1-e^{j\varphi_1}) = 0 \tag{6.5}$$

Equation 6.5 is the characteristic equation of the SDPS that must be solved to achieve low RAM. With knowledge of the straight modulator loss, $\alpha_1$, at the maximum desired phase shift, $\varphi_1$, for a given length, L, equation 6.5 is solved for $\kappa$.
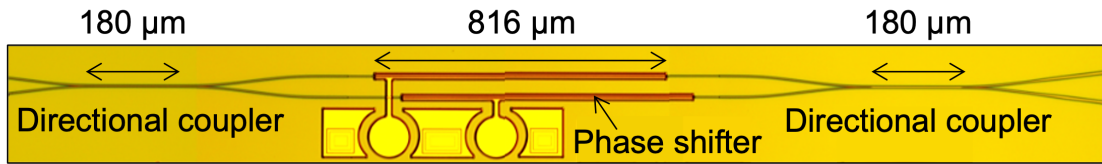


Figure 6.8: Optical microscope photo of fabricated SDPS [9].

Figure 6.8 shows an optical micrograph of the fabricated SDPS device. To fit in the mask set, the longest SDPS arm length that could be used was 816 $\mu$m. Based on this arm length and the results from characterizing the straight phase modulators, the ideal value for the directional coupler power splitting ratio was found to be $\kappa = 0.15$ for a $\pi$ phase shift. To

find the required directional coupler length to achieve the desired $\kappa$ value, simulations using Lumerical's eigenmode expansion (EME) solver were performed. Figure 6.9 shows the structure of the directional couplers used in the SDPS and PICs. To minimize the directional coupler length while keeping a minimum gap of 1 $\mu$m, the waveguides were tapered down from 3 $\mu$m to 2 $\mu$m in the coupling region. Figure 6.10 plots the simulated power coupling ratio versus directional coupler length for both the through and cross ports. The coupling ratio does not quite go to zero for a directional coupler length of zero. This is because some coupling occurs in the input bends to the straight section of the directional coupler and, in the simulation setup, the power was monitored at the start and end of the straight section only.

The measured DC transmission through the low RAM SDPS is plotted by the black line in Figure 6.11. The total change in transmission for $\pi$ phase shift was 1.98 dB. A constant bias of 2 mA was applied to the opposite arm to achieve the flattest response. The corresponding change in transmission for a 816 $\mu$m long straight phase modulator was calculated to be 3.85 dB. Since a straight phase modulator with a length of 816 $\mu$m was not fabricated, the expected loss for an 816 $\mu$m long phase modulator was calculated based on the measurements of the 2.5 mm long straight phase modulator. The plotted transmission is normalized to compare the change versus phase shift, so the insertion loss is not reflected in the plot. The insertion loss for the SDPS device is greater than that of the straight phase shifter.

The tested SDPS device had directional couplers with a length of 180 $\mu$m, which had a simulated power splitting ratio of 0.24. The actual splitting ratio of the fabricated couplers

was estimated in two ways. Firstly, both SDPS arms, which were the same length, were reverse biased and the measured photocurrents were used to calculated the splitting ratio. This yielded a splitting ratio of 0.12. The simulated SDPS transmission for a power splitting ratio of 0.12 is shown by the orange dotted line in Figure 6.11 and gives a maximum change of 1.41 dB in transmission. The second method for estimating the actual power splitting ratio was to find the best fit to the data. A $\kappa$ value of 0.09 gives the best fit to the data, which is close to the measured value of 0.12. The measured splitting ratio of 0.12 was about half of the designed splitting ratio of 0.24. This is most likely due to inaccuracy in the fabrication of the directional coupler gap, which strongly affects the splitting ratio.
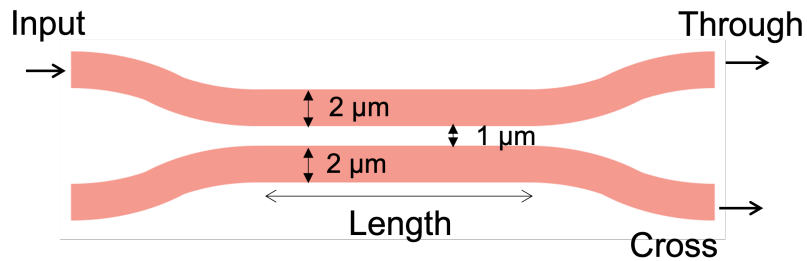
Figure 6.9: Diagram showing top-down structure of directional couplers.
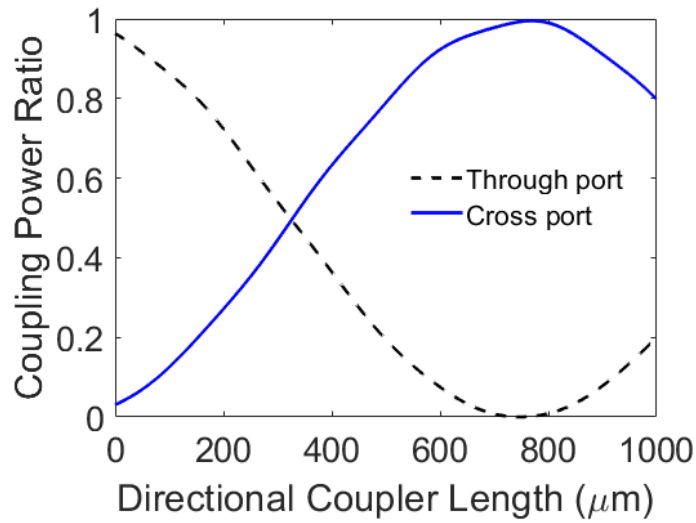
Figure 6.10: Simulated power splitting ratio of directional coupler versus length. Simulation was performed using Lumerical's EME solver.
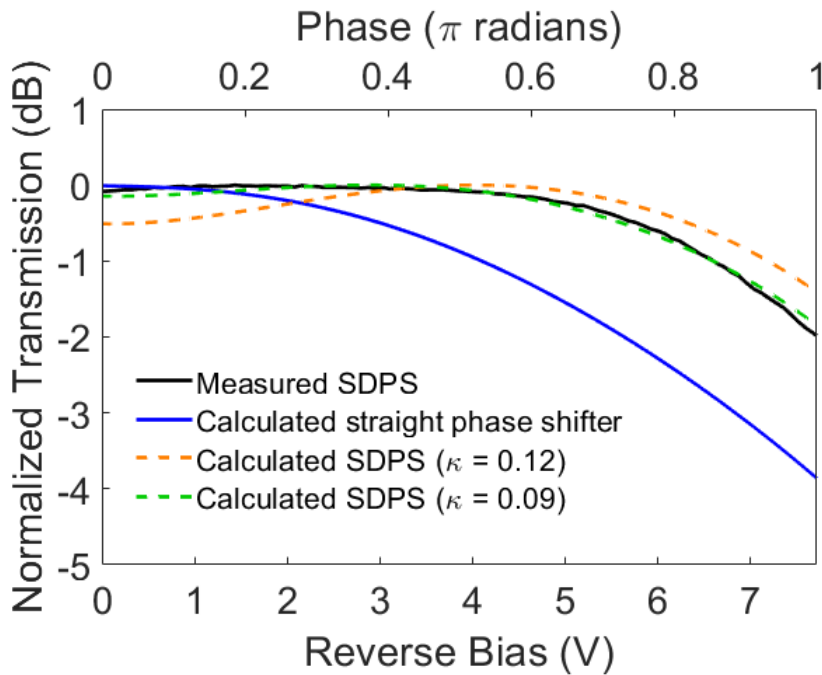


Figure 6.11: Transmission with reverse bias through the SDPS (black line) compared to the expected transmission for a straight phase modulator of the same length (blue line). The orange dashed line shows the simulated transmission for the measured directional coupler power splitting ratio of 0.12. The green dotted line is the simulated transmission for $\kappa = 0.09$, which is the value that gives the best fit to the data.

## 6.3   Chapter Summary

The device presented in Chapter 6 successfully reduced the RAM in an InP phase modulator by compensating for loss due to electro-absorption using a Mach-Zehnder interferometer architecture. The change in transmission over a $\pi$ phase shift was flattened from 3.85 dB to 1.98 dB for an 816 $\mu$m long phase modulator. This initial implementation of the low-RAM phase modulator design illustrates the utility of the concept for InP-based devices. Many more designs have been fabricated and need characterization. Future work should include a study of the effects on laser frequency modulation locking for straight versus low-RAM phase modulators.

## References

[1]   K. Numata, J. R. Chen, S. T. Wu, J. B. Abshire, and M. A. Krainak, "Frequency stabilization of distributed-feedback laser diodes at 1572 nm for lidar measurements of atmospheric carbon dioxide," *Applied Optics*, vol. 50, no. 7, pp. 1047–1056, 2011.

[2]   G. C. Bjorklund, "Frequency-modulation spectroscopy: A new method for measuring weak absorptions and dispersions," *Optics Letters*, vol. 5, no. 1, 1980.

[3]   S. Andreou, K. A. Williams, and E. A. J. M. Bente, "Steady-state analysis of the effects of residual amplitude modulation of inp-based integrated phased modulators in pound-drever-hall frequency stabilization," *IEEE Photonics Journal*, vol. 11, no. 3, 2019.

[4]   E. A. Whittaker, M. Gehrtz, and G. C. Bjorklund, "Residual amplitude modulation in laser electro-optic phase modulation," *Journal of the Optical Society of America B*, vol. 2, no. 8, 1985.

[5]   J. F. Diehl, C. E. Sunderman, J. M. Singley, V. J. Urick, and K. J. Williams, "Control of residual amplitude modulation in lithium niobate phase modulators," *Optics Express*, vol. 25, no. 26, 2017.

[6]   S. Andreou, K. A. Williams, and E. A. J. M. Bente, "Residual amplitude modulation in inp-based integrated phase modulators and its effect in pound-drever-hall frequency stabilization," *OSA Advanced Photonics Congress IPR*, 2017.

[7]   N. Dupuis, J. E. Proesel, H. Ainspan, C. W. Baks, M. Meghelli, and L. B. G., "Nanosecond-scale shift-and-dump mach-zehnder switch," *Optics Letters*, vol. 44, no. 18, pp. 4614–4616, 2019.

[8]   N. Dupuis, B. G. Lee, and M. A. Taubenblatt, "Electro-optic phase modulator with no residual amplitude modulation," *U.S. Patent 9,912,413 B1*, 2018.

[10]   B. Arar, M. Schiemangk, H. Wenzel, O. Brox, A. Wicht, A. Peters, and G. Trankle, "Method for in-depth characterization of electro-optic phase modulators," *Applied Optics*, vol. 56, no. 4, pp. 1246–1252, 2017.

# Chapter 7

# PIC System Characterization

After fabrication, thinning, cleaving, and anti-reflective (AR) coating, the photonic integrated circuit (PIC) bars underwent preliminary screening to check the optical power levels at various locations in the PIC and the power output from the PIC. Due to fabrication defects, especially in the directional couplers, which are difficult to fabricate accurately, not all of the PICs had enough power at the outputs and on-chip photodiode. The first PIC found to have adequate power levels was one with the design shown in Figure 7.1. The leader and follower lasers were sampled-grating distributed Bragg reflector (SGDBR) lasers with the same design as SGDBR laser design A in Section 5.1.2. The PIC uses 2x2 multimode interference (MMI) couplers for all light splitting and combining. The leader laser output path has a 1 mm long semiconductor optical amplifier (SOA) followed by a 900 $\mu$m long straight phase modulator. The follower laser output path has a 500 $\mu$m long SOA followed by a Mach-Zehnder modulator (MZM) and another 500 $\mu$m long SOA. The unlabelled devices seen in

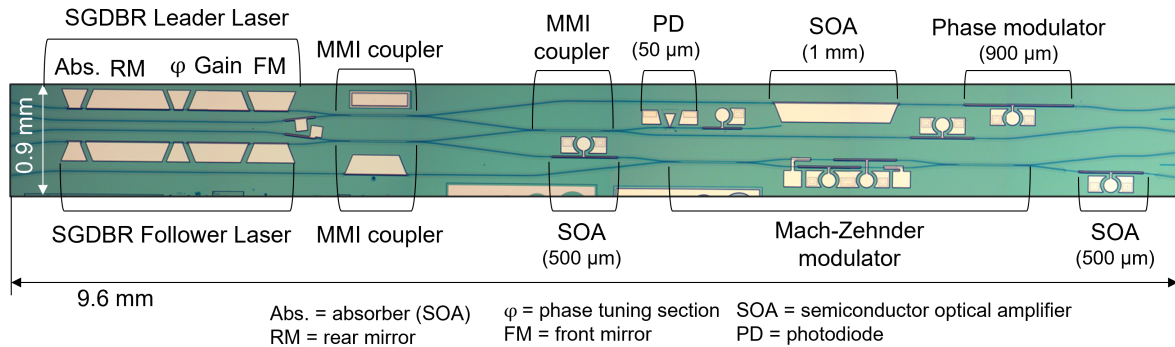Figure 7.1 are SOAs included for diagnostic and testing purposes.



Figure 7.1: Optical microscope image of the fabricated PIC that was characterized.
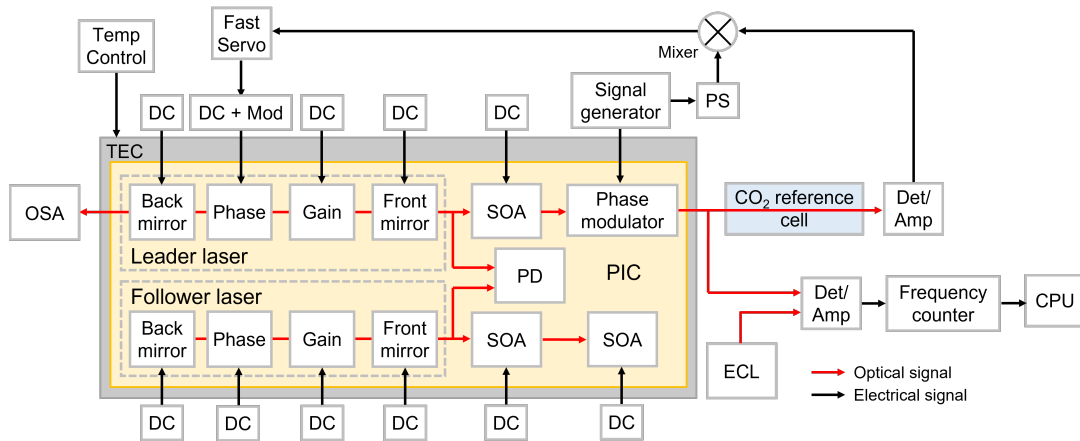
## 7.1   Leader Laser Stabilization



Figure 7.2: Test setup used for characterization of the leader laser frequency stabilization. OSA = optical spectrum analyzer; PS = phase shifter; ECL = external cavity laser; TEC = thermoelectric cooler.

The test setup used to characterize the leader laser frequency stabilization via frequency modulation locking is shown in Figure 7.2. Even though the devices used for the follower laser offset locking and pulsing were not needed, they were biased during the leader laser

107

stabilization measurement because thermal and electrical cross-talk between components affected the wavelength of the leader laser. A combination of Vescent Photonics SLICE-DCC-200 low-noise current sources and Kiethley SourceMeter units were used to bias on-chip components. The PIC was mounted on a thermally controlled stage. Tight thermal control is important for maintaining accurate laser frequency and the stage temperature was used for manual coarse wavelength targeting. A stage temperature must be found that allows both lasers in the PIC to achieve the desired wavelength tuning with reasonable SMSR. On-chip, the light from the leader laser goes to an SOA and phase modulator before being coupled off-chip. The phase modulator was forward biased at 23 mA and modulated by a signal generator (Anritsu MG3691B) with -7 dBm output power at 125 MHz. A lensed fiber was used to collect the output power. The lensed fiber output was split in two directions: one connected to a bench top $CO_2$ Herriott cell with a built-in photodiode and trans-impedance amplifier (TIA) and the other was combined with the output of an external cavity laser (ECL) (Agilent 8164B) and sent to a photodetector (New Focus model 1014).

The error signal detected at the reference cell output goes to the input of a Liquid Instruments Moku:Lab, an FPGA-enabled versatile testing module. The Laser Lock Box function of the Moku:Lab module was used to detect the error signal from the $CO_2$ gas reference cell and feedback an error signal to the phase section of the leader laser. The Moku:Lab contains the phase shifter, mixer, fast servo, and signal generator for feedback to the phase section of the leader laser.

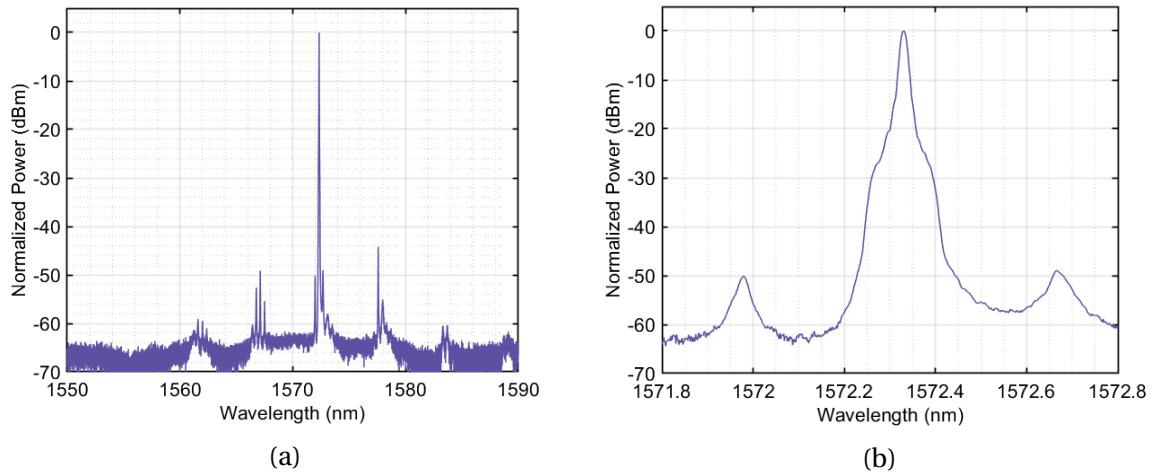The stabilization of the leader laser was characterized by measuring the beat note be-

Figure 7.3: Optical spectrum of the unlocked leader laser plotted over a (a) wide wavelength range to show an SMSR of 44 dB and (b) a narrow wavelength range to show the lasing wavelength at exactly 1572.335 nm.

tween the leader laser and a reference external cavity laser set to a frequency 1 GHz offset from the leader laser. Although the phase modulator introduced some chirp, the power output from the rear mirror of the laser was not high enough to use for characterization. After the photodetector sensing the combined leader laser and external cavity laser output, a frequency counter (BK Precision 1856D) measured the beat note frequency and the values were recorded over time with a computer. The leader laser spectrum was monitored out the back of the laser using a Yokogawa AQ6370D optical spectrum analyzer.

The spectrum of the unlocked leader laser is shown in Figure 7.3(a) and (b). Figure 7.3(a) plots the spectrum over the wavelength range from 1550 to 1590 nm, showing a 44 dB SMSR between the mode at 1572 nm and the other competing supermodes. Figure 7.3(b) plots the spectrum in a narrow range to show that the laser output is indeed centered at 1572.335 nm.

The frequency of the beat note between the leader laser and external cavity laser over

one hour is plotted in Figure 7.4. Unlocked, the peak-to-peak frequency variation was 2664 MHz and the frequency standard deviation was 251.5 MHz. Locked, the peak-to-peak frequency was 54 MHz and the frequency standard deviation was 7.2 MHz, a 49- and 35-fold improvement, respectively, demonstrating that the leader laser was successfully frequency locked.
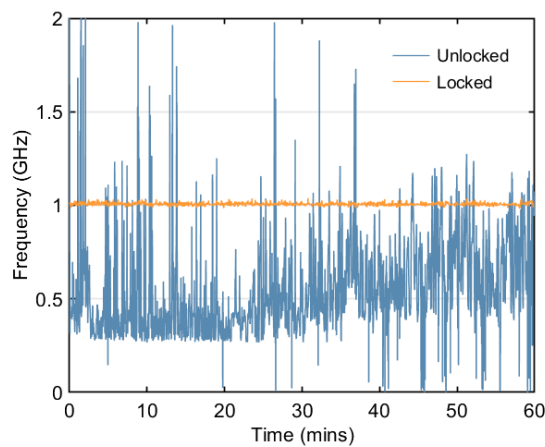


Figure 7.4: Beat note between the leader laser and an external cavity laser for the leader laser locked and unlocked over one hour.

## 7.2 Follower Laser Offset Locking and Pulsing

The setup used for testing the offset-locking of the follower laser is illustrated in Figure 7.5. The integrated photodiode was used to detect the beat note between the leader and follower lasers. The electrical output from the on-chip photodiode was split, with part of the signal going to the PLL board (Analog Devices SDP-S evaluation board) and the other part going to an electrical spectrum analyzer (ESA) (Rhode and Schwartz FSU). The feedback signal from the PLL board goes to the phase section of the follower laser. The interface for controlling

the PLL board with the settings used is shown in Figure 7.6. The follower laser frequency

offset was manually updated for each frequency step. The optical spectrum of the leader

and followers lasers were simultaneously viewed on the OSA. The optical spectra of both

lasers as the follower laser was frequency stepped from +2 to +15 GHz offset from the leader

laser is shown in Figure 7.7(a) and the corresponding signal from the on-chip photodiode

at each step is shown in Figure 7.7(b). The follower laser was successfully frequency offset

locked up to +15 GHz offset from the locked leader laser using the on-chip photodiode for
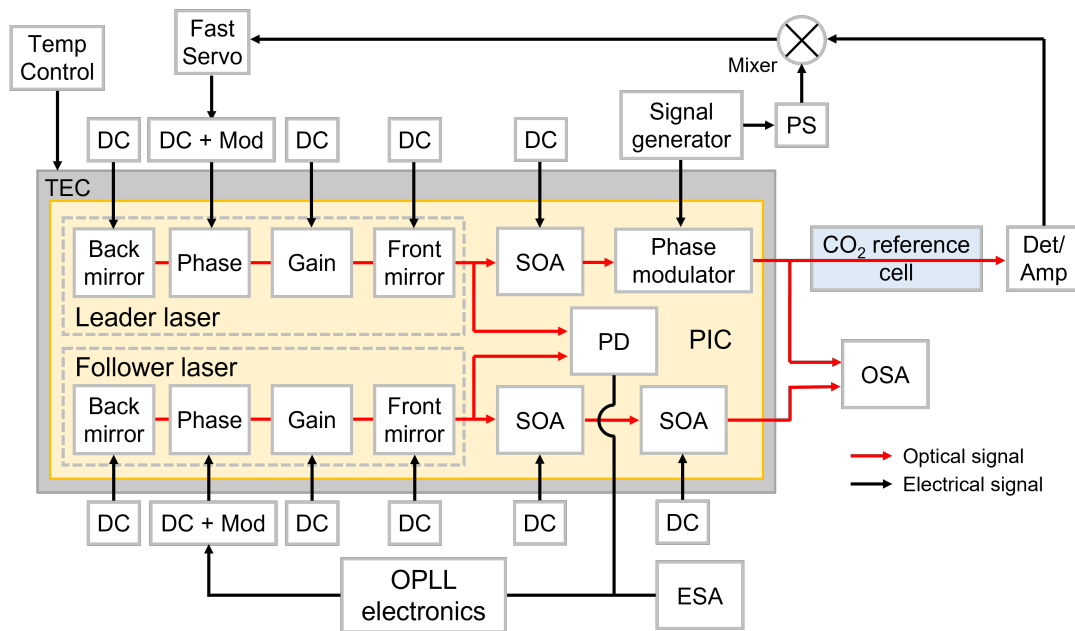
beat note detection.



Figure 7.5: Test setup used for characterization of the follower laser offset frequency stepping. OSA = optical spectrum analyzer; PS = phase shifter; OPLL = optical phase lock loop; TEC = thermoelectric cooler.

To characterize the follower laser stabilization at a given offset frequency, the test setup

was arranged as shown in Figure 7.8. The frequency of the beat note between the leader and

follower lasers for a +2 GHz offset over one hour is shown in Figure 7.9(a). With the follower
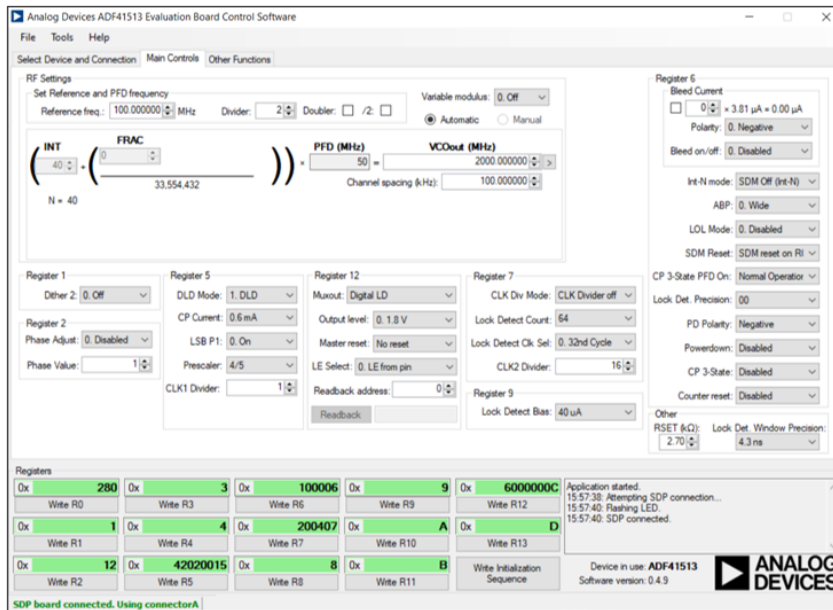
Figure 7.6: GUI with settings used for control of the Analog Devices evaluation board used for generating the PLL feed forward signal. The offset frequency of the follower laser was set manually using the VCOut and PD Polarity settings.

laser unlocked, the peak-to-peak frequency was 499 MHz and the frequency standard deviation was 86.9 MHz. With the follower laser locked, the peak-to-peak frequency was 47 MHz and the frequency standard deviation was 4.6 MHz, an 11- and 19-fold improvement, respectively, demonstrating that the follower laser was frequency locked.

The follower laser stabilization was able to be maintained over at least 15 hours as shown in Figure 7.9(b). Over 15 hours, the peak-to-peak frequency was 56 MHz and the frequency standard deviation was 6.1 MHz.

To produce high extinction ratio (ER) pulses after the follower laser, the bias applied to the SOA closest to the follower laser side output was pulsed using a laser diode driver (ILX Lightwave LDP-3840). The driver was set to output 1 $\mu$s pulses with a period of 133 $\mu$s with a bias sweep of 0 to 150 mA. The resulting output optical pulse is shown in Figure
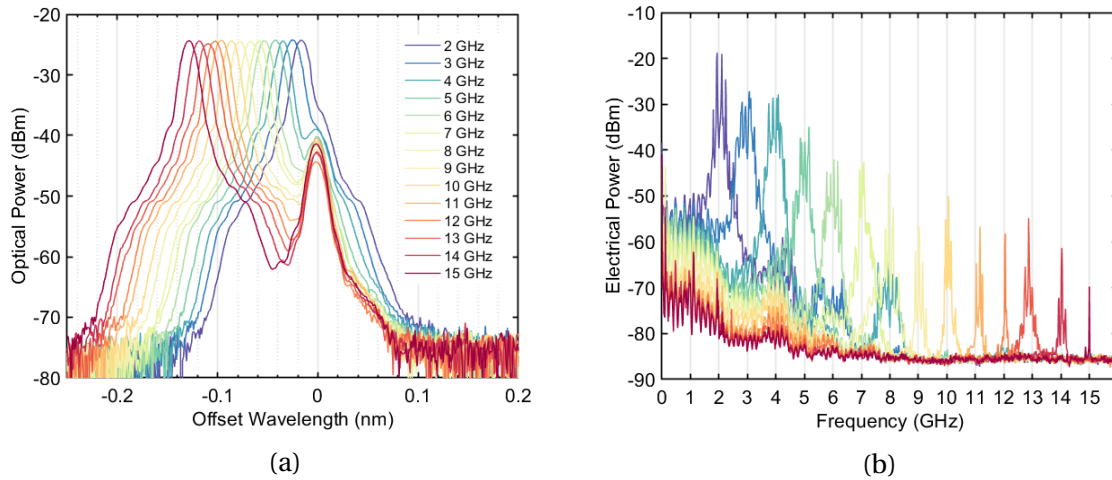
Figure 7.7: (a) Combined optical spectra of the leader and follower laser for the follower laser tuned from 2 to 15 GHz offset from the leader laser. (b) Electrical spectrum detected by the on-chip photodiode as the follower laser offset locking is stepped.

7.10. The pulse ER is at least 18 dB. This is about half of the required ER of 35 dB. The true ER may be higher because the zero of the pulse was at the noise floor of the photodiode and oscilloscope used to record it. In addition, the ER could be improved by sending the SOA into reverse bias in the off-state in order to further decrease the zero level. In PICs fabricated for this project using an offset quantum well (OQW) platform, ERs of at least 35 dB were observed [1].
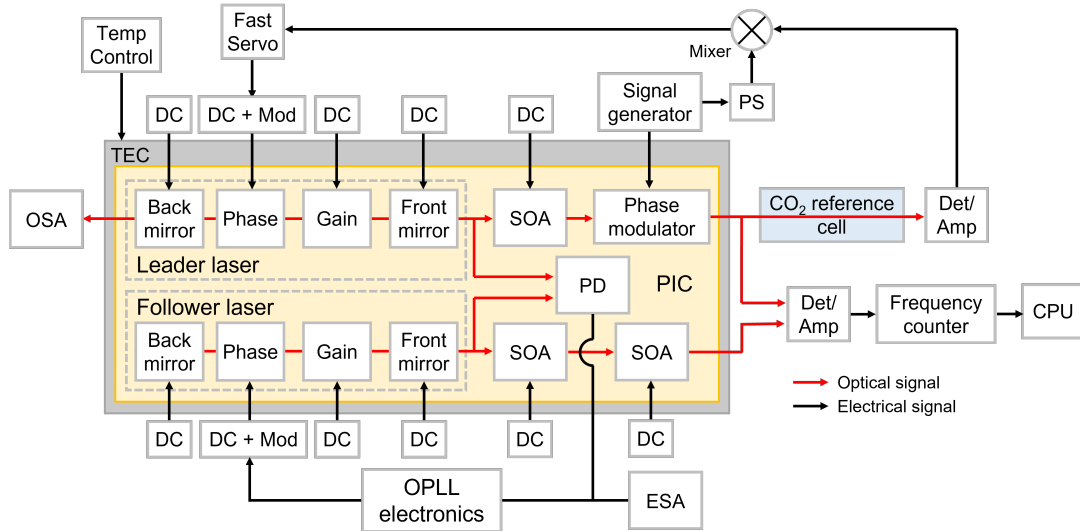
Figure 7.8: Test setup used for characterization of the follower laser frequency stabilization. OSA = optical spectrum analyzer; PS = phase shifter; OPLL = optical phase lock loop; TEC = thermoelectric cooler.
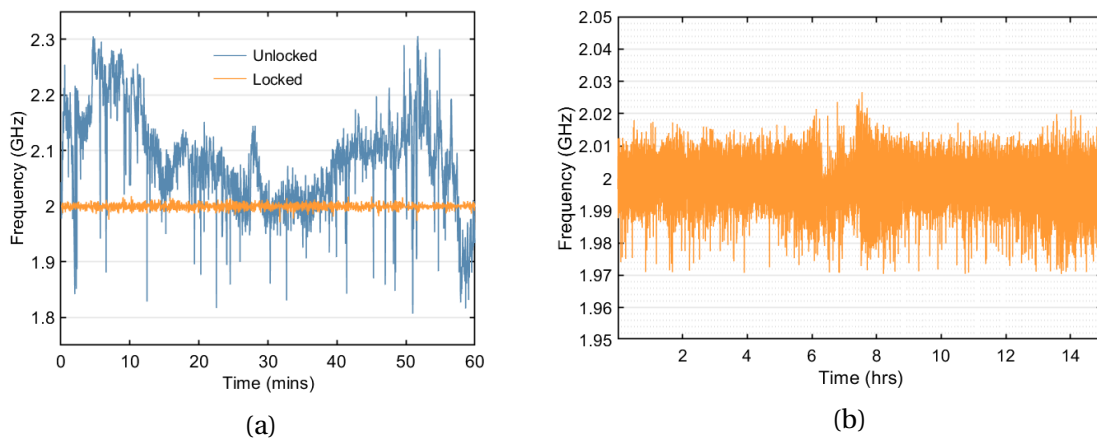


Figure 7.9: Beat note between the leader and follower laser for the follower laser (a) locked and unlocked for one hour and (b) locked for 15 hours.
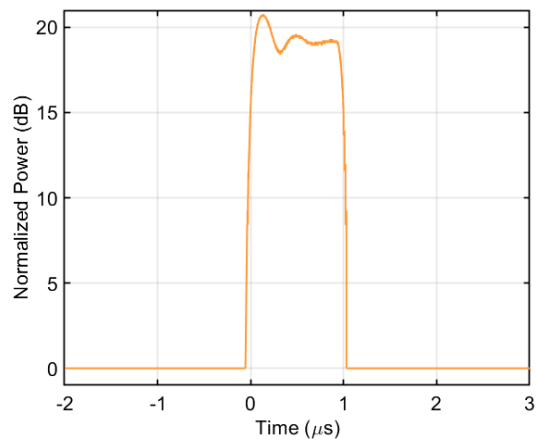
Figure 7.10: Optical pulse generated by sweeping the bias to the output SOA from 0 to 150 mA showing an 18 dB extinction ratio.

## 7.3 Gas Sampling

The test setup for demonstrating $CO_2$ gas sampling with the system is shown in Figure 7.11. The output from the follower laser was sent to a second $CO_2$ Herriott cell which was filled to a different pressure than the reference cell used for the leader laser. The DC and AC components of the signal detected at the cell output were measured using an oscilloscope (Tektronix MDO3024).
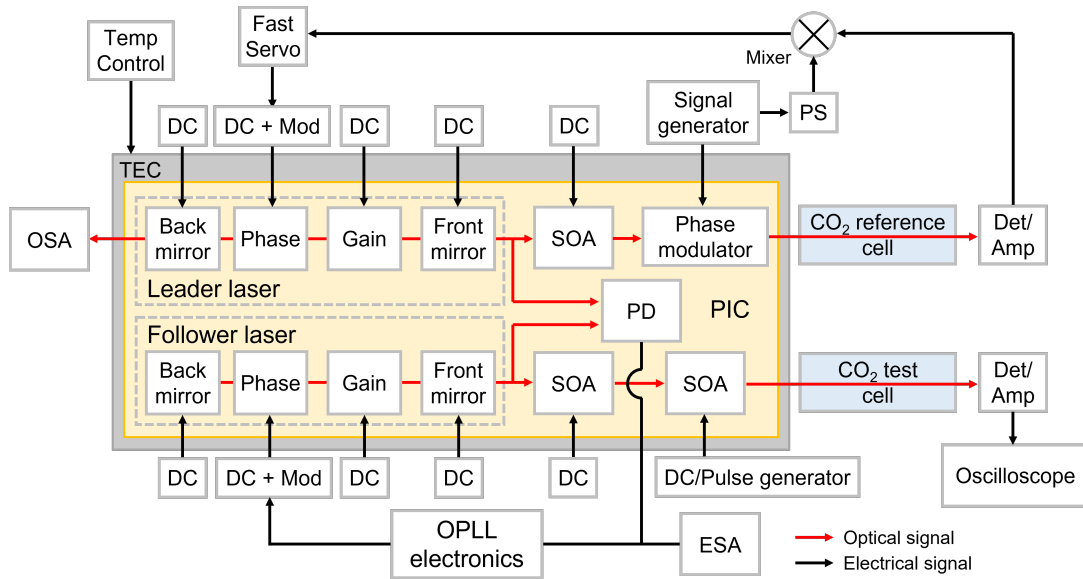


Figure 7.11: Test setup used for demonstrating $CO_2$ absorption line sampling. A second gas cell pressurized to a different value than the reference cell was added at the follower side output.

Frequency sampling of the $CO_2$ test cell absorption was performed by manually stepping the follower laser frequency and recording the oscilloscope output at each step. The data points measured for continuous wave sampling are plotted in Figure 7.12(a) along with a Lorentzian fitted curve. Each data point is an average of one million points taken over 400 $\mu$s. It is evident from Figure 7.12(a) that the $CO_2$ absorption line is able to be clearly mapped

using the lidar PIC under bench top testing. Figure 7.12(b) plots the data measured via pulsed sampling. Each data point is the average of three pulses over 400 $\mu$s. While there is clearly a dip in the transmission at the center wavelength, the absorption line shape is not nearly as clear as it is for the CW sampling curve. Part of the reason for this is that the pulsed data was only averaged over three pulses while the CW data was averaged over many points for the same period of time. The accuracy of the pulsed measurement could be improved by taking more data points per frequency step. This was not done because of the difficulty in manually managing that much data for a first demonstration. Secondly, there was a variation in power due to variation in the fiber alignment over time. All of these things could be improved by optical packaging and closely packaged electronics with automated data collection and analysis and are not limitations of the PIC performance.
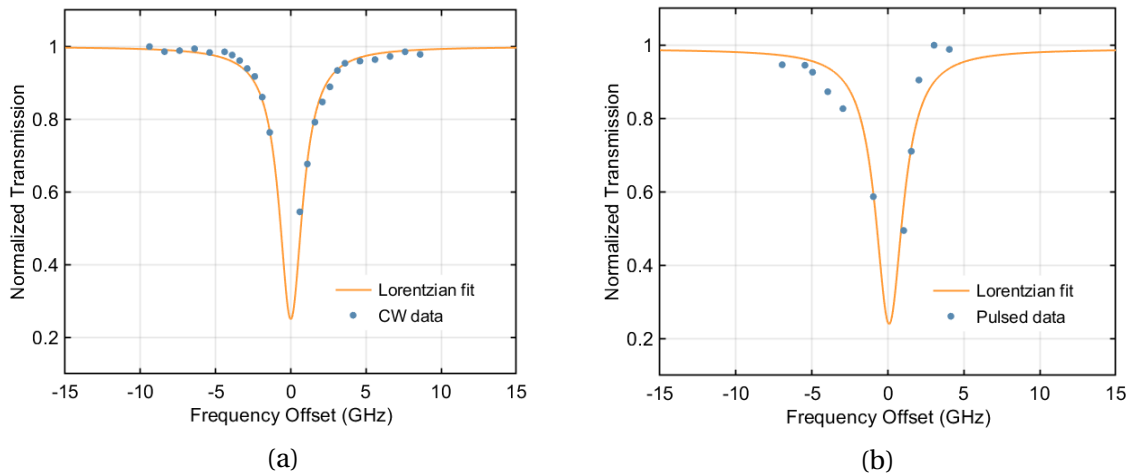


Figure 7.12: Optical transmission through the $CO_2$ test cell versus follower laser frequency offset plotted with a Lorentzian fit for (a) continuous wave and (b) pulsed operation.

## 7.4 Chapter Summary

Chapter 7 covered the subsystem characterization of the lidar PIC showing successful frequency stabilization of the leader and follower lasers and offset frequency locking and pulsing of the follower laser. Continuous wave $CO_2$ sampling was demonstrated as well, showing the viability of PIC technology for differential absorption lidar (DIAL) gas spectroscopy. This is the first QWI PIC ever demonstrated that integrates most of the optical functionality for a DIAL system. The only optical functions that currently need to be performed off-chip are the optical path through the gas reference cell and amplification of the final output using an erbium-doped fiber amplifier. The first PIC demonstrated for this application was the offset quantum well (OQW) based PIC that was developed in our research group under the same program. To further mature the platform, future work should include screening of all the PIC designs to determine the best performing variations. A study of the on-chip reflections and their effect on the laser frequency stabilization, SMSR, linewidth, and noise would also provide insight for downselecting and improving the PIC layout.

## References

[1]  J. Fridlander, F. Sang, V. Rosborough, F. Gambini, S. T. S. Brunelli, J. R. Chen, K. Numata, M. Stephen, L. A. Coldren, and J. Klamkin, "Dual laser indium phosphide photonic integrated circuit for integrated path differential absorption lidar," *IEEE Journal*

*of Selected Topics in Quantum Electronics,* vol. 28, no. 1, 2022. DOI: 10.1109/JSTQE.2021.3091662.

# Chapter 8

# Summary and Future Work

## 8.1  Summary of Accomplishments

This work demonstrated (1) a novel method for simultaneous definition of variable $\kappa$ laser mirror gratings, (2) design, fabrication, and characterization of extremely high side mode suppression ratio (SMSR) distributed feedback (DFB) lasers, (3) a novel implementation of a low residual amplitude modulation (RAM) phase modulator design, and (4) integration of most of the optical functions for a differential absorption lidar system using a quantum well intermixing (QWI) platform photonic integrated circuit (PIC) in indium phosphide (InP).

## 8.2  Future Work

The next steps to actualizing a PIC-enabled remote sensor revolve around co-packaging with control electronics, miniaturization of the wavelength reference for the leader laser,

and space qualification and reliability testing. This section reviews options that were explored for a compact wavelength reference.

### 8.2.1 Compact Wavelength References

One of the remaining obstacles to miniaturizing the entire $CO_2$ lidar system is the creation of a compact reference for stabilizing the leader laser at a precise wavelength of 1572.335 nm. Figure 8.1 shows a photo of the bench top $CO_2$ Herriott cell currently used to lock the leader laser. The cell is 13 inches long with 2.5 inch diameter flanges at either end and has a 10 meter optical path length. Potential wavelength references can be sorted into two categories: absolute and calibrated. Absolute references use the $CO_2$ absorption line itself as a reference, as was done in this work. A calibrated wavelength reference would use a filter with a notch in its spectral response at 1572.335 nm.
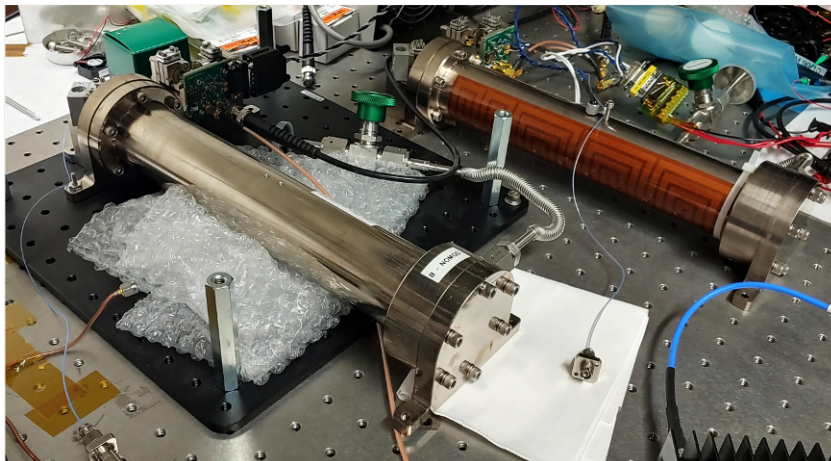


Figure 8.1: Benchtop Herriott gas cells used for leader laser stabilization and $CO_2$ sampling demonstration.

**Absolute References**

An absolute wavelength reference is the ideal option because it is not highly dependent on environmental conditions. However, an integrated or compact gas reference is difficult to realize due to there being a minimum required optical path length. The $CO_2$ absorption line at 1572.335 nm was chosen partly because it is not strongly absorbing. To discern differences in gas concentration, the probing signal must not be completely absorbed by the atmospheric $CO_2$ in its path to the ground and back to the on-board receiver. An integrated waveguide solution would be preferable for its small size, but the waveguide must also be very low loss to comprise meters of optical path length. One option considered was a hollow-core antiresonant reflecting optical waveguide (ARROW) [1]–[3] design, where the optical mode is confined to the gas-filled core. However, these waveguides are difficult to fabricate and do not have low enough propagation loss to support path lengths on the order of meters. Ultra low loss silicon nitride waveguides can support meter-class waveguide lengths. It could be possible to use a low-loss silicon nitride waveguide evanescently coupled to $CO_2$, similar to the Si on-chip sensor in [4] (see Section 2.3.1), but because of the small interaction area, the waveguide length would need to be further increased, diminishing the size advantage of an integrated approach [5], [6].

Another compact option is a gas-filled hollow-core fiber, which has been successfully demonstrated for laser frequency modulation locking using a $CO_2$ absorption line at 2 $\mu$m [7] and for $CH_4$ and $CO_2$ detection at 3.3 and 1.57 $\mu$m, respectively, using wavelength modulation spectroscopy [8]. The main drawbacks of hollow-core fibers are the difficulty in

handling them for connectorization and the presence of higher order and cladding modes, which can be addressed through careful design of the antiresonant structure [9]. Finally, extremely compact multi-pass gas cells have been developed [10]–[12]. Designed for absorption spectroscopy, a single reflective toroidal surface has been used to demonstrate a 10 meter-long path length in a cell with a mass of only 200 g [11]. However, this type of cell requires very precise machining and can suffer from fringe effects caused by the divergence of the beam after multiple reflections.

**Calibrated References**

An optical wavelength filter such as a Bragg grating filter, ring resonator, or asymmetric interferometer could be used as a reference. These approaches would be better suited to integration since they do not require the long optical path length of an absolute wavelength reference. The main drawback is that the filter environment, especially the temperature, must be carefully controlled to maintain the correct filter response. Some work has been done on fabricating athermal devices through the use of materials with thermo-optic coefficients of opposite signs. For example, $TiO_2$ clad Si ring resonators have been demonstrated with resonances that vary by less than 6 pm/°C at 1.3 $\mu$m over a temperature range of 20-50 °C [13]. Wavelength variation of less than 0.5 pm/°C has been achieved for an integrated Mach-Zehnder interferometer using doped silica waveguide cores [14]. Further work is required to identify and qualify the best compact wavelength reference approach.

# References

[1] G. Testa, G. Persichetti, and R. Bernini, "Hollow-core-integrated optical waveguides for mid-ir sensors," *IEEE Journal of Selected Topics in Quantum Electronics*, vol. 24, no. 6, 2018.

[2] D. Yin, H. Schmidt, J. P. Barber, and A. R. Hawkins, "Integrated arrow waveguides with hollow cores," *Optics Express*, vol. 12, no. 12, 2004.

[3] H. P. Uranus, H. J. W. M. Hoekstra, and E. van Groesen, "Considerations on material composition for low-loss hollow-core integrated optical waveguides," *Optics Communications*, 2005.

[4] C. Xiong, Y. Martin, E. J. Zhang, J. S. Orcutt, M. Glodde, L. Schares, T. Barwicz, C. C. Teng, G. Wysocki, and W. M. J. Green, "Silicon photonic integrated circuit for on-chip spectroscopic gas sensing," in *Proc. of SPIE*, ser. Silicon Photonics XIV, 2019. DOI: 10. 1117/12.2511793.

[5] R. Siebert and J. Muller, "Infrared integrated optical evanescent field sensor for gas analysis," *Sensors and Actuators A*, vol. 119, 2005.

[6] Y. Huang, S. K. Kalyoncu, Q. Zhao, R. Torun, and O. Boyraz, "Silicon-on-sapphire waveguides design for mid-ir evanescent field absorption sensors," *Optics Communications*, vol. 313, pp. 186–194, 2014.

[7] P. G. Westergaard, J. W. Thomsen, M. R. Henriksen, M. Michieletto, M. Triches, J. K. Lyngso, and J. Hald, "Compact, co2-stabilized tuneable laser at 2.05 microns," *Optics Express*, vol. 24, no. 5, 2016.

[8] P. Jaworski, P. Koziol, K. Krzempek, D. Wu, F. Yu, P. Bojes, G. Dudzik, M. Liao, K. Abramski, and J. Knight, "Antiresonant hollow-core fiber-based dual gas sensor for detection of methane and carbon dioxide in the near- and mid-infrared regions," *Sensors*, vol. 20, 2020. DOI: 10.3390/s20143813.

[9] A. Hartung, J. Kobelke, A. Schwuchow, J. Bierlich, J. Popp, M. A. Schmidt, and T. Frosch, "Low-loss single-mode guidance in large-core antiresonant hollow-core fibers," *Optics Letters*, vol. 40, no. 14, pp. 3432–3435, 2015.

[10] A. Manninen, B. Tuzson, H. Looser, Y. Bonetti, and L. Emmenegger, "Versatile multipass cell for laser spectroscopic trace gas analysis," *Lasers and Optics Applied Physics B*, vol. 109, pp. 461–466, 2012.

[11] M. Graf, L. Emmenegger, and B. Tuzson, "Compact, circular, and optically stable multipass cell for mobile laser absorption spectroscopy," *Optics Letters*, vol. 43, no. 11, pp. 2434–2437, 2018.

[12] H. Chang, S. Feng, X. Qiu, H. Meng, G. Guo, X. He, Q. He, X. Yang, W. Ma, R. Kan, C. Fittschen, and C. Li, "Implementation of the toroidal absorption cell with multi-layer patterns by a single ring surface," *Optics Letters*, vol. 45, no. 21, pp. 5897–5900, 2020.

[13]  S. Feng, K. Shang, J. T. Bovington, R. Wu, B. Guan, K.-T. Cheng, J. E. Bowers, and S. J. B. Yoo, "Athermal silicon ring resonators clad with titanium dioxide for 1.3 micron wavelength operation," *Optics Express*, vol. 23, no. 20, 2015.

[14]  L. Zuo, H. Suzuki, K. Kong, J. Si, M. M. Aye, A. Watabe, and S. Takahashi, "Athermal silica-based interferometer-type planar lightwave circuits realized by a multicore fabrication method," *Optics Letters*, vol. 28, no. 12, pp. 1046–1048, 2003.